

## Turbomachinery Developments and Cavitation

**Luca d'Agostino**

Alta S.p.A., 5 Via A. Gherardesca, 56121 Ospedaletto (Pisa)  
Università di Pisa, Pisa  
ITALY

[l.dagostino@alta-space.com](mailto:l.dagostino@alta-space.com)

### **ABSTRACT**

*After a brief review of flow-induced instabilities in turbopumps for liquid propellant feed systems of modern rocket engines, the lecture illustrates some recent results of the work carried out at Alta on the hydrodynamics and unsteady cavitation phenomena of these machines.*

*A reduced order model for preliminary design and noncavitating performance prediction of tapered axial inducers is illustrated. In the incompressible, inviscid, irrotational flow approximation the model expresses the 3D flow field in the blade channels by superposing a 2D cross-sectional vorticity correction to a fully-guided axisymmetric flow with radially uniform axial velocity. Suitable redefinition of the diffusion factor for bladings with non-negligible radial flow allows for the control of the blade loading and the estimate of the boundary layer blockage at the specified design flow coefficient, providing a simple criterion for matching the hub profile to the axial variation of the blade pitch angle. Carter's rule is employed to account for flow deviation at the inducer trailing edge. Mass continuity, angular momentum conservation and Euler's equation are used to derive a simple 2nd order boundary value problem, whose numerical solution describes the far field axisymmetric flow at the inducer discharge. A closed form approximate solution is also provided, which proved to yield equivalently accurate results in the prediction of the inducer performance. Finally, the noncavitating pumping characteristic is obtained by introducing suitably adapted correlations of pressure losses and flow deviation effects. The model has been verified to closely approximate the geometry and noncavitating performance of a number of tapered-hub high-head inducers for space application.*

*The results of a series of tests conducted in water under similarity conditions on the four-bladed DAPAMITO4 inducer, designed and manufactured by means of the above reduced-order model, are illustrated. Several non-synchronous instabilities have been observed on the inducer, including an axial surge, a backflow oscillation and, at higher temperatures, incipient rotating cavitation and backflow vortex instability. In addition, synchronous rotating cavitation (leading to the characteristic "one step" shape of the cavitating performance curve near head breakdown conditions) has been detected at all the flow conditions investigated. It has been found that the amplitude of the flow oscillations associated to this instability generally tends to decrease at higher water temperatures.*

*The characterization of the rotordynamic forces acting on a whirling four-bladed, tapered-hub, variable-pitch high-head inducer, under different load and cavitation conditions is presented. The results have obtained in the Cavitating Pump Rotordynamic Test Facility at Alta by means of a novel experimental technique, allowing for the continuous measurement of the rotordynamic force spectra as functions of the whirl ratio. Comparison with simultaneous high-speed movies of the inducer inlet flow highlighted the relationship between the cavitation dynamics in the inducer backflow and the spectral behavior of the*

## Fluid Dynamics Associated to Launcher Developers

rotordynamic force as functions of the whirl ratio.

Finally, the future perspectives of the work carried out at Alta on the hydrodynamics and unsteady cavitation phenomena of high performance turbopumps for liquid propellant feed systems of modern rocket engines are briefly illustrated.

## 1.0 HYDRODYNAMIC INSTABILITIES OF TURBOPUMPS

### 1.1 Introduction

Propellant feed turbopumps are a crucial component of all liquid propellant rocket engines because of the severe limitations associated with the design of high power density, dynamically stable machines capable of meeting the extremely demanding suction, pumping and reliability requirements of modern space transportation systems. Figure 1 shows the evolution of the power/weight ratio of the main propellant feed turbopumps used by US space rocket engines powering the Mercury, Gemini, Apollo and Space Shuttle programs in the two decades from the early '60s to the '80s. The ten-fold increase of the power density clearly indicates that today's rocket propellant feed turbopumps belong to a special family of machines with respect to earlier more conventional land or sea-based applications.

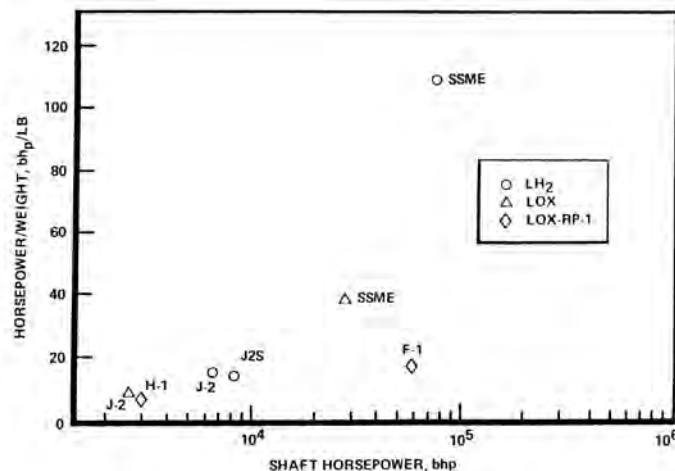


Figure 1. Power/weight evolution of propellant feed turbopumps for US space rocket engines (Rockwell International, personal communication).

The attainment of such high power/weight ratios is invariably obtained by running the impeller at the maximum allowable speed and lower shaft torque. Operation under cavitating conditions with lighter – but also more flexible – shafts is therefore tolerated, exposing rocket propellant feed turbopumps to the onset of dangerous cavitation-induced fluid dynamic and rotordynamic instabilities.

Cavitation represents the major source of degradation of their suction performance, efficiency, reliability, power density and useful life ([77] Stripling and Acosta 1962). More importantly for space applications, cavitation can provide the necessary flow excitation and compliance for triggering dangerous fluid mechanic and/or rotordynamic instabilities of the turbopump ([69] Sack and Nottage 1965, [60] Natanzon et al. 1974, [10] Brennen and Acosta 1973, [11] Brennen and Acosta 1976, [61] Ng and Brennen 1978, [5] Braisted 1979, [24] d'Auria, d'Agostino and Brennen 1995, [17] d'Agostino, d'Auria and Brennen 1998, [18] d'Agostino and Venturini-Autieri 2002, [19] d'Agostino and Venturini-Autieri 2003), or even, through the coupling with thrust generation and the structural response, of the entire space vehicle (POGO auto-

oscillations, [67] Rubin 1966).

The most critical rotordynamic instability in turbopumps is the development of self-sustained lateral motions (whirl) of the impeller under the action of destabilizing forces of mechanical or fluid dynamic origin. Because of their greater complexity, rotordynamic fluid forces have so far received relatively little attention in the open literature, despite of their well recognized potential for promoting rotordynamic instabilities of high performance turbopumps ([66] Rosenmann 1965) by significantly modifying, in conjunction with cavitation, the dynamic properties of the impeller, and therefore the critical speeds of the whole machine ([27] Franz 1989, [3] Bhattacharyya 1994, [3] Bhattacharyya et al. 1997, [24] d'Auria, d'Agostino and Brennen 1995, [17] d'Agostino, d'Auria and Brennen 1998, [18] d'Agostino and Venturini-Autieri 2002, [19] d'Agostino and Venturini-Autieri 2003).

Typically cavitation of the liquid propellant is confined to the turbopump inducer, an initial axial-flow or mixed-flow impeller routinely used to sufficiently raise the fluid pressure for suppressing cavitation in the main centrifugal impeller(s). The main forms of cavitation developing in turbopump inducers are schematically illustrated in Figure 2. Cavitation first appears in the core of the vortex generated by the blade tips when the Euler (or cavitation) number:

$$\sigma = \frac{P_{ref} - P_v}{\frac{1}{2} \rho \Omega^2 r_T^2}$$

drops below the inception value, which essentially depends on the geometry of the machine. Next, more extensive cavitation develops, starting in the leakage flow at the blade tips and progressively extending on the suction sides of the blades towards the hub. The bubbly, cloudy or attached nature of blade cavitation depends on the dominant location and susceptibility of the nuclei responsible for the inception of cavitation, as well as on the thermodynamic state of the liquid and the nature of the flow (laminar/turbulent, separated/unseparated, etc.). Finally, especially at high blade loads, cavitation can also appear in the separated, recirculating and slowly co-rotating backflow that develops at the inlet of the inducer near the side wall of the casing as a consequence of the combined effects of tip blade and leading edge flow leakage.

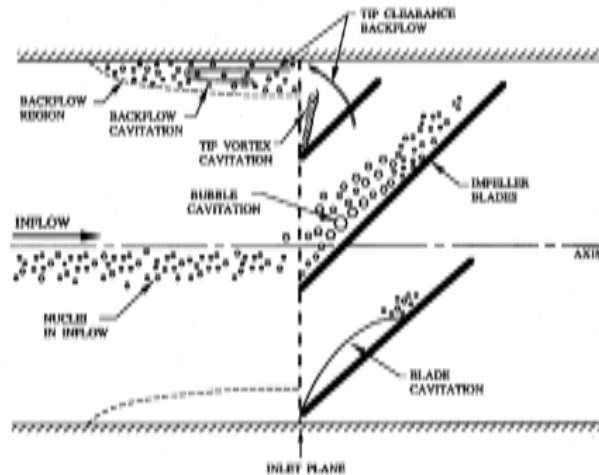


Figure 2. Types of cavitation in turbopumps.

With reference to Table 1 flow-induced instabilities of turbopumps can be conventionally classified as proposed in [1] by Brennen 1994 in: *global oscillations* (category A, including surge, cavitation auto-

## Fluid Dynamics Associated to Launcher Developers

oscillations, rotating stall, rotating cavitation, unsteady partial-blade and vortex cavitation, higher order cavitation surge), which affect the whole machine or even the entire pumping system on a large scale, *local oscillations* (category B, like blade flutter and rotor-stator interactions), of more limited impact, and *rotordynamic instabilities* (category C), caused by fluid forces on the impellers.

**Table 1. Original classification of flow instabilities by Brennen 1994, [8].**

VIBRATION CATEGORY	FREQUENCY RANGE
A2 Surge	System dependent, 3 – 10 Hz in compressors
A2 Auto-oscillation	System dependent, 0.1 – 0.4Ω
A1 Rotor rotating stall	0.5Ω – 0.7Ω
A1 Vaneless diffuser stall	0.05Ω – 0.25Ω
A1 Rotating cavitation	1.1Ω – 1.2Ω
A3 Partial cavitation oscillation	< Ω
C1 Excessive radial force	Some fraction of Ω
C2 Rotordynamic vibration	Fraction of Ω when critical speed is approached.
A4 Blade passing excitation (or B2)	$Z_R\Omega/Z_{CF}, Z_R\Omega, mZ_R\Omega$ (in stator frame) $Z_S\Omega/Z_{CF}, Z_S\Omega, mZ_S\Omega$ (in rotor frame)
B1 Blade flutter	Natural frequencies of blade in liquid
B3 Vortex shedding	Frequency of vortex shedding
A6 Cavitation noise	1 kHz – 20 kHz

Another useful classification of cavitation-induced turbopump instabilities has been proposed in [26] by Franc 2001, who distinguishes between *system* instabilities, also involving the other components of the pumping system (inlet and outlet lines, tanks, valves), and *intrinsic* instabilities, whose features are dependent on the characteristics of the pump.

The cavitating behavior of a rotating machine can often be usefully interpreted with reference to the equivalent features of the flow through static cascades of hydrofoils. In this order of approximation, cavitation surge, sometimes observed in supercavitating hydrofoils ([92] Wade and Acosta 1966) as a result of the interactions of long cavities with the dynamics the other components of the circuit, is probably the most well-known system instability. On the other hand, unsteady cloud cavitation, characterized by the periodic break-up of the cavity developing on highly loaded lifting surfaces and by the subsequent shedding of a large-scale vortex containing a cluster of many small bubbles ([51] Kubota et al. 1989), is a typical example of intrinsic instability. Experiments carried in out facilities with different characteristics or adjustable configurations ([87] Tsujimoto, Watanabe and Horiguchi 1998) led to very similar Strouhal numbers for the cloud oscillations and proved the correlation between cloud cavitation and the re-entrant jet generated at the cavity closure for cavity lengths greater than about 50% of chord ([12] Callenaere, Franc and Michel 1998, [48] Kawanami et al. 1997, [70] Sakoda et al, 2001).

### 1.2 Rotating Stall

Rotating stall typically occur in compressors operating at high incidence, where it has been extensively investigated because of its critical impact on the performance and stability of the machine ([33] Greitzer 1981). However, it has also been observed in noncavitating turbopumps at low flow rates operating near the maximum of the pumping characteristic. As a consequence of the distortions generated in the flow field,

partial stall cells tend to rotate in the opposite direction of the impeller with an absolute speed equal to 50-70% of the rotor speed. Rotating stall is most frequently observed in compressors with a large number of blades, but it has also been detected in pumps with a just 3 or 4 blades. Actually, in [55] Murai 1968 was the first to detect and investigate rotating stall in an axial flow pump with 18 blades. He measured stall propagation velocities between 0.45 and 0.6 times the impeller rotational speed, and observed that it was somewhat affected by the occurrence of a limited amount of cavitation.

A useful approximate criterion in compressors predicts the onset of rotating stall when the maximum of the total head rise curve is approached as the flow coefficient decreases. As a consequence, a number of authors postulated that also rotating stall in inducers could be associated to areas of positive slope of the pumping performance curve (see for example [45] Kamijo et al. 1977). This is, however, no more than an approximation ([33] Greitzer 1981). More sophisticated stall criteria typically take into consideration the evolution of the displacement thickness on the blade suction side. In particular, following this approach, in [54] Leiblein 1965 has been able to demonstrate the correlation of stall with a simple integral parameter of the flow, the diffusion factor, predicting the occurrence of stall on typical blade profiles when its value exceeds about 0.6.

### 1.3 Rotating Cavitation

At low Euler numbers, cavitating inducers and pump impellers can exhibit a phenomenon similar to rotating stall, known as rotating cavitation. Even the two phenomena look similar, significant differences exist. Rotating stall occurs at locations of the head-flow characteristic where the slope of the curve is positive and therefore unstable. Rotating cavitation, on the other hand, is normally observed in the zone of negative slope at cavitation numbers between 2 and 3 times larger than the breakdown value. Even if subsynchronous (or “backward rotating”) rotating cavitation has sometimes been observed, usually it is supersynchronous (forward rotating with respect to the impeller blades) with frequencies between 1.1 and 1.2 times the pump’s rotational speed, as indicated in Figure 3 (from [8] Brennen 1994) with reference to the inducer tested by Kamijo et al. 1977, [45].

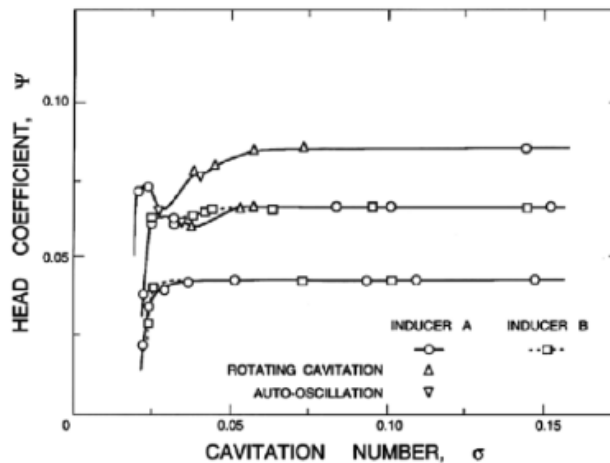


Figure 3. Occurrence of rotating cavitation and auto-oscillation in the performance of a cavitating inducer ([8] Brennen 1994).

The first observation of rotating cavitation was probably documented in [66] by Rosenmann 1965, who reported a vibration with similar characteristics in some of his experiments on inducers operating at cavitation numbers between 2 and 3 times the breakdown value. However, Rosenmann did not recognize

## Fluid Dynamics Associated to Launcher Developers

---

this phenomenon as rotating cavitation. It has first been identified explicitly in [45] by Kamijo et al. 1977, and associated to the portion of the inducer performance curve with negative slope, where the head is starting to be affected by cavitation.

A detailed theoretical analysis of rotating cavitation was proposed in [87] by Tsujimoto et al. 1993. They used a simplified analytical model based on the actuator disk equations, able of reproducing fairly well the experimental results available at that time (in particular, those obtained by Kamijo et al. 1977, [45]). The most interesting results of their model were:

- Rotating cavitation is a completely different phenomenon from rotating stall, which is not significantly affected by the existence of cavitation. In particular, rotating cavitation is caused by a positive mass flow gain factor, while rotating stall is caused by the positive slope of the performance curve.
- The two driving parameters for the onset of rotating cavitation are the mass flow gain factor  $M$  and the cavitation compliance  $K$ . Other parameters, like flow coefficient and cavitation number, do not affect rotating cavitation directly.
- Two modes of rotating cavitation are predicted by the model: not only a “forward” rotating mode (i.e. rotating faster than the impeller speed), but also a “backward” rotating mode (slower than the impeller speed).

Similar results were obtained with a more refined model based on annular cascade equations, and presented in [99] by Watanabe et al. 1999. Several instability modes were obtained by the model as solutions of the characteristic equation, including rotating stall, forward and backward rotating cavitation, and various secondary radial modes.

In [34] Hashimoto et al. 1997 first investigated the behavior of rotating cavitation on a 3-bladed inducer, observing that it was almost suppressed using a casing with a forward-facing step. In a second paper [35] (Hashimoto et al. 1997b) they analyzed the influence of the rotational speed of the inducer, showing that the operational conditions for the occurrence of rotating cavitation, asymmetric cavitation and low-cycle oscillations (or cavitation surge) can be different depending on the geometry of the inducer casing. Rotating cavitation can eventually disappear at higher rotating speeds. Backward rotating cavitation, predicted by in [87] by Tsujimoto et al. 1993, was first detected and recognized by analyzing the cross-correlation phase of pressure signals from transducers flush-mounted on the casing at different angular stations near the leading edges of the inducer. These results were also confirmed in [86] by Tsujimoto et al. 1997, who observed backward rotating cavitation with a propagation speed of about 0.9 times the inducer rotational speed.

Rotating cavitation has also been detected in both water and LOX tests of the Fastrac engine turbopump, [100] (Zoladz 2000), where a connection with cavitation surge has also been observed. The frequency of rotating cavitation decreased (tending to synchronous frequency) as the cavitation number approached breakdown conditions. This result is consistent with the predictions of the linear 2D cascade model with closed cavities proposed in [88] by Tsujimoto 2001, who also found that 4-bladed inducers are expected to show higher rotating cavitation frequencies than 3-bladed ones and, furthermore, that the onset point of cavitation corresponds to a cavity length equal to about 70% of the blade spacing.

Recent 3D simulations (see for example [49] Kimura et al. 2006, [47] Kang et al. 2007) indicate that the interaction between the tip leakage vortex and the next blade plays a central role in the onset of rotating cavitation. The design of inducer leading edge shape is therefore of great importance for the suppression of the rotating cavitation. Furthermore, it has been recognized that rotating instability modes can be controlled by changing the shape of the inducer casing. In particular, in [74] Shimiya et al. 2006, have shown that the use of J-Grooves on the inducer casing can effectively reduce or suppress rotating cavitation, but also promotes the occurrence of cavitation surge modes generated by the interference of the tip leakage vortex

cavitation and the leading edge of the next blade. At higher cavitation numbers, these modes can be reduced by extending the J-Groove further upstream of the inducer leading edges, but can not be suppressed in this way at lower cavitation numbers. Furthermore, the use of J-Groove seems not to be effective for the control of the rotating cavitation at higher flow coefficients near design conditions.

More recently, rotating cavitation has been observed at Pratt-Whitney Rocketdyne laboratories in a 3-bladed LH2 inducer ([71] Sargent et al. 2008). The 2D simulations reported in [63] by Ohta and Kajishima 2008 also predicted a forward-running rotating cavitation mode in a 3-bladed inducer and a backward- running mode with similar characteristics in a 4-bladed inducer.

#### 1.4 Other Rotating Instabilities

Attached uneven cavitation (also called “steady asymmetric cavitation” or “synchronous rotating cavitation”) and alternate blade cavitation are synchronous rotating instabilities frequently occurring in cavitating inducers (see Figure 4). Attached uneven cavitation is characterized by nonuniform length of the cavities developing on the inducer blades. It can be considered as a single-cell rotating cavitation moving with the same angular velocity of the inducer and generates a peak in the pressure spectra at the synchronous frequency. Alternate blade cavitation is frequently observed in inducers with an even number of blades when alternate blades experience different intensities of cavitation. It can be considered as a synchronous rotating cavitation mode with a number of cells equal to one half of the number of blades and generates a peak in the pressure spectra at a frequency equal to the synchronous frequency multiplied by the number of cells.

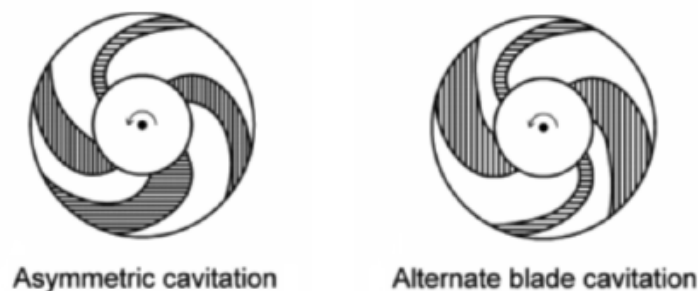


Figure 4. Schematic representation of the asymmetric cavitation (left) and the alternate blade cavitation (right). Experimental observations of synchronous rotating instabilities were presented in [34] by Hashimoto et al. 1997. Attached uneven cavitation was observed in both a 3-bladed and a 4-bladed inducer operating at lower cavitation numbers near breakdown conditions. Alternate blade cavitation was observed on the 4-bladed inducer at higher cavitation numbers, around 2-3 times the breakdown value. Both instabilities occurred at high flow coefficients close to the design point. Not surprisingly, alternate blade cavitation, unlike attached uneven cavitation, did not induce significant shaft vibrations because of the polar symmetry of the perturbed flow field.

A detailed analysis of the influence of the blade number, angle and solidity on synchronous rotating instabilities is presented in [31] by Furukawa et al. 2002. It was found that the range of cavitation numbers for which it is possible to detect both attached uneven cavitation and alternate blade cavitation tends to be narrower for inducers with higher number of blades, longer blade length or higher blade angle.

Using a quasi-3D analytical model of steady cavitation in a 2-bladed inducer, in [40] Horiguchi et al. 2003b predicted that alternate blade cavitation starts to occur when the cavity length on the inducer blades reaches about 65% of the blade spacing, confirming the results obtained for rotating cavitation from simpler 2D analyses of blade cascades.

Fluid Dynamics Associated to Launcher Developers

An analysis of the characteristics of synchronous uneven cavitation on a 3-bladed inducer is presented in [73] by Shimagaki et al. 2006. Figure 5 shows the waterfall plot of mid-chord pressure fluctuations and the suction characteristic of the inducer at its design flow coefficient. A significant decrease of the head is present when synchronous asymmetric cavitation occurs, and the authors report that the head loss can be different depending on which inducer blade experiences the asymmetry in cavitation.

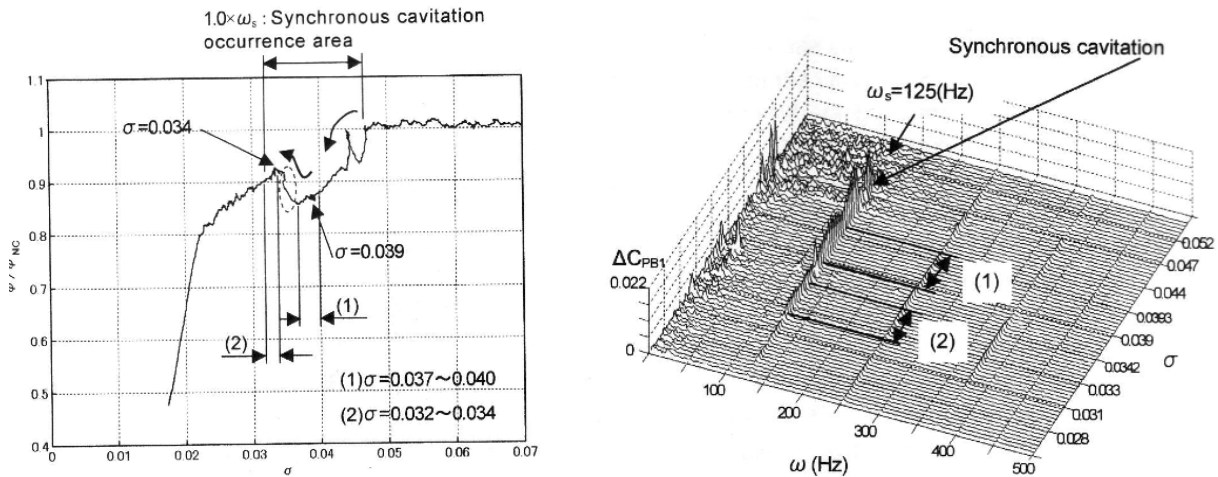


Figure 5. Left: suction performance curve of a 3-bladed inducer at the design flow coefficient. Right: waterfall plot of the power spectra of mid-chord pressure fluctuations, for the same flow conditions ([73] Shimagaki et al. 2006).

Finally, in [97] Yoshida et al. 2008 conducted a detailed experimental and numerical investigation to elucidate the mechanism of generation and development of asymmetric cavitation by means of measurements taken by pressure transducers installed along the blade channels. They reported that the synchronous blade vibration generated by uneven cavitation appeared to be a self-excited vibration, hydrodynamically coupled with the rotordynamic characteristics of the impeller.

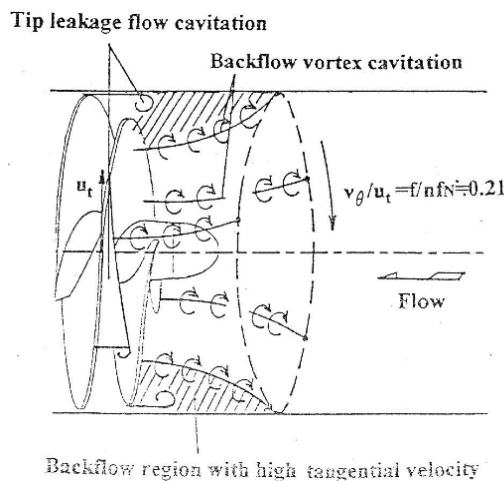


Figure 6. Schematic representation of the “backflow vortex cavitation” instability ([86] Tsujimoto et al. 1997).

Backflow vortex cavitation was first detected and identified by Tsujimoto et al. 1997, [86], in inducers operating at flow coefficients lower than design conditions and cavitation numbers either close to breakdown



or significantly higher (3-4 times the breakdown value). As illustrated in Figure 6, it is a rotating instability of the inducer backflow with the formation of multiple cells of axial vorticity (5 cells in [86]), which slowly rotate at an angular speed less than 0.2 times the inducer rotating speed.

The occurrence of a backflow vortex instability with 8 cells rotating at about 32% of the impeller speed has been documented in [100] by Zoladz 2000 with reference to the tests of the Fastrac turbopump. In [41] Imamura et al. 2003 showed that backflow vortex cavitation can be suppressed by means of J-grooves in the inducer casing, similar to those used for the control of rotating cavitation.

Rotating choke is another form of cavitation instability first identified by Tsujimoto and Semenov 2002, [85], and Semenov et al. 2004, [72], with reference to the phenomenon observed by Shimura et al. (2002), [75], and Uchiumi et al. 2003, [90], in the LH2 inducer of the Japanese H-II engine and indicated as “rotating stall cavitation”. It occurred near the inducer operational conditions (with a negative slope of the performance curve) at rotating speeds close to the second critical speed of the rotor, and was eventually eliminated by redesigning the inducer casing with slightly conical tip blade shape. Tsujimoto and Semenov 2002, [85], indicated that rotating choke is not related to blade stall as originally postulated, but rather to the transition of pumping performance from negative to positive slope when breakdown are approached, as illustrated in Figure 7.

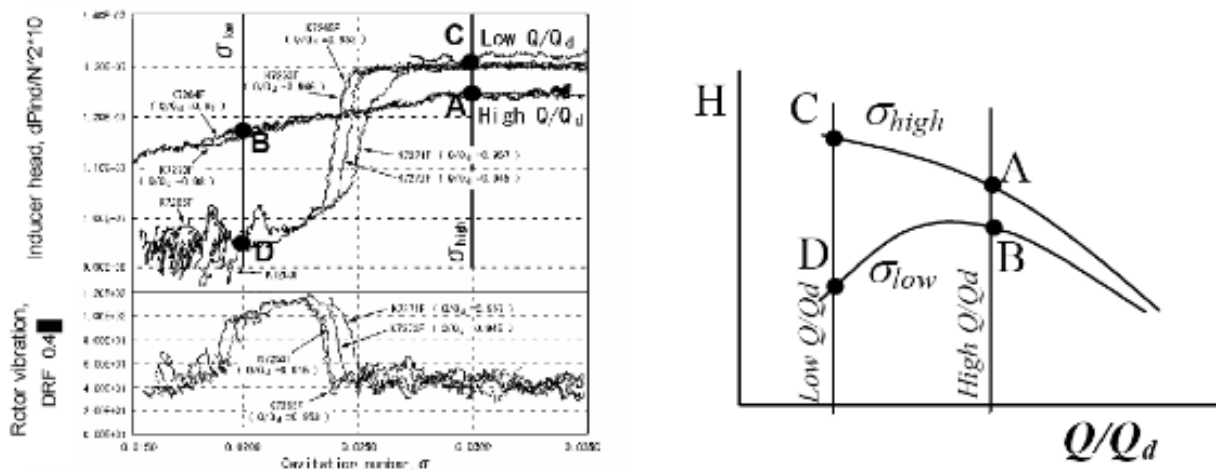


**Figure 7. Left: Suction performance and rotor vibration as a function of the cavitation number, at two different flow coefficients (95% and 98% of the operating conditions), for the liquid hydrogen inducer of the Japanese LE-7 engine. Right: schematic representation of the change of slope in the performance curve ([85] Tsujimoto and Semenov 2002).**

They proposed to name this instability “rotating choke” in order to highlight its dependence on the “choking” cavitation conditions that develop near inducer breakdown. As the Euler number decreases the cavities on the suction side of the blades increase, eventually “choking” the flow and rapidly increasing the head losses as soon as they extend into the throat between adjacent blades. If this head loss is sufficiently large the slope of the pumping characteristic becomes positive. Under these conditions choking in a blade channel propagates in the opposite direction of the inducer rotation with the same mechanism as for rotating stall.

A similar kind of “rotating stall” was observed by the author and his collaborators in a series of tests conducted in the Cavitating Pump Rotordynamic Test Facility at Alta, Pisa, Italy, on a 3-bladed commercial inducer ([13] Cervone et al. 2005) and, later, on a 2-bladed inducer with the same blade geometry of the 3-bladed LOX inducer for the Vinci engine ([14] Cervone et al. 2006b). In these tests, however, the

## Fluid Dynamics Associated to Launcher Developers

phenomenon was detected at high blade loads (flow coefficients lower than the design value) over a wide range of cavitation conditions, even if it was more intense near breakdown. The rotating nature of the phenomenon was later confirmed by flow visualization by means of a high-speed camera ([15] Cervone et al. 2007).

In a series of experiments on several inducers intended for use in liquid hydrogen Uchiumi and Kamijo 2008, [91], showed that “rotating stall cavitation” occurred when the flow incidence on the leading edges of the inducer was larger than about 43% of the tip blade angle measured from the tangential direction.

### 1.5 Cavitation Surge

Surge and cavitation surge (or cavitation auto-oscillation) are instabilities of pumping systems resulting in pressure and flow rate oscillations that can often generate excessive vibration and performance degradation of the machine and, in the worst case, even affect the integrity of the entire system.

With reference to Figure 8, consideration of the effects of small perturbations shows that the operational point O in the left diagram, at the intersection between the head characteristic and the load curve of the system, is quasi-statically stable if the slope of the load characteristic is larger than the slope of the pumping characteristic ([33], Greitzer 1981). Hence, for instance, point A in the right diagram is stable, B is neutrally stable and C is unstable. Operation of the machine under unstable conditions leads to the development of potentially dangerous large-amplitude surge oscillations both in compressors and pumps. As frequently observed in nonlinear dynamic oscillation, also surge instabilities of pumping systems usually display an hysteresis cycle ([33], Greitzer 1981).

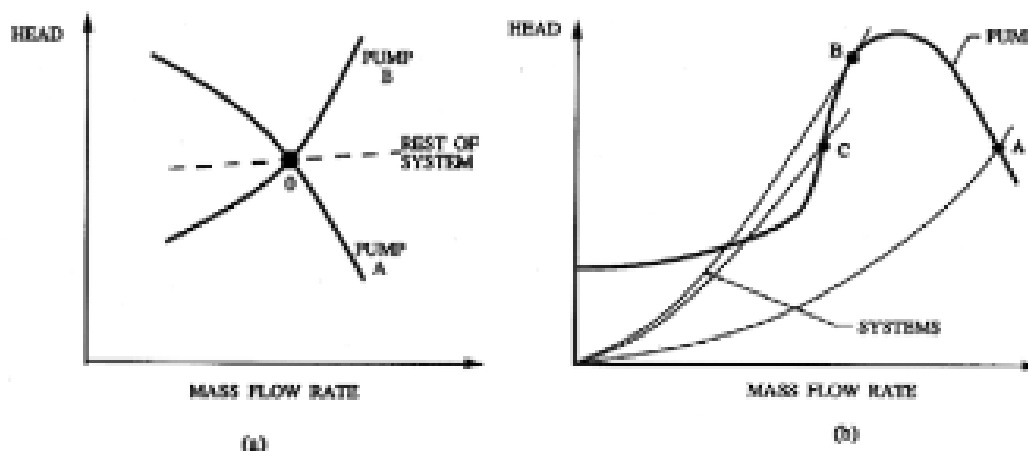


Figure 8. Schematic of stable and unstable characteristic curves of a pumping system ([8] Brennen 1994).

Clearly the rapid increase of the slope of the performance characteristic of cavitating turbopumps as breakdown is approached suggests that in these machines cavitation surge becomes increasingly more likely at low cavitation numbers. Indeed in cavitating pumps violent oscillations of the pressure and flow rate of the entire pumping system have routinely been observed when the cavitation number is decreased at values for which the head rise begins to be affected, as documented by Rosenman 1965, [66], Sack and Nottage 1965, [69], Natanzon et al. 1974, [60], Braisted and Brennen 1980, [1], among others. This surge phenomenon, named “cavitation auto-oscillation” in the original classification by Brennen 1994, [8], has been later indicated as “cavitation surge” by other researchers. It can lead to very large fluctuations across

the pumping system and can also cause substantial axial forces on the shaft, on the order of 20% of the steady axial thrust on the impeller. Braisted and Brennen 1980, [1], and later Yamamoto 1991, [94], showed that the frequency of cavitation surge oscillations is roughly proportional to the pump's rotating speed and the square root of the cavitation number.

With reference to space propulsion applications, the onset of cavitation surge is especially dangerous in liquid propellant rocket feed systems because the resulting flow rate fluctuations, by modulating the engine thrust, can trigger self-sustained POGO oscillations of the entire space vehicle, a global instability characterized by extremely dangerous large-amplitude fluctuations of the thrust, [56], NASA 1970.

A violent cavitation surge instability at very low frequency (<10 Hz) was observed by Hashimoto et al. 1997, [34] on a 3-bladed model of the liquid oxygen inducer of the Japanese LE-7 engine operating near breakdown conditions and at flow coefficients close to the nominal design value. The authors called this instability "low cycle oscillations" and reported a significant interaction with steady uneven cavitation and backflow vortices. A similar surge mode, but at higher frequency (about 18 Hz), was detected on a similar 3-bladed inducer by Tsujimoto et al. 1999, [86], who interpreted it as the result of a resonance between the vibration mode of the system at 18 Hz and the oscillations of the blade cavities due to the occurrence of rotating cavitation.

A surge-mode instability at about 2 Hz was detected by Furukawa et al. 2001, [30], in water tests on a 2-bladed inducer with a relatively high tip blade angle (about 11 degrees) operating near breakdown conditions at flow coefficients significantly lower than the nominal design value (Figure 9). The onset pressure of this instability mode is reported to coincide with the value for which the cavities on the blades reach the inlet of the blade channels.

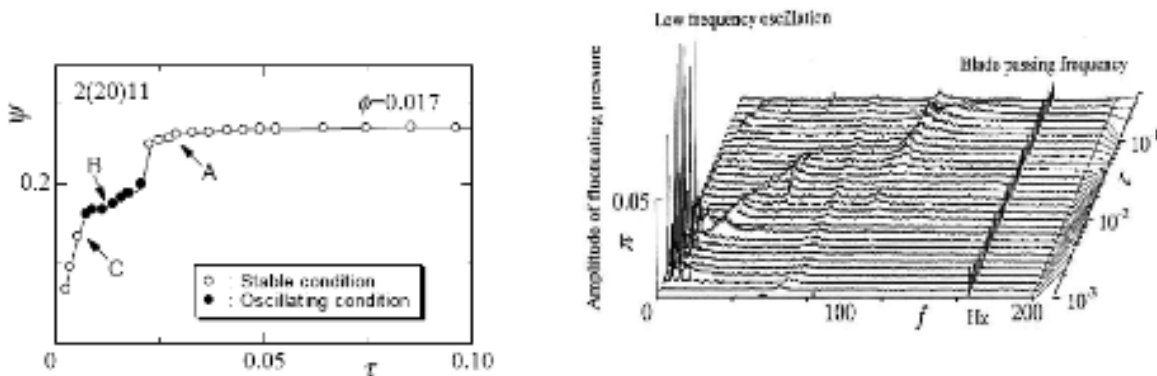


Figure 9. Left: suction performance curve of a 2-bladed inducer at  $\phi = 0.017$ , including the field of existence of the surge-mode instability. Right: waterfall plot of the power spectrum of outlet pressure fluctuations on the same inducer, under the same test conditions ([30] Furukawa et al. 2001).

The dependence of the frequency of cavitation surge on the Euler number is probably the consequence of a strong connection between this form of instability and rotating cavitation, as documented in [100] by Zoladz 2000 in connection with the tests carried out on the LOX turbopump of the Fastrac engine. If  $\Omega$  is the pump rotational speed,  $f_{rc}$  is the frequency of rotating cavitation instability and  $Z$  is the number of blades of the inducer, the frequency  $f$  of the cavitation surge mode is reported to be equal to

$$f = Z(f_{rc} - \Omega)$$

## Fluid Dynamics Associated to Launcher Developers

Several observations under different test conditions confirmed this relationship, which is also compatible with the cavitation surge frequencies reported by other research groups on different pumps.

The influence of number of blades, blade angle and blade solidity on the cavitation surge instability was investigated by Furukawa et al. 2002, [31], by means of experimental observations on several test inducers. It was found that:

- when the blade number is increased (and, consequently, the head rise is decreased), the range of cavitation numbers for which the cavitation surge is detected tends to become wider;
- when blade solidity is increased (by increasing the axial length of the blades) and head rise is therefore increased, the range of cavitation numbers for the existence of cavitation surge becomes narrower;
- finally, when the blade angle is decreased, the field of existence of the cavitation surge in terms of  $\sigma$  tends to be wider.

### 1.6 Higher Order Cavitation Instabilities

Free oscillation modes with frequencies significantly higher than the inducer rotational speed are generically indicated as higher-order instabilities and can involve unstable flow motion in the streamwise (higher-order surge modes) and azimuthal (higher-order rotating modes) directions. They have been detected and investigated in detail only in recent years and are universally recognized as extremely important in the design and characterization of space rocket inducers because of their potential for coupling with the lower critical speeds of the turbopump or with the flutter frequencies of the inducer blades, possibly leading to catastrophic failures of the machine. As an example, the failure of the Japanese H-II rocket in 1999 is thought to have been caused by the fatigue rupture of the inducer blades under the resonant excitation of an unstable high-order cavitation instability ([58] NASDA 2000a, [59] NASDA 2000b). Furthermore, several recent flight tests on important components of the Space Shuttle main engine have suffered from vibration problems at frequencies compatible with the characteristic frequencies of high-order rotating cavitation instabilities observed in the propellant feed turbopumps.

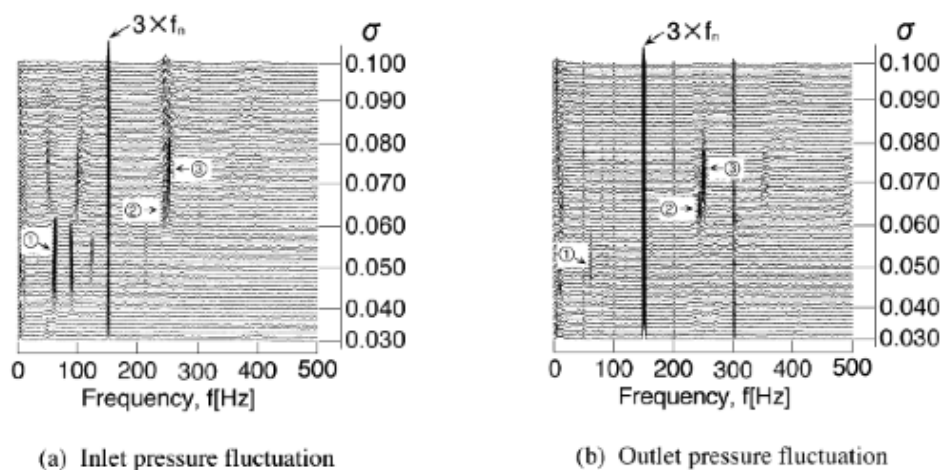


Figure 10. Waterfall plots of the power spectra of inlet and outlet pressure fluctuations in a 3-bladed inducer at flow coefficient  $\phi = 0.080$  ([28] Fujii et al. 2002).

High-order streamwise and azimuthal instabilities were first predicted on theoretical grounds by Tsujimoto 2001, [88], as unstable modes resulting from the application of his 2D linear cavity model originally developed for the investigation of rotating cavitation. He anticipated the occurrence of these modes with

system-independent frequencies between 4.2 and 4.7 times the inducer rotating speed and at Euler numbers equal or larger than about four times the breakdown value, just above those characteristic of conventional rotating cavitation. The author also suggested that the high-order azimuthal mode might be caused by the modulation of the inlet backflow structure, also in consideration that it was predicted to occur even without cavitation on the blades.

Experimental evidence of the occurrence of higher-order instabilities was first provided by Fujii et al. 2002, [28], in a test campaign on a 3-bladed inducer similar to the LOX inducer of the LE-7 turbopump, whose main results are illustrated in Figure 10. The spectral analysis of the pressure fluctuations, recorded at the inlet and outlet cross-sections of the inducer when operating at nearly nominal flow and variable inlet pressure, indicated the presence, together with conventional rotating cavitation denoted by 1 in the figure, of two additional higher-order instabilities:

- A higher-order surge (denoted by 2 in the figure) with a frequency about 5 times the rotational speed of the inducer at cavitation numbers higher than for conventional rotating cavitation.
- A higher-order rotating cavitation (denoted by 3 in the figure) at frequencies and cavitation numbers close to those of the higher-order surge oscillations. It was also found that the cavity size fluctuation for this instability mode is smaller than for conventional rotating cavitation. Furthermore, while in conventional rotating cavitation the outlet pressure fluctuations are significantly smaller than those at the inlet, for the higher-order rotating cavitation mode the situation is reversed.

In the same paper the authors also indicate that the above instabilities could be eliminated almost completely by means of the introduction of a suitable step in the design of the inducer casing. Finally, the detection of a higher-order surge instability with the same features observed by Fujii et al. 2002, [28], was confirmed by Tsujimoto and Semenov 2002, [85], also in full-scale tests on the liquid hydrogen turbopump of the LE-7 engine.

Figure 11 summarizes the results of similar tests conducted in the U.S. by Subbaraman and Patton 2006, [78], on a 4-bladed inducer for the characterization of higher-order instabilities at frequencies up to ten times the rotational speed of the impeller.

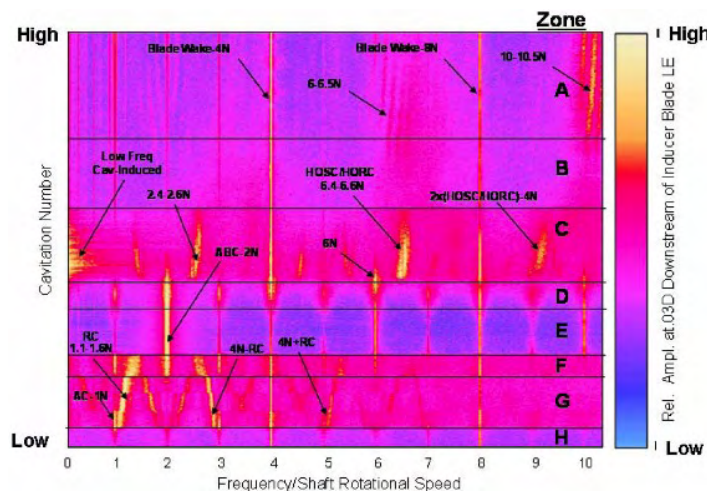


Figure 11. 2D Color plot of the power spectra of the pressure fluctuations v/s the cavitation number in a 4-bladed inducer, at a flow coefficient equal to 1.02 times the design value ([78] Subbaraman and Patton 2006).

The plot in the figure clearly shows the occurrence of higher order surge cavitation (HOSC) and higher order

## Fluid Dynamics Associated to Launcher Developers

---

rotating cavitation (HORC) at nearly nominal flow conditions and cavitation numbers equal to or higher than about four times the breakdown value. The HORC and HOSC frequencies only differ by about one tenth of the inducer rotational speed and, not surprisingly, the HORC component displays both forward and backward running modes. These higher-order instabilities also produced many nonlinear modulations and harmonics over the whole range of experimental observation, including a component at very low frequency indicated as “Low Freq Cav-Induced” in the above plot. The most intense harmonic component occurred at a frequency equal to 6.4-6.6 times the rotational speed, which was therefore considered as the “nominal” frequency of the instability.

The author present in the paper a “Tip Vortex Suppressor”, consisting of some devices able to provide a re-circulate flow from the inducer discharge to the inducer inlet. This device showed to be quite effective, shifting the higher-order phenomena to low values of the flow coefficient (significantly lower than the operating point) and eventually suppressing most of them when an additional through flow was provided by the device. However, in the latter case the detected oscillations due to alternate blade cavitation were significantly stronger.

A higher-order surge mode was detected by Cervone et al. 2006b, [14], on a 2-bladed inducer with the same blade geometry of the 3-bladed LOX inducer for the Vinci engine. Two harmonics of the phenomenon have been identified, at 4.4 and 6.6 times the inducer rotational speed. The phenomenon was observed at all values of the flow coefficient and cavitation number, but became more evident at higher flow rates near the design point and tended to disappear as breakdown conditions were approached.

## 2.0 ON THE DESIGN OF HIGH-HEAD INDUCERS

### 2.1 Introduction

As mentioned earlier, current rocket propellant feed turbopumps often employ an inducer upstream of the centrifugal stage in order to pre-pressurize the flow to the main centrifugal pump, avoid unacceptable cavitation, improve the suction performance and reduce the propellant tank pressure and weight.

Over time the typical inducer geometry has evolved as schematically indicated in Figure 12, taken from [42] Jakobsen 1971. Earlier low-head inducers are essentially axial flow impellers, with constant-pitch helical blading and roughly uniform mean radius. Today's high-head inducers, with tapered hubs, nearly cylindrical casings and variable-pitch blades, are instead more similar to mixed-flow machines, where a significant portion of the pressure rise is obtained from the work developed by centrifugal forces as a consequence of the radial displacement of the fluid through the impeller. Compared to centrifugal pump impellers, typical inducers have fewer blades (usually 3 or 4), lower flow coefficients (from 0.05 to 0.1), larger stagger angles (70 to 85 deg) and significantly higher blade solidities (between 1.5 and 2.5). Long blades with small angles of attack provide ample time and room for the collapse of the cavitation bubbles and for the gradual exchange of energy with the flow. The resulting configuration, even though beneficial from the standpoint of cavitation performance, results in relatively low values of the inducer efficiency due to the highly viscous, turbulent and dissipative flow inside the blade passages.

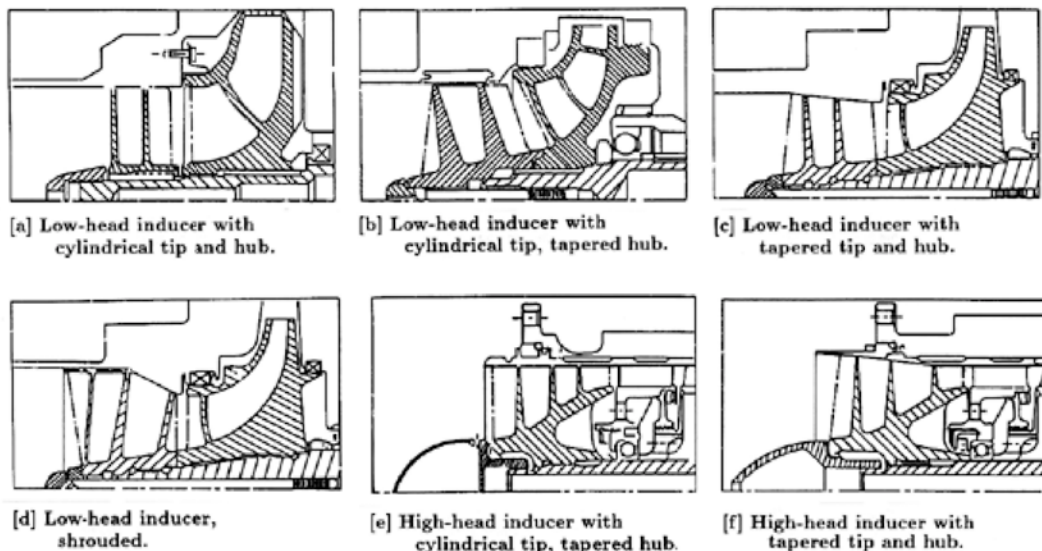


Figure 12. Typical geometries of cavitating inducers (from [42] Jakobsen 1971).

The development of 3D theoretical models capable of rapidly predicting the performance of axial inducers in order to provide indications for the preliminary design of the machine is of particular interest to rocket engineers. However, not many such models have been proposed so far, probably due to the difficulty of adequately describing the 3D flow field inside the inducer blades. Therefore, designers often refer to simple “rules of thumb”, or to the general indications of design manuals, such as the one published by [56] NASA 1971. In the last decades, numerical simulation of the complex 3D features of inducer flows has emerged as a promising tool for design validation and refinement (see, as an example, [1] Ashihara et al. 2002, [47] Kang et al. 2007), but its use in the early stages of design still remains impractical.

## Fluid Dynamics Associated to Launcher Developers

A number of 2D reduced order models for the prediction of the noncavitating flow in turbopump inducers are illustrated by [8] Brennen 1994 and [9] Brennen 1995). These models are based on linear and radial cascade analyses with semi-empirical inclusion of flow deviation and viscous effects. Three-dimensional corrections for inlet flow prerotation, tip leakage and discharge flow are also indicated.

A second class of models has been aimed at the prediction of the effects of cavitation on inducer performance ([77] Stripling and Acosta 1962, [10] Brennen and Acosta 1973, [7] Brennen 1978). These models are essentially two-dimensional, where cavitation is assimilated to a vapor layer on the blade or a mixture of bubbles and liquid. Early studies opened the way to a number of more recent analyses capable of better understanding and predicting the major flow instabilities affecting cavitating inducers ([84] Tsujimoto et al. 1993, [87] Tsujimoto et al. 1998, [93] Watanabe et al. 1999, [18] d'Agostino and Venturini-Autieri 2002, [19] d'Agostino and Venturini-Autieri 2003, [72] Semenov et al. 2004).

Some earlier analyses of single and two phase flow in inducers have been carried out, among others, by [16] Cooper 1967. More recently, [52] Lakshminarayana 1982 addressed the problem of performance prediction of noncavitating inducers by the combined use of a simplified radial equilibrium analysis and the Euler equation. Viscous effects are taken into account through an empirical loss coefficient deduced from the reported performance of inducers documented in the literature. Indications on the effects of solidity and number of blades are also provided.

In [6] Bramanti et al. 2007 developed a simplified model based on the traditional throughflow theory approximations with empirical corrections for incidence, friction and deviation losses of the flow through the inducer blades. The model proved to be in good agreement with the reported performance of several inducers tested in different facilities worldwide and represented the basis for the development of the work illustrated in this paper.

The present model is based on the incompressible, inviscid, irrotational flow approximation, where the 3D velocity field inside the blade channels is expressed as the superposition of a fully-guided axisymmetric flow with radially uniform axial velocity and a 2D cross-sectional vorticity correction. Boundary layer blockage is estimated by means of a suitable redefinition of the diffusion factor for bladings with non-negligible radial flow and Carter's rule is used to account for flow deviation at the inducer trailing edge. Performance losses are evaluated by adding suitably adapted correlations of turbulent duct losses to the inlet flow incidence losses. Conservation of mass and angular momentum are used to model the flow transition from the inducer trailing edge to the axisymmetric downstream flow, thus accounting for the majority of mixing losses occurring at the inducer exit. Model validation has been carried out against the experimental data obtained from two space inducers tested in the Cavitating Pump Rotordynamic Test Facility at Alta, as well as from a number of inducers documented in the open literature.

## 2.1 Inducer Flow and Geometry

### 2.1.1 Flow Velocity

The incompressible, inviscid and irrotational flow through a helical inducer with  $N$  radial blades, rotational speed  $\Omega$ , constant tip radius  $r_T$ , tapered hub radius  $r_H$  and variable axial pitch  $P$  and blade angle  $\gamma$  (as schematically shown in Figure 13), is held by the equations:

$$\nabla \cdot \mathbf{u} = 0 \quad \text{and} \quad \nabla \times \mathbf{u} = 0$$



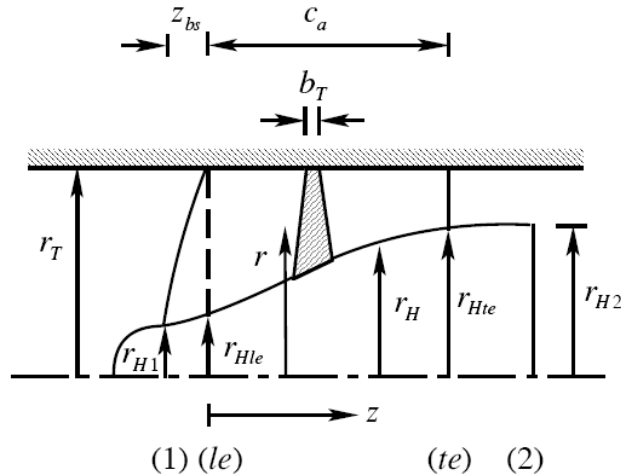


Figure 13. Inducer schematic and nomenclature.

The relatively large value of the blade solidity typical of inducers designed for controlling cavitation in highly loaded turbopumps suggests that near design conditions ( $\Phi \approx \Phi_D$ ) the 3D velocity  $\mathbf{u}$  in the blade channels can be approximated by the superposition of a fully-guided axisymmetric flow  $\hat{\mathbf{u}}$  with radially uniform axial velocity component  $\hat{w}$  and a 2D cross-sectional slip velocity correction  $\tilde{\mathbf{u}}$  (Figure 14):

$$\mathbf{u} = \hat{\mathbf{u}} + \tilde{\mathbf{u}}$$

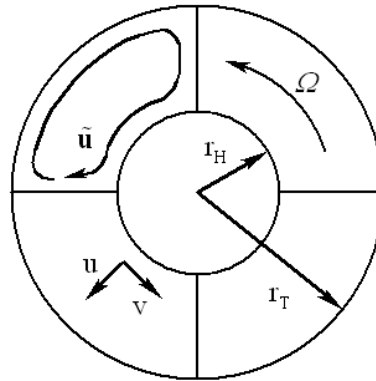


Figure 14. Schematic of the 2D cross-sectional slip velocity correction in the inducer blade channels.

With reference to the velocity triangles of Figure 15, for radial helical blades:

$$\tan \gamma = \frac{2\pi r}{P} \Rightarrow \begin{cases} \hat{v} = \Omega r - \hat{w} \tan \gamma = \Omega r - 2\pi r \frac{\hat{w}}{P} \\ \hat{w} = \frac{\dot{m}}{\rho \pi (r_T^2 - r_H^2) B} = \frac{\Phi \Omega r_T^3}{(r_T^2 - r_H^2) B} \end{cases}$$

where  $0 \leq B \leq 1$  is the average cross-sectional blockage due to boundary layer displacement effects and, if

Fluid Dynamics Associated to Launcher Developers

significant, to blade thickness. The 2D slip velocity components are most synthetically expressed and solved in terms of a scalar stream function  $\psi(r', \vartheta')$  in the rotating cylindrical coordinates  $r' = r$ ,  $\vartheta' = \vartheta - \Omega t$ ,  $z' = z$ :

$$\tilde{u} = \frac{1}{r'} \frac{\partial \psi}{\partial \vartheta'} \text{ and } \tilde{v} = -\frac{\partial \psi}{\partial r'}$$

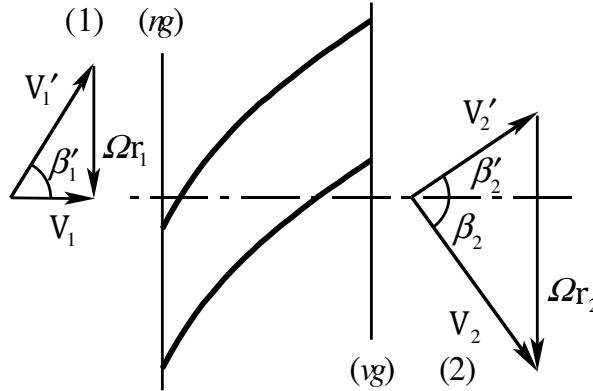


Figure 15. Velocity triangles.

2.1.2 Inducer Pitch and Hub Radius

Substitution of the assumed velocity field in the expressions of the incompressibility and irrotationality conditions in cylindrical coordinates  $r, \vartheta, z$  yields:

$$\frac{\partial(r\hat{u})}{\partial r} = -r \frac{d\hat{w}}{dz}$$

$$\frac{d}{dz} \left( \frac{\hat{w}}{P} \right) = 0$$

$$\frac{d^2 \hat{w}}{dz^2} = 0$$

$$\frac{1}{r} \frac{\partial}{\partial r} \left( r \frac{\partial \psi}{\partial r} \right) + \frac{1}{r^2} \frac{\partial^2 \psi}{\partial \vartheta'^2} = 2\Omega - 4\pi \frac{\hat{w}}{P}$$

Integration of  $d^2 \hat{w} / dz^2 = 0$  with the boundary conditions  $\hat{w}(0) = \hat{w}_{le}$  and  $\hat{w}(c_a) = \hat{w}_{te}$  at the axial locations bounding the full-height portion of the blades (indexes  $le$  and  $te$ ) yields:

$$\frac{d\hat{w}}{dz} = \frac{\hat{w}_{te} - \hat{w}_{le}}{c_a} = \text{constant}$$

and the following expression for the axial velocity:

$$\hat{w} = \hat{w}_{le} + (\hat{w}_{te} - \hat{w}_{le}) \frac{z}{c_a}$$

Similarly, by integrating the continuity equation with the impermeability condition  $\hat{u}(r_T) = 0$  at the tip radius, the following expression for the radial velocity is obtained:

$$\hat{u} = \frac{1}{2} \frac{d\hat{w}}{dz} \left( \frac{r_T^2}{r} - r \right)$$

Finally, by evaluating  $\hat{w}$  at design conditions (index  $D$ ) by means of the continuity equation and integrating  $d(\hat{w}/P)/dz = 0$  with  $P(w_{leD}) = P_{Te}$  at  $z = 0$ , the following expressions for matching the axial changes of the hub radius  $r_H$  and blade pitch  $P$  are obtained:

$$\frac{1}{(r_T^2 - r_H^2)B} = \frac{1}{(r_T^2 - r_{He}^2)B_{le}} + \left[ \frac{1}{(r_T^2 - r_{He}^2)B_{te}} - \frac{1}{(r_T^2 - r_{He}^2)B_{le}} \right] \frac{z}{c_a}$$

$$P = P_{Te} \frac{\hat{w}_D}{\hat{w}_{leD}} = P_{Te} + P'z$$

where:

$$P' = \left[ \frac{(r_T^2 - r_{He}^2)B_{le}}{(r_T^2 - r_{He}^2)B_{te}} - 1 \right] \frac{P_{Te}}{c_a}$$

and a linear axial variation of the blockage:

$$B = B_{le} + (B_{te} - B_{le}) \frac{z}{c_a}$$

can be approximately assumed inside the blade passages from the leading edge station ( $le$ ), where  $B = B_{le} \approx 1$ , to the trailing edge ( $te$ ), where  $B = B_{te}$ .

### 2.1.3 Slip Flow

Finally, on each channel cross-section the Poisson's equation for the stream function can be conformally mapped in a rectangular domain and integrated by standard methods ([38] Hildebrand 1976) with the condition  $\psi = 0$  on the boundary to:

$$\psi = - \sum_{m=1}^{+\infty} \sum_{n=1}^{+\infty} C_{m,n} \sin \left[ m\pi \frac{\ln(r/r_H)}{\ln(r_T/r_H)} \right] \sin \frac{(2n-1)N\vartheta'}{2}$$

where:

Fluid Dynamics Associated to Launcher Developers

$$C_{m,n} = \frac{A_{m,n}}{m^2 \pi^2 / \ln^2(r_T/r_H) + (n - \frac{1}{2})^2 N^2}$$

with:

$$A_{m,n} = Kr_H^2 \frac{m / (n - \frac{1}{2}) \ln^2(r_T/r_H)}{1 + m^2 \pi^2 / 4 \ln^2(r_T/r_H)} \left[ 1 - (-1)^m \frac{r_T^2}{r_H^2} \right]$$

and:

$$K = 2\Omega - 4\pi \frac{\hat{w}}{P} = 2\Omega \left[ 1 - \frac{2\pi\Phi r_T^3}{P(r_T^2 - r_H^2)} \right]$$

from which the radial and tangential slip velocity components  $\tilde{u}$  and  $\tilde{v}$  are readily computed.

**2.1.4 Blade Loading and Boundary Layer Blockage**

With reference to Figure 16, suitable redefinition of the diffusion factor for axial bladings ([53] Lieblein et al. 1953) to the case of tapered inducers with non-negligible radial flow:

$$D = \frac{V'_1 - V'_2}{V'_1} + \frac{|v_2 - v_1|}{2\sigma V'_1} = \frac{p_2 - p_1}{\frac{1}{2}\rho V'_1(V'_1 + V'_2)} + \frac{p_{t2} - p_{t1}}{\sigma\rho\Omega(r_1 + r_2)V'_1}$$

allows for the control of the blade loading (a crucial design aspect under cavitating conditions) and the estimate of the boundary layer blockage at nominal flow conditions.

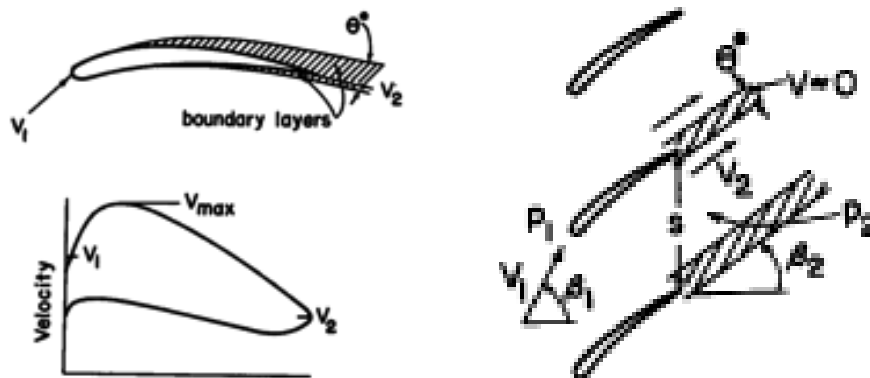


Figure 16. Nomenclature for blade boundary layer (left) and linear cascade (right).

By evaluating:

$$p_2 - p_1 = \frac{1}{2}\rho(V_1'^2 - V_2'^2) - \frac{1}{2}\rho\Omega^2(r_1^2 - r_2^2) \quad \text{and} \quad p_{t2} - p_{t1} = \rho\Omega(r_2v_2 - r_1v_1)$$

with the Bernoulli's and Euler's equations for mixed-flow bladings and substituting in the above expression

for  $D$ , obtain:

$$D \approx \frac{V'_1 - V'_2}{V'_1} - \frac{\Omega^2 (r_1^2 - r_2^2)}{V'_1 (V'_1 + V'_2)} + \frac{r_2 v_2 - r_1 v_1}{\sigma (r_1 + r_2) V'_1}$$

Here all relevant properties including the solidity  $\sigma = c/s$  are evaluated on the mean streamline:

$$r = r_M = \sqrt{\frac{r_T^2 + r_H^2}{2}}$$

and, for flow with no inlet prerotation and fully guided at the inducer outlet ( $v_1 \approx 0$  and  $v'_2 \approx w_{te} \tan \gamma_{te}$ ), the relative velocities are expressed by:

$$V'_1 = \sqrt{w_1^2 + v_1'^2} = \sqrt{\left(\frac{\Phi_D \Omega r_T^3}{r_T^2 - r_{H2}^2}\right)^2 + \Omega^2 r^2} \quad \text{and} \quad V'_2 = \sqrt{w_2^2 + v_2'^2} = \frac{\Phi_D \Omega r_T^3}{(r_T^2 - r_{H2}^2) \cos \gamma_{te}}$$

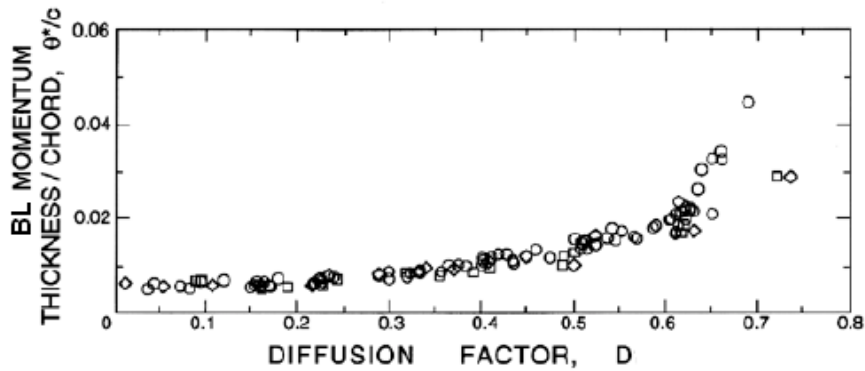


Figure 17. Ratio of the momentum thickness  $\theta^*$  of the blade boundary layer to the chord  $c$  as a function of the diffusion factor  $D$ , for axial cascades with three different profiles (adapted from [8], Brennen 1994).

As illustrated in Figure 17, in turbulent boundary layers over blade cascades the diffusion factor is directly correlated to the momentum thickness  $\theta^*$  ([54] Leiblein 1965, [8] Brennen 1994):

$$\frac{\theta^*}{c} = f(D)$$

and, in turn, for turbulent boundary layers, also to the displacement thickness by the relation  $\delta^* \approx 1.3\theta^*$ . With these results, the blade boundary layer blockage at the inducer trailing edge is computed as:

$$B_{te} = 1 - \frac{2\delta^*}{s_{te} \cos \gamma_{te}}$$

## Fluid Dynamics Associated to Launcher Developers

(Figure 16), where the blade spacing  $s_{le} = 2\pi r_{le}/N$  is evaluated at the mean radius.

### 2.1.5 Mean Radius, Chord and Solidity

On a relative streamline of the fully-guided flow:

$$\frac{dr}{\hat{u}'} = \frac{rd\vartheta'}{\hat{v}'} = \frac{dz}{\hat{w}'}$$

where from earlier results:

$$\hat{u}' = \hat{u} = \frac{1}{2} P' \frac{\hat{w}_{le}}{P_{tle}} \left( \frac{r_T^2}{r} - r \right)$$

$$\hat{v}' = \Omega r - \hat{v} = 2\pi r \frac{\hat{w}_{le}}{P_{tle}}$$

$$\hat{w}' = \hat{w} = \frac{\hat{w}_{le}}{P_{tle}} (P_{tle} + P'z)$$

Hence, integrating with initial conditions  $r_{Mle}, \vartheta'_{Mle}, z_{Mle}$ , the equations of the mean streamline are:

$$r_M = \sqrt{r_T^2 - (r_T^2 - r_{le}^2) \frac{P_{tle} + P'z_{Mle}}{P_{tle} + P'z_M}}$$

$$\vartheta'_M = \vartheta'_{Mle} + \frac{2\pi}{P'} \ln \frac{P_{tle} + P'z_M}{P_{tle} + P'z_{Mle}}$$

The mean values of the blade chord and solidity are then evaluated as:

$$c = \int_{z_{Mle}}^{c_a} dz_M \sqrt{\left( \frac{\partial r_M}{\partial z_M} \right)^2 + \left( r_M \frac{\partial \vartheta'_M}{\partial z_M} \right)^2 + 1}$$

$$\sigma = \int_{z_{Mle}}^{c_a} \frac{dc}{S_M} = \int_0^{c_a} \frac{dz_M}{2\pi r_M/N} \sqrt{\left( \frac{\partial r_M}{\partial z_M} \right)^2 + \left( r_M \frac{\partial \vartheta'_M}{\partial z_M} \right)^2 + 1}$$

## 2.1 Inducer Performance Modeling

### 2.1.1 Discharge Flow

In the assumption of uniform inlet flow to the inducer with no prerotation ( $v_1 = 0$ ), radial differentiation of the incompressible isentropic Euler equation:

$$\frac{p_2}{\rho} + \frac{1}{2}(v_2^2 + w_2^2) - \frac{p_1}{\rho} - \frac{1}{2}(v_1^2 + w_1^2) = \Omega(r_2 v_2 - r_1 v_1)$$

for the axisymmetric flow at sections (1) and (2) of Figure 13 and elimination of the pressure by means of the radial equilibrium condition:

$$\frac{v^2}{r} = \frac{1}{\rho} \frac{\partial p}{\partial r}$$

yields the following ODE for the axial and tangential velocity profiles  $w_2(r_2)$  and  $v_2(r_2)$  at the inducer discharge section:

$$\frac{1}{2} \frac{dw_2^2}{dr_2} + \left( \frac{v_2}{r_2} - \Omega \right) \frac{d(r_2 v_2)}{dr_2} = 0$$

In order to solve the above equation for the axial velocity profile it is necessary to establish a correlation between  $w_2$  and the azimuthal velocity  $v_2$ . To this purpose the fully guided flow with uniform axial velocity and slip vorticity correction at the inducer trailing edge (station  $te$ ):

$$u_{te} = \tilde{u}_{te}$$

$$v_{te} = \Omega r_{te} - w_{te} \frac{r_{te}}{r_T} \tan \gamma_{Tte} + \tilde{v}_{te}$$

$$w_{te} = \frac{\Phi \Omega r_T^3}{r_T^2 - r_{He}^2}$$

is assumed to mix into an axisymmetric swirled axial flow with velocities  $v_2$  and  $w_2$  at the discharge section (station 2), while satisfying mass continuity and, in the absence of wall friction, conserving the axial component of angular momentum:

$$2\pi w_2 r_2 dr_2 = 2\pi w_{te} r_{te} dr_{te}$$

$$2\pi w_2 v_2 r_2^2 dr_2 = w_{te} r_{te}^2 dr_{te} \int_0^{2\pi} v_{te} d\vartheta'$$

Integration of the second equation with earlier expressions of  $v_{te}$  and  $\tilde{v}_{te}$  yields:

$$v_2 = \frac{r_{te}}{r_2} \left[ \Omega r_{te} - w_{te} \frac{r_{te}}{r_T} \tan \gamma_{Tte} + \tilde{v}_s(r_{te}) \right]$$

where:

**Fluid Dynamics Associated to Launcher Developers**

$$\tilde{v}_s(r_{ie}) = \frac{1}{r_{ie}} \sum_{m=1}^{+\infty} \sum_{n=1}^{+\infty} \frac{mC_{m,n}}{(n-\frac{1}{2}) \ln(r_T/r_H)} \cos \left[ m\pi \frac{\ln(r_{ie}/r_{He})}{\ln(r_T/r_H)} \right]$$

Finally, substitution in the ODE for the axial velocity profile where, from the mass balance:

$$\frac{d}{dr_2} = \frac{dr_{ie}}{dr_2} \frac{d}{dr_{ie}} = \frac{w_2 r_2}{w_{ie} r_{ie}} \frac{d}{dr_{ie}} \quad \text{and} \quad \frac{dr_{ie}^2}{dr_2^2} = \frac{w_2}{w_{ie}}$$

results in the following BVP (boundary value problem) for  $w_2$  and  $r_{ie}$  as functions of  $r_2^2$ :

$$\frac{dw_2}{dr_2^2} = \frac{1}{2w_{ie}} \left[ \Omega - \left( \Omega - \frac{w_{ie}}{r_T} \tan \gamma_{Tie} + \frac{\tilde{v}_s(r_{ie})}{r_{ie}} \right) \frac{r_{ie}^2}{r_2^2} \right] \left\{ 2\Omega - 2 \frac{w_{ie}}{r_T} \tan \gamma_{Tie} + \frac{1}{r_{ie}} \frac{d}{dr_{ie}} [r_{ie} \tilde{v}_s(r_{ie})] \right\}$$

$$\frac{dr_{ie}^2}{dr_2^2} = \frac{w_2}{w_{ie}}$$

The above problem can then be solved by numerical shooting from  $r_{H2}^2$  to  $r_T^2$  with initial conditions:

$$w_2(r_{H2}^2) = w_{H2} \quad \text{and} \quad r_{ie}^2(r_{H2}^2) = r_{He}^2$$

iterating on the assumed value of  $w_{H2}$  until the final boundary condition  $r_{ie}^2(r_T^2) = r_T^2$  is satisfied.

A closed form approximation of the axial velocity profile  $w_2(r_2)$  can also be obtained by assuming  $r_{ie} \approx r_2$  in the expression of  $v_2$  and neglecting  $\tilde{v}_s$  in:

$$\frac{v_2}{r_2} - \Omega = -\frac{w_2}{r_T} \tan \gamma_{T2} + \frac{\tilde{v}_s}{r_2} \approx -\frac{w_2}{r_T} \tan \gamma_{T2}$$

Then the ODE for the axial velocity profile becomes:

$$\frac{dw_2}{dr_2} - \frac{1}{r_T} \tan \gamma_{T2} \frac{d(r_2 v_2)}{dr_2} = 0$$

whose closed form solution is:

$$w_2(r_2) = \frac{[\Omega r_2 + \tilde{v}_s(r_2)](r_2/r_T) \tan \gamma_{T2} + c}{1 + (r_2^2/r_T^2) \tan^2 \gamma_{T2}}$$

with the integration constant  $c$  determined by the mass balance between the inlet and discharge cross-sections:

$$\int_{r_{H2}}^{r_T} w_2 2\pi r_2 dr_2 = \int_{r_{H1}}^{r_T} w_1 2\pi r_1 dr_1$$



### 2.1.2 Flow Losses

The assumptions of inviscid flow fully-guided at the inducer trailing edge are not accurately satisfied in practice. In order to better approximate the actual pumping characteristic of noncavitating inducers the main sources of performance degradation (flow incidence, friction and deviation) have to be accounted for.

Friction losses in the blade channels are evaluated by means of standard correlations for turbulent duct flows:

$$\Delta p_{friction} = f \frac{L_{ch}}{D_{ch}} \frac{1}{2} \rho V_1'^2$$

where the friction factor  $f$  depends on the Reynolds number based on the hydraulic diameter  $D_{ch}$  of the blade channels,  $L_{ch}$  is the effective channel length evaluated along the mean streamline, and  $V_1'$  is the relative flow velocity at the mean inlet radius.

Incidence losses due to the sudden change of the flow direction at the leading edge of the inducer blades are expressed in terms of a nondimensional equivalent length  $L_{eq}/D_{ch}$ , function of the incidence angle evaluated on the mean streamline. Hence, the overall pressure losses can be written as follows

$$\Delta p_{loss} = f \left( \frac{L_{ch}}{D_{ch}} + \frac{L_{eq}}{D_{ch}} \right) \frac{1}{2} \rho V_1'^2$$

### 2.1.3 Flow Deviation

The mean value of the exit flow deviation is evaluated at the mean radius using Carter's correlation:

$$\delta^\circ \approx \frac{m_c}{\sqrt{\sigma}} (\gamma_{le} - \gamma_{te})$$

and applied to correct the discharge flow direction at all radii in the inducer annulus. In order to better match the experimental data, the standard correlation for the coefficient  $m_c$  has been slightly modified according to the equation

$$m_c \approx 1.22 \left[ 0.23 \left( \frac{2a}{c} \right)^2 + 0.1 \left( \frac{\gamma_{te}}{50^\circ} \right) \right]$$

where  $a \approx c/2$  is the relative position of the maximum camber point from the blade leading edge. Hence, the azimuthal flow velocity at the inducer discharge section (2) with flow deviation corrections becomes:

$$v_{2\delta^\circ} = \Omega r - w_2 \tan(\beta_2' + \delta^\circ)$$

where

$$\beta_2' = \tan^{-1} \left( \frac{\Omega r - v_2}{w_2} \right)$$

**Fluid Dynamics Associated to Launcher Developers**

**2.1.4 Pumping Performance**

With the above results, the pumping performance is readily evaluated from the Euler equation:

$$p_{t2} - p_{t1} = p_2 - p_1 + \frac{1}{2} \rho (v_{2\delta}^2 + w_2^2 - w_1^2) = \rho \Omega r_2 v_{2\delta} - \Delta p_{loss}$$

Hence, by mass averaging the pressure changes, the total and static head coefficients are expressed by:

$$\Psi_t = \frac{1}{\Omega^2 r_T^2 \dot{m}} \int_{r_{H2}}^{r_T} (p_{t2} - p_{t1}) w_2 2\pi r_2 dr_2$$

$$\Psi = \frac{1}{\Omega^2 r_T^2 \dot{m}} \int_{r_{H2}}^{r_T} (p_2 - p_1) w_2 2\pi r_2 dr_2$$

The entire flow has therefore been solved in terms of the stated input data and parameters.

**2.1 Model Discussion and Validation**

With reference to the definition of the inducer geometry, in the stated assumptions and approximations the requirement for radially uniform axial velocity in the blade channels at design conditions determines the relationship between the axial schedules of the hub radius and blade pitch angle of helical inducers. If, in particular, the hub-to-tip radius ratio is known at the leading and trailing edge sections and the design flow coefficient and leading edge blade angle are assigned, then all of the main geometric features of tapered hub helical inducers can be derived, including the trailing edge pitch angle. Comparison with the MK1 and FAST2 space inducers, produced by Avio and previously tested in Alta’s Cavitating Pump Rotordynamic Test Facility, confirmed that the proposed model actually generates quite realistic geometries of high-head inducers.

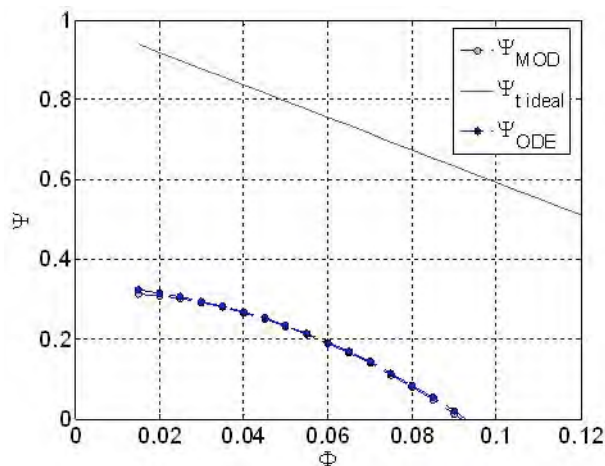


**Figure 18. Comparison between the numerical solution (ODE) and the corresponding closed form approximation (MOD) for the noncavitating performance prediction of tapered inducers.**

With reference to the inducer performance evaluation, it is first worth noticing that the numerical solution of the BVP for the discharge velocity profiles and the corresponding closed form approximation lead to

**Fluid Dynamics Associated to Launcher Developers**

essentially equivalent results, as illustrated by the comparison of the noncavitating pumping characteristics shown in Figure 18. Only for significantly low values of the flow coefficient ( $\Phi < 0.02$ ), when the slip velocity becomes comparable to the axial velocity, a small difference between the two curves can be observed.

Upon implementation of the model in a MathLab code, the geometric definition of the inducer satisfying a given set of input data and parameters and the prediction of its noncavitating characteristic curve is accomplished in about 30 s on today’s personal computers (and clearly much less when using more efficient programming languages), allowing for real-time interactive design of the machine and opening the way for the effective application of parametric optimization methods.

The model has been validated against the experimental performance of six different tapered-hub inducers, whose main characteristics are summarized in Table 2. Information on inducers A, B, C and D comes from the open Japanese literature. Specifically, the experimental data on inducers A and B have been taken from [34] Hashimoto et. al. 1997 and refer to two different LOX pumps. The tests of inducer C are documented in [28] Fujii et. al. 2002. Finally, inducer D is used in the LE-7A HTP and its experimental performance is reported in [29] Fujii et. al. 2005.

**Table 2. Geometrical characteristics of the inducers used for validation of the proposed model.**

	MK1	FAST2	INDUCER A	INDUCER B	INDUCER C	INDUCER D
<b>Number of blades</b>	4	2	3	4	3	3
<b>Tip diameter, mm</b>	168.0	82.2	127.4	127.4	149.8	174.0
<b>Inlet tip blade angle, deg</b>	82.36	82.62	82.75	82.75	82.5	83.6
<b>Outlet blade angle, deg</b>	73.4 medium	68.76 medium	80.75 tip	80.75 tip	81.0 tip	78.9 tip
<b>Hub/tip at inlet</b>	0.428	0.365	0.300	0.300	0.250	0.287
<b>Hub/tip at outlet</b>	0.690	0.685	0.500	0.500	0.500	0.460
<b>Solidity at tip</b>	2.1	1.59	2.7	3.0	1.91	2.1

Figure 19 and Figure 20 compare the experimental noncavitating characteristics of the MK1, FAST2, A and B inducers with the respective predictions of the simplified closed form solution. The head coefficients based on the static and total pressure, with and without losses, are reported, together with the “ideal” pumping performance for perfectly guided flow in the absence of pressure losses and deviation effects. For all of these inducers, the static head rise predicted by the model closely agrees with the experimental results.

Fluid Dynamics Associated to Launcher Developers

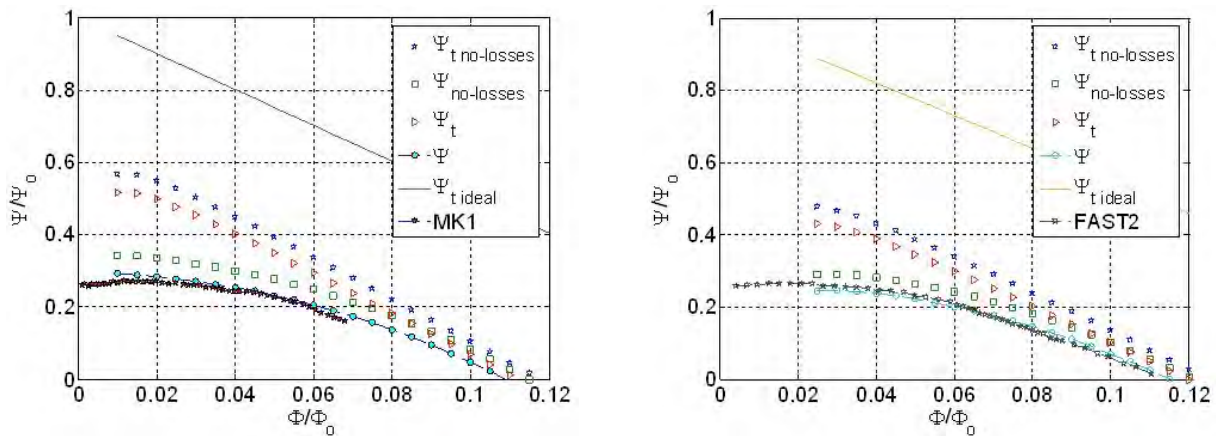


Figure 19. Comparison between the experimental non-cavitating performance of the MK1 inducer (left, red stars) and of the FAST2 inducer (right, white stars) with the predictions of the analytical model.

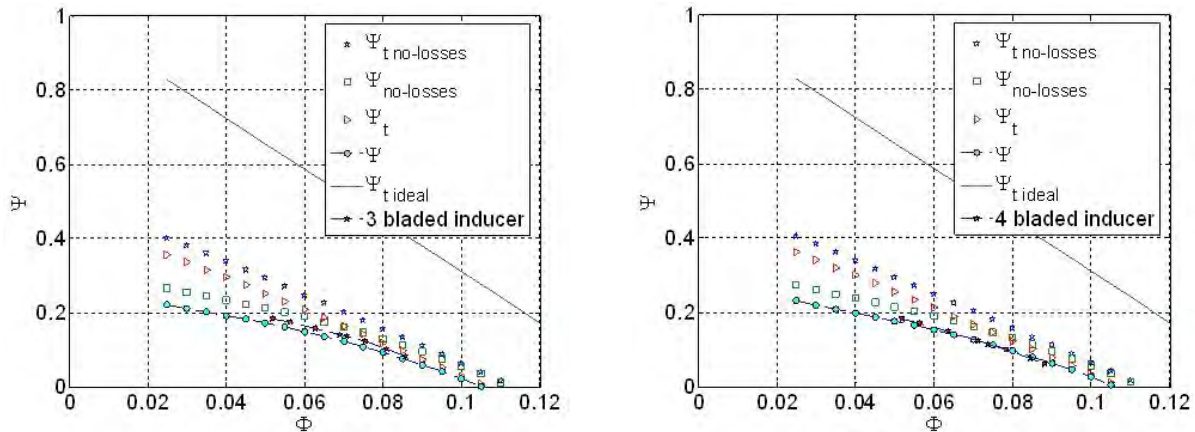


Figure 20. Comparison between the experimental noncavitating performance of the inducer A (left, red stars) and B (right, red stars) with the predictions of the analytical model.

For better assessment of these results, it is worth noting that the pressure tap used for the measurement of the static head rise developed by the MK1, FAST2, A and B inducers was located more than two diameters downstream of the blade trailing edge. At this location the flow more closely approximates the fully-settled axisymmetric conditions necessary for correct comparison of the experimental data with the model predictions.

Conversely, Figure 21 shows that the non-cavitating performance of inducers C and D is evaluated with lower accuracy. Most likely, this situation is related to the different position of the downstream pressure tap, which in this case was located very close to the blade trailing edge. This is clearly inconsistent with the nature of the proposed model, whose predictions are specifically derived from consideration of the axisymmetric far-field flow downstream of the inducer. The consequent deviation of the tangential velocity profile from the radial equilibrium one introduces a systematic error in the evaluation of the centrifugal effects and, therefore, of the static pressure downstream of the inducer. This is confirmed by the almost linear nature of the measured pumping characteristics of inducers C and D, which is consistent with the expected behavior for nearly uniform distribution of the axial flow velocity at the inducer trailing edge before the establishment of radial equilibrium conditions.

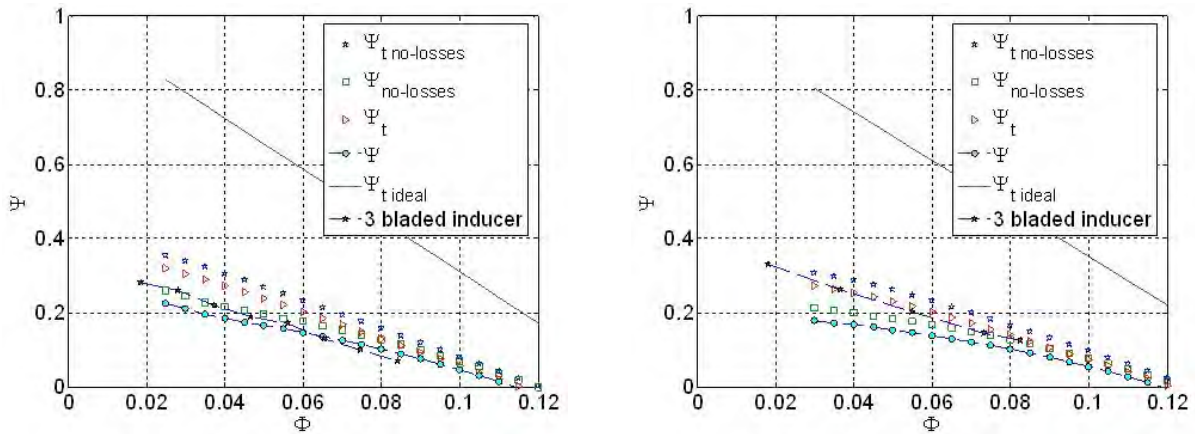


Figure 21. Comparison between the experimental noncavitating performance of the inducer C (left, red stars) and D (right, red stars) with the predictions of the analytical model.

The proposed model can also be applied for predicting the performance of helical inducers of more general hub and blade shapes. However, it is obviously expected to deliver best results when used for geometries more closely consistent with the assumptions used for its derivation, as confirmed by the results for the MK1 and FAST2 inducers.

More recently d'Agostino et al. 2011, [22], successfully extended a similar approach to the preliminary design and noncavitating performance prediction of radial turbopumps for space applications. An example of the geometry of a six-bladed impeller generated by means of their model is shown in Figure 22.

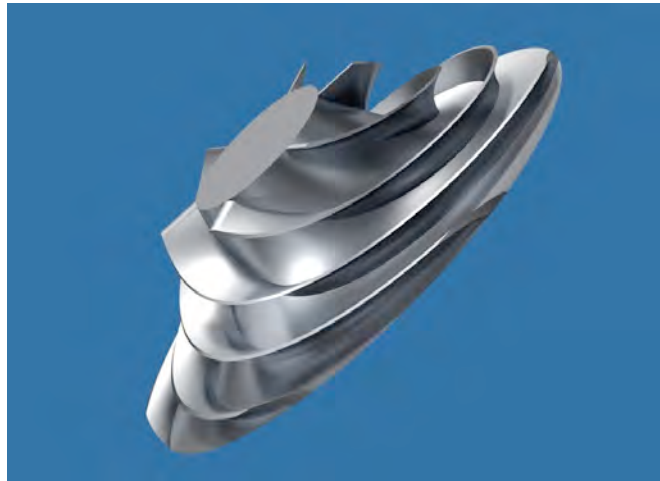
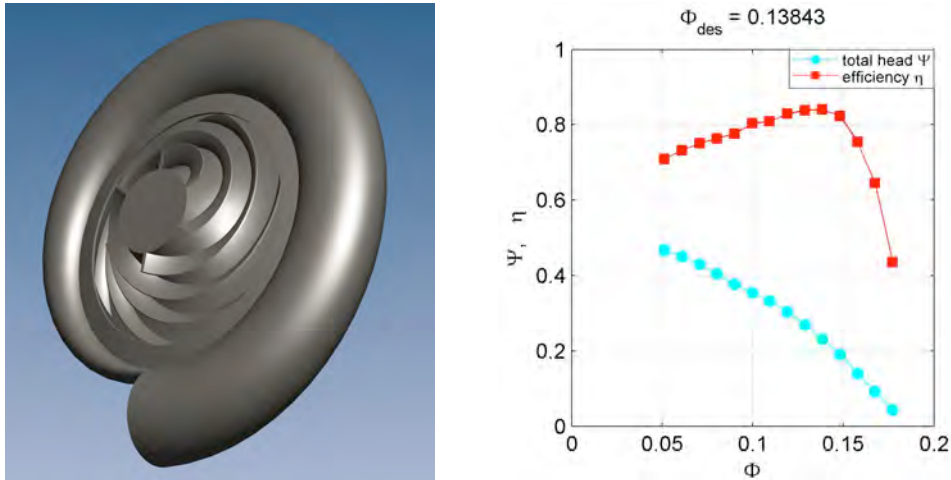


Figure 22. Rendering of a six-bladed radial impeller designed according to the model proposed in [22] d'Agostino et al. 2011.

In a later publication [23] d'Agostino et al. 2012 incorporated in their model the calculation of boundary layers inside the blade channels and other major forms of flow losses occurring in radial turbopumps, and demonstrated the possibility of using it for rapid parametric optimization of the machine geometry and performance under appropriate design constraints, such as target values of the specific speed, flow coefficient and impeller blading solidity. An example of application of this procedure to the optimal design

## Fluid Dynamics Associated to Launcher Developers

of a centrifugal pump is illustrated in .



**Figure 23. Left: 3D rendering of a turbopump operating with an six-bladed radial impeller, designed and optimized according to the model proposed in [22] d'Agostino et al. 2011. Right: predicted total head and total-to-total efficiency characteristics.**

## 2.1 Conclusions

Based on the available evidence, the present theoretical model proved to represent a useful tool for preliminary design and performance analyses of turbopump inducers. More specifically, the model is able to provide accurate quantitative indications for geometry definition, 3D flow field description, characterization and control of the blade loading, and prediction of the noncavitating pumping characteristics of helical inducers with tapered hub and variable blade pitch angle.

In this context, the model can be effectively used in two ways:

- for the preliminary definition of the geometry of tapered inducers, with particular reference to the hub and blade shape in order to minimize secondary flow losses and attain adequate cavitation performance;
- for the preliminary evaluation of the noncavitating performance of an inducer of given shape, or for defining the main geometric characteristics of an inducer, starting from the desired noncavitating pumping characteristic.

More generally, the model provides inducer designers with a comprehensive interpretative framework where the main – often conflicting – aspects of inducer design and their mutual implications can be assessed, quantified and balanced in view of the attainment of the desired requirements and performance.

The limitations of the model are mostly related to the simplifying assumptions and approximations introduced in order to attain a practical solution. In particular, improvements in the description of the flow, control of the blade load, and accuracy of the inducer performance prediction are expected to be gained by a more refined treatment of viscous effects, capable to account for the axisymmetric nature of the blade boundary layers and the radial changes of their thickness across the inducer annulus.

### 3.0 CAVITATION INSTABILITIES IN A 4-BLADED HIGH-HEAD INDUCER

#### 3.1 Introduction

In the axial inducers used for liquid propellant rocket turbopumps, typically working under cavitating conditions, it is usual to observe the development of flow instabilities, which can seriously degrade the performance of the machine, or even cause its complete failure ([8] Brennen 1994, [84] Tsujimoto et al. 1993). Because of the complexity of the phenomena involved and their development over wide ranges of time and spatial scales, experimentation still plays a central role in applied research on the unsteady hydrodynamics of cavitating turbopumps. The first step for understanding cavitation instabilities in inducers is therefore typically represented by experimentation on scaled models under Euler, Reynolds and thermal cavitation similarity conditions. The very high operational Reynolds numbers of rocket engine turbopump inducers (typically ranging from  $10^7$  and  $10^8$ ) usually allows a convenient reduction of the flow velocity in the experiments without significant Reynolds scaling effects.

The cavitating behavior of a rotating machine can be related, at least to some extent, to that of a static cascade of hydrofoils. The onset of cavitation instabilities in 2-D hydrofoils is strongly related to the mean cavity length, which displays a strong dependence on the parameter  $\sigma/\alpha$  (cavitation number divided by the incidence angle, [50] Kjeldsen et al. 1998, [37] Higashi 2001). One of the most studied forms of instabilities in hydrofoils is the so-called cloud cavitation instability, which consists in violent periodical fluctuations of the cavity length, typically occurring at constant Strouhal numbers and followed by the release of a cavity cloud at the conclusion of each cycle ([51] Kubota et al. 2009). The nature of this form of instability in cavitating hydrofoils has been studied in detail ([87] Tsujimoto et al. 1998), proving the correlation between cloud cavitation and the formation of a re-entrant jet at the cavity closure as a result of a critical adverse pressure gradient observed for cavity lengths greater than about 50% of chord ([12] Callenaere et al. 1998, [48] Kawanami et al. 1997, [70] Sakoda et al. 2001).

Another driving parameter in the development of cavitation induced flow instabilities in 2-D cascades is the dimension of the cavity with respect to the thickness of the blade passage. In rotating cascades, the blockage induced by cavitation can lead to rotating instabilities similar to rotating stall in compressors, such as rotating cavitation ([35] Hashimoto et al. 1997b, [100] Zoladz 2000, [68] Ryan et al. 1994, [32] Goirand et al. 1992) and rotating choke ([85] Tsujimoto and Semenov 2002, [91] Uchiumi and Kamijo 2008). In particular, it has been found that the onset point of rotating cavitation corresponds to a cavity length equal to about 70% of blade spacing and, furthermore, that 4-bladed inducers are expected to show higher rotating cavitation frequency than 3-bladed inducers ([88] Tsujimoto 2001).

Finally, the presence of the blade tip and the consequent clearance between the impeller and the casing introduces further complexities in the development of cavitation and cavitation induced instabilities. The so-called backflow vortex cavitation, a rotating instability with multiple vortical cells forming in the inducer backflow, was detected for the first time in 1997 for two separated ranges of values of the cavitation number: at high cavitation numbers (3-4 times the breakdown cavitation number), when the tip vortex cavitation is the principal form of cavitation, and around the head breakdown for lower flow coefficients, where the backflow is particularly strong ([86] Tsujimoto et al. 1997). It has been recently shown that the extent of the cavitation backflow and, consequently, of the surge instability associated to it, can be significantly reduced by adding a “backflow restriction step” to the inducer casing ([80] Tomaru et al. 2007).

It is well known that the noncavitating performance of inducers is relatively insensitive to the tip clearance for clearance/mean blade height ratios lower than 2%, but tends to rapidly degrade for larger values of this parameter. In addition, tip clearance affects the cavitation inception number in unshrouded machines since cavitation usually begins in the vortices associated to the tip clearance flows ([1] Acosta 1958, [43] Janigro

## Fluid Dynamics Associated to Launcher Developers

A. and Ferrini 1973). Finally, azimuthal instabilities like rotating cavitation are significantly influenced by the tip clearance, due to their strict correlation with the extent and characteristics of the tip vortices. The techniques proposed so far for suppressing rotating cavitation include: use of special custom-designed devices ([78] Subbaraman and Patton M. 2006), modifications of the inlet housing ([46] Kamjio et al. 1993), introduction of an axial groove along the inducer casing ([41] Imamura et al. 2003), cutbacks of the leading edges of alternate blades ([39] Horiguchi et al. 2000, [95] Yoshida et al. 2001), design modifications of both inducer and inlet geometry ([76] Shimura et al. 2003).

The present paper illustrates the main results of a series of inducer flow experiments conducted in the Cavitating Pump Rotordynamic Test Facility (CPRTF) at Alta. The tests have been carried out on the four-bladed high-head inducer designated as DAPAMITO4, designed and manufactured using the reduced-order analytical model for the prediction of geometry and noncavitating performance of typical space rocket inducers described earlier ([20] d'Agostino et al. 2008a, [21] d'Agostino et al. 2008b). The experiments have been performed at different water temperatures and flow coefficients, under cavitating and noncavitating conditions, and the development of both azimuthal and streamwise instabilities has been observed. The results of a similar test campaign conducted on a 3-bladed inducer, including in particular a detailed study of the influence of the blade tip clearance on the pump performance and the flow instabilities, have been presented in a previous paper ([81] Torre et al. 2010).

### 3.2 Experimental Apparatus

#### 3.2.1 Test Facility and Instrumentation

The Cavitating Pump Rotordynamic Test Facility (CPRTF, Figure 24) is a versatile and easily instrumentable facility operating in water ([65] Rapposelli et al. 2002), at temperatures up to 90 °C. The facility is intended as a flexible apparatus that can readily be adapted to conduct experimental investigations on virtually any kind of fluid dynamic phenomena relevant to high performance turbopumps in a wide variety of alternative configurations (impeller with axial, radial or mixed flow, with or without an inducer). The CPRTF has been especially designed for the analysis of unsteady flow phenomena and rotordynamic impeller forces in scaled cavitation tests under fluid dynamic and thermal cavitation similarity conditions. It can also be configured as a small water tunnel to be used for thermal cavitation tests aimed at fundamental investigations and/or experimental validation of numerical tools and simulations.

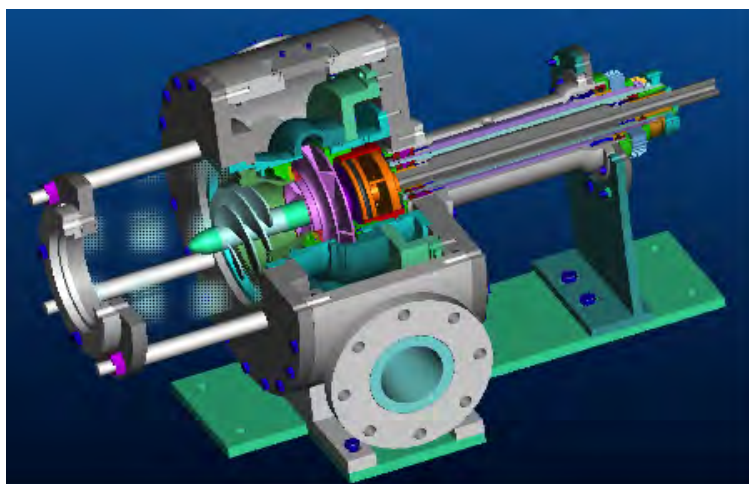
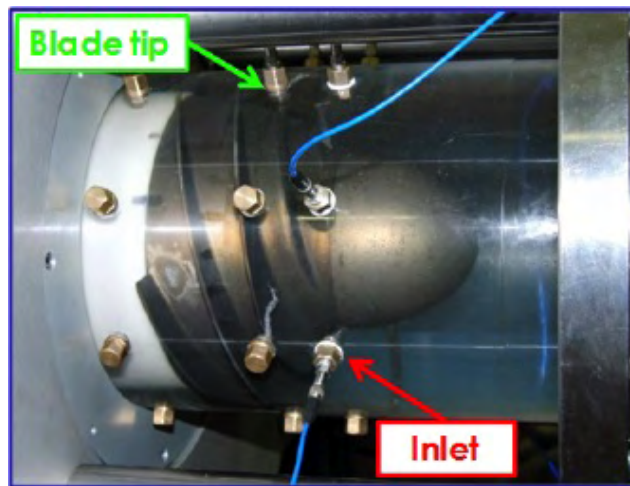


Figure 24. Cut-off drawing of the Cavitating Pump Rotordynamic Test Facility (CPRTF) test section.



The test section (Figure 24) can be equipped with a rotating dynamometer, for the measurement of the instantaneous forces and moments acting on the impeller, and with an eccentric drive mechanism capable of adjusting and rotating the eccentricity of the impeller axis in the range from 0 to 2 mm and  $\pm 3000$  rpm, specifically designed for rotordynamic experiments. The inlet section, made in transparent Plexiglas, allows for multilateral optical access to the inducer flow. It can be instrumented with several flush-mounted piezoelectric pressure transducers (PCB M112A22, ICP<sup>®</sup> voltage mode-type, 0.1% class), located at different axial stations (Figure 25, in particular, shows the transducers installed at the inducer inlet and the blade tip). At each station, up to eight transducers can be mounted with a given angular spacing, in order to cross-correlate their signals for amplitude, phase and coherence analyses. As a result, waterfall plots of the power spectral density of the pressure fluctuations can be obtained as functions of the cavitation number, in order to identify the presence of instabilities in the flow conditions under consideration. Cross-correlation of two pressure signals from different locations allows for determining the streamwise or azimuthal nature of a given instability and, in the second case, the number of rotating cells involved (up to one half of the total number of pressure transducers located on the same axial cross-section of the inducer casing).



**Figure 25. The transparent inlet section of the facility instrumented with piezoelectric pressure transducers.**

The water pressure at the inlet of the test section can be adjusted by means of an air bag in the water tank, while the temperature regulation is obtained by means of a 5 kW electrical heater. A Silent Throttle Valve is used for the variation of the pump load. Two electromagnetic flow meters (mod. 8732C by Fisher-Rosemount, range 0-100 l/s, accuracy 0.5% FS), mounted on the suction and discharge lines of the water loop, provide the measurement of the inlet and outlet flow rates. The inlet pressure is monitored by an absolute transducer positioned about one diameter upstream of the blade leading edges (Druck, model PMP 1400, 0÷1.5 bar operating range, 0.25% precision class), while a pair of redundant differential pressure transducers measure the pump pressure rise between the same inlet section and an outlet section positioned about two diameters downstream of the blade trailing edges (Kulite, model BMD 1P 1500 100, 0÷6.8 bar-d operating range, 0.1% precision class; Druck, model PMP 4170, 0÷1 bar-d operating range, 0.08% precision class). Photo cameras and high-speed video cameras can be used for visualization of the cavitating flow on the test article.

### 3.2.2 Test Inducer

The experiments have been conducted on a four-bladed, tapered-hub, variable-pitch, high-head inducer, named DAPAMITO4, whose main geometrical and operational parameters are summarized in Table 3. It is

## Fluid Dynamics Associated to Launcher Developers

made of 7075-T6 aluminum alloy and has been designed using the reduced order model described earlier ([20] d'Agostino et al. 2008a and [21] d'Agostino et al. 2008b).

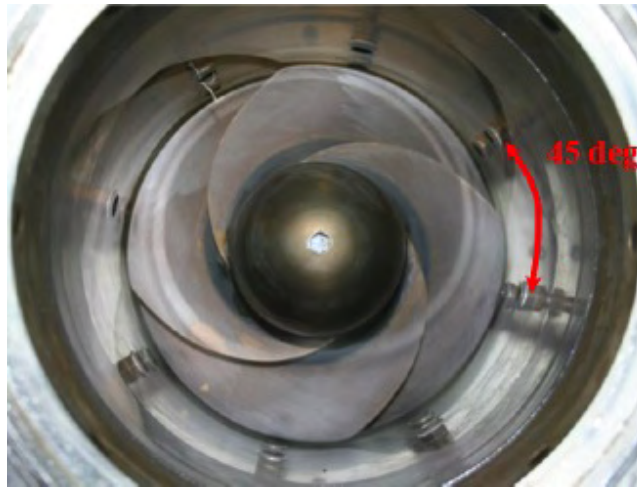
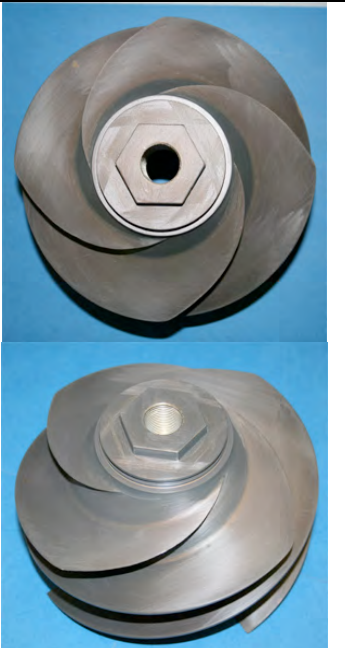


Figure 26. Axial front view of the DAPAMITO4 inducer inside the test chamber of the facility.

The overall dimensions of this inducer have been chosen for installation and testing in the current CPRTF configuration. A moderate value of the blade loading (with a diffusion factor  $D = 0.38$  as defined in in [20] d'Agostino et al. 2008a, [21] d'Agostino et al. 2008b) and a high solidity ( $\sigma_T = 2.25$ ) have been chosen for reducing the leading-edge cavity and improving the suction performance. The value of the tip incidence-to-blade angle ratio  $\alpha/\beta_b < 0.5$  has been selected with the aim of controlling the danger of surge instabilities at design flow under cavitating conditions. Figure 26, in particular, shows a front view of the inducer mounted in the test chamber of the facility, with the piezoelectric pressure transducers flush-mounted at a number of azimuthal locations.

Table 3. Geometrical and operational parameters of the DAPAMITO4 inducer.

Design flow coefficient	[--]	$\Phi_D$	0.070	
Number of blades	[--]	$N$	4	
Tip radius	mm	$r_T$	81.0	
Inlet tip blade angle	deg	$\gamma_{Tle}$	81.10	
Inlet hub radius (fully-developed blade)	mm	$r_{Hle}$	48.0	
Outlet hub radius	mm	$r_{Hte}$	58.5	
Mean blade height	mm	$h_m$	27.75	
Axial length (fully-developed blade)	mm	$c_a$	63.5	
Inlet hub radius	mm	$r_{HI}$	35.0	
Axial length	mm	$L$	90.0	
Diffusion factor	[--]	$D$	0.38	
Ratio between tip incidence and blade angles	[--]	$\alpha/\beta_b$	0.31	
Tip solidity	[--]	$\sigma_T$	2.25	
Incidence tip angle @ design	deg	$\alpha$	2.74	
Outlet tip blade angle	deg	$\gamma_{Tte}$	72.46	

### 3.3 Results and Discussion

#### 3.3.1 Noncavitating Performance and Hydraulic Efficiency

A first set of tests have been performed on the DAPAMITO4 inducer for the characterization of its noncavitating performance and hydraulic efficiency at two different water temperatures:  $T = 18.8\text{ }^{\circ}\text{C}$  and  $49.6\text{ }^{\circ}\text{C}$ . The blade tip clearance for these tests was 2 mm, corresponding to 6.8% of the mean blade height. Figure 27 shows the noncavitating experimental curves in terms of the static head coefficient  $\Psi = \Delta p / \rho \Omega^2 r_T^2$  and the hydraulic efficiency  $\eta = Q \Delta p_i / \tau \Omega$  as functions of the flow coefficient  $\Phi = Q / \pi \Omega r_T^3$ .

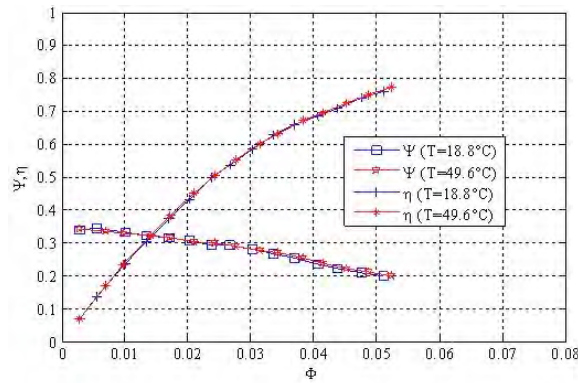


Figure 27. DAPAMITO4 inducer noncavitating performance and hydraulic efficiency at two different water temperatures.

In this case, the low pressure tap for the measurement of the static pressure rise has been located on the suction line, about 6 inducer diameters upstream of the blade leading edges, in order to eliminate the effect of inlet flow prerotation. The high pressure tap has been mounted on the discharge line at about 2.5 duct diameters downstream of the test chamber connection, because of the uncertainties in the influence of the exit flow swirl. Hence head measurements include the losses due to the flow diffusion from the inducer outlet into the test section and to the entrance in the discharge line. In order to evaluate the total pressure rise, some assumptions have been made both on the measured static pressure rise and the dynamic pressure at the exit of the inducer.

The torque  $\tau$  has been directly measured by means of the rotating dynamometer, thereby by-passing the uncertainties associated with bearing and seal friction on the inducer shaft. The curves, obtained at a rotational speed of 1750 rpm and several temperatures of the liquid, confirm the independence of the test results on the flow temperature. The highest measured efficiency corresponding to the highest experimental flow coefficient ( $\Phi = 0.052$ ) is about 77%, in accordance with the typical values for this kind of machines (70÷80%).

#### 3.3.2 Cavitating Performance

The cavitating performance of the inducer has been characterized in terms of the head coefficient as a function of the cavitation number  $\sigma = (p_{in} - p_v) / \frac{1}{2} \rho \Omega^2 r_T^2$ , at ambient temperature and rotating speed  $\Omega = 3000\text{ rpm}$ , for several values of the flow coefficient (84%, 80%, 76%, 71% and 63% of  $\Phi_D$ ). In the

## Fluid Dynamics Associated to Launcher Developers

present case, the static pressure at inducer inlet has been used for the evaluation of the cavitation number.

Figure 28 (left) shows a comparison between the results obtained using two different test procedures, here indicated as “steady” and “continuous” experiments, and refers to a value of  $c_{\%}$  (tip blade clearance-to-mean blade height ratio) equal to 2.7%. More in detail, the “steady” test results have been obtained by averaging the measurements over 2.4 s at fixed values of the flow coefficient and cavitation number, while the “continuous” test data have been taken keeping the flow coefficient and the pump rotational speed constant and gradually reducing the inlet pressure from atmospheric conditions to the minimum allowable value at a constant rate of about 3 mbar/s. Figure 28 (right) illustrates the appearance of cavitation on the inducer at a flow coefficient equal to 76% of the design value and decreasing values of the cavitation number. The performance curves show a “one step” shape under breakdown conditions, consisting of an intermediate head drop. As shown later, this phenomenon is associated to the occurrence of some forms of instabilities as the synchronous rotating cavitation.

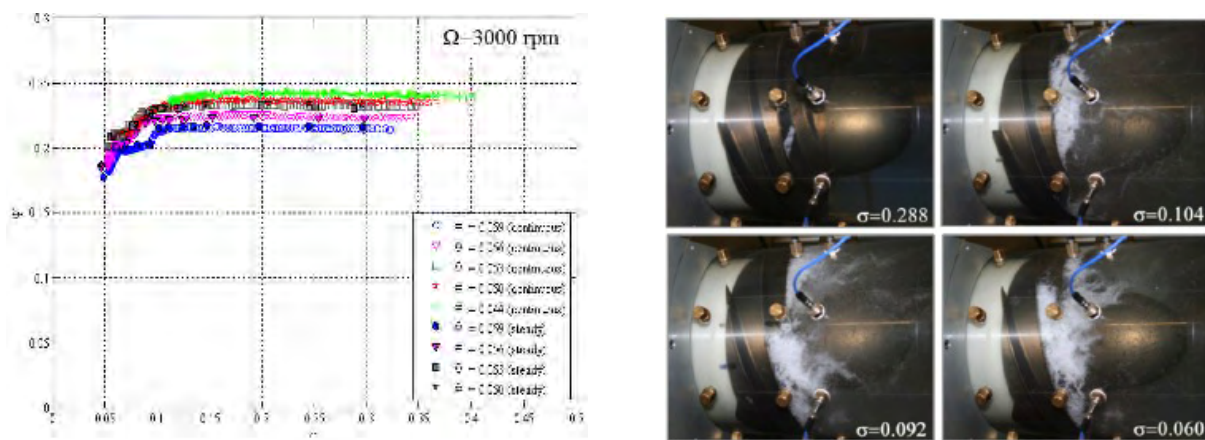


**Figure 28. Cavitating performance of the DAPAMITO4 inducer at different flow coefficients (left) and appearance of cavitation in the inducer at different cavitation numbers, for  $\Phi = 0.053$  (right). Data taken at ambient temperature  $T = 15$  °C.**

### 3.3.3 Cavitating Performance

The instability analysis has been conducted for the same flow coefficients investigated during the cavitating performance characterization. The analysis is based on three steps: a) detection and recognition of oscillating phenomena by the analysis of the pressure fluctuations in the inducer, b) definition of the most probable nature of the phenomena (axial or rotating and, in the second case, number of lobes and direction of rotation) by the analysis of the cross-spectra phases ( $\varphi$ ) for different transducers couples located at the same axial cross-section of the inducer inlet (cross-spectra phases constantly close to 0 imply an axial phenomenon, cross-spectra phases close to  $n\Delta\theta$ , with  $n$  integer, imply a rotating phenomenon with  $n$  lobes), c) validation of previous points by the analysis of the coherence function  $\gamma_{xy}$  (only phenomena with  $\gamma_{xy} > 0.8$  have been considered).

The tests illustrated in the present Section are referred to ambient temperature conditions ( $T = 15$  °C). Figure 29 shows the waterfall plots obtained at  $\Phi = 0.044$  and  $\Phi = 0.056$ , with  $\Omega = 3000$  rpm; the inducer rotational frequency (50 Hz) and its harmonics ( $n\Omega$ ) have been filtered. The orange boxes refer to the actual driving instabilities, the yellow ones to the non-linear interactions between the actual phenomena and the harmonics of the blade passage ( $n\Omega$ ). Table 4 summarizes the flow instabilities detected on the DAPAMITO4 inducer at 0.8 mm clearance in terms of frequencies range, flow coefficients at which they

have been observed, cavitation number range, typology of instability (rotating or axial) and number of lobes.

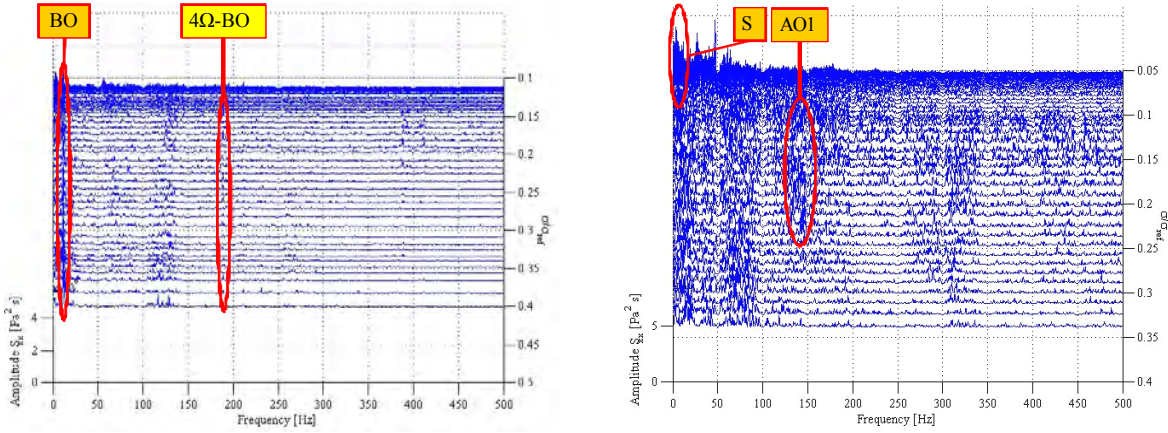


Figure 29. Waterfall plot of the power spectrum of the inlet pressure fluctuations on DAPAMITO4 inducer at  $\phi = 0.044$  (left) and  $\phi = 0.056$  (right) with  $c\% = 2.7\%$ ,  $\Omega = 3000$  rpm,  $T = 15.0$  °C, filtered for the  $n\Omega$  frequencies.

Table 4. Flow instabilities detected on the DAPAMITO4 inducer ( $c\% = 2.7\%$ ,  $\Omega = 3000$  rpm,  $T = 15.0$  °C).

Instability I.D.	Frequency [Hz]	$\phi$	$\sigma$ range	Type
S	1÷8.3	0.059	0.054÷0.079	Axial
		0.056	0.053÷0.093	
		0.053	0.058÷0.124	
		0.050	0.068÷0.122	
		0.044	0.113÷0.130	
BO	10.3÷11.7	0.044	0.113÷0.370	Rotating 1-lobe
AO1	127.4÷146.5	0.059	0.227÷0.293	Axial
		0.056	0.070÷0.247	
		0.053	0.107÷0.249	
		0.050	0.101÷0.171	
		0.044	0.118÷0.141	
4Q - BO	188.5÷189	0.044	0.114÷0.130	Rotating 3-lobes

Examination of the pressure fluctuations shows the occurrence of four different phenomena:

- The frequency denoted as S (Surge) is related to a 0-th order (axial) instability, as it can be inferred from cross-correlation analyses like the one presented in Figure 30. It appears at all the flow coefficients

Fluid Dynamics Associated to Launcher Developers

investigated in this experimental campaign.

- The frequency denoted as BO (Backflow Oscillation) appears only at the lowest flow coefficient. It is a single-cell, co-rotating instability (as shown in Figure 31) related to the backflow rotating speed ( $\sim 0.2\Omega$ ), with similar characteristics to those illustrated in [89] by Tsujimoto et al. 2005.
- The frequency denoted as AO1 (Axial Oscillation 1) is an axial instability which has been observed at all the flow coefficients. This phenomenon appears at high and intermediate cavitation numbers.
- Finally, the  $4\Omega - BO$  frequency refers to a three-cells co-rotating instability (likely due to a non-linear interaction between the blade passage frequency  $4\Omega$  and the backflow oscillation  $BO$ ).

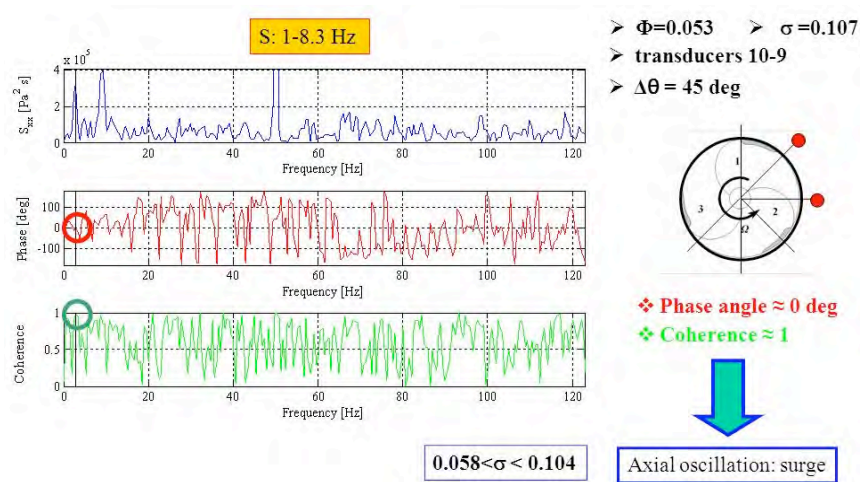


Figure 30. Amplitude and phase of the cross-spectral density and coherence function of the pressure signals of two transducers with  $45^\circ$  angular separation mounted at the inlet section of the DAPAMITO4 inducer (phenomenon = S,  $\Omega = 3000 \text{ rpm}$ ,  $T = 15.0 \text{ }^\circ\text{C}$ ).

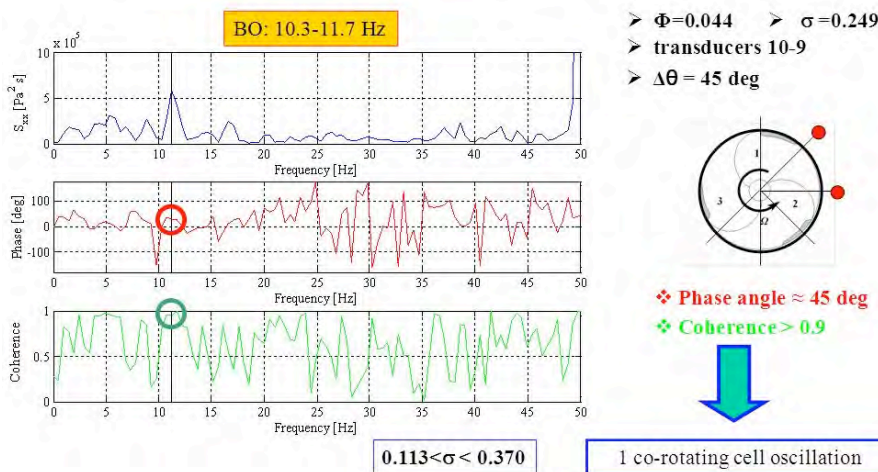
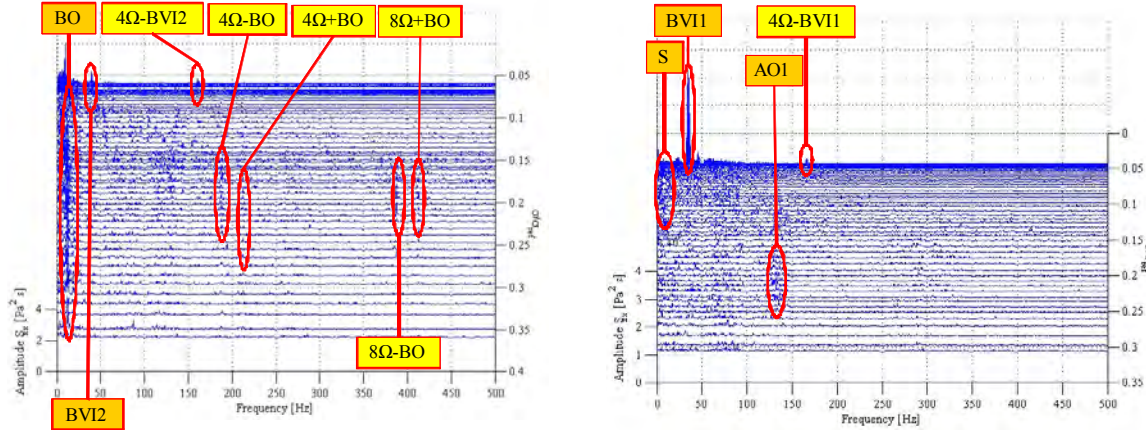


Figure 31. Amplitude and phase of the cross-spectral density and coherence function of the pressure signals of two transducers with  $45^\circ$  angular separation mounted at the inlet section of the DAPAMITO4 inducer (phenomenon = BO,  $\Omega = 3000 \text{ rpm}$ ,  $T = 15.0 \text{ }^\circ\text{C}$ ).

### 3.3.4 Flow Instabilities at Higher Temperatures

Figure 32 shows the waterfall plots obtained at  $\Phi = 0.044$  and  $\Phi = 0.059$  and a temperature of about  $50\text{ }^\circ\text{C}$ , with  $\Omega = 3000\text{ rpm}$ ; also in this case, the inducer rotational frequency ( $50\text{ Hz}$ ) and its harmonics ( $n\Omega$ ) have been filtered. The orange boxes refer to the actual driving instabilities, whereas the yellow ones are referred to the non-linear interactions between the actual phenomena and the harmonics of the blade passage ( $n\Omega$ ).



**Figure 32. Waterfall plot of the power spectrum of the inlet pressure fluctuations on DAPAMITO4 inducer at  $\Phi = 0.044$  (left) and  $\Phi = 0.059$  (right) with  $c\% = 2.7\%$ ,  $\Omega = 3000\text{ rpm}$ ,  $T = 49.7\text{ }^\circ\text{C}$ , filtered for the  $n\Omega$  frequencies.**

Table 5 summarizes the flow instabilities detected in this case in terms of frequencies range, flow coefficients at which they have been observed, cavitation number range, typology of instability (rotating or axial) and number of lobes. Examination of the pressure fluctuations shows the occurrence of several different phenomena:

- The frequency denoted as *S* (*Surge*) is related to a 0-th order (axial) instability. It appears at all the investigated flow coefficients beginning at intermediate cavitation numbers, and has the same characteristics of the surge instability observed in the cold tests.
- The frequency denoted as *BO* (*Backflow Oscillation*), as in the case of the cold tests, appears only at the lowest flow coefficient; it is a single-cell co-rotating instability related to the backflow rotating speed ( $\sim 0.2\Omega$ ).
- The frequency denoted as *BVI1* (*Backflow Vortices Instability 1*) appears to be related to a 3-lobes rotating phenomenon, typical of the backflow vortices instabilities. The phenomenon occurs at high and intermediate flow coefficients and is observed only at very low cavitation numbers (close to the head breakdown). The rotational frequency of the three lobes as a whole can be obtained by dividing the detected instability frequency by the number of lobes:  $BVI1/3 \approx 10\text{ Hz}$ , which corresponds to the backflow rotating speed ( $\sim 0.2\Omega$ ).
- The frequency denoted as *BVI2* (*Backflow Vortices Instability 2*) appears to be related to a 2-lobes rotating phenomenon: even if the rotational frequency of the vortices system ( $BVI2/2 \approx 20\text{ Hz}$ , about  $0.4\Omega$ ) is higher than the typical one, this phenomenon has been associated to a backflow vortices instability.
- The frequency denoted as *AO1* (*Axial Oscillation 1*) appears at all the flow coefficient except  $\Phi = 0.044$ : it is an axial oscillation and has the same characteristics of the similar one detected at ambient temperature.

Fluid Dynamics Associated to Launcher Developers

- The other detected frequencies are likely to be caused by non-linear interactions between the phenomena  $BO$ ,  $BVII$  and  $BVI2$  and the harmonics of the blade passage. The frequencies of these phenomena are  $4\Omega - BVI2$ ,  $4\Omega - BVII$ ,  $4\Omega - BO$ ,  $4\Omega + BO$ ,  $8\Omega - BO$  and  $8\Omega + BO$ ; the corresponding cross-correlation phases can be obtained by  $\varphi(4\Omega - BVI2) = \varphi(4\Omega) - \varphi(BVI2)$ ,  $\varphi(4\Omega - BVII) = \varphi(4\Omega) - \varphi(BVII)$ ,  $\varphi(4\Omega - BO) = \varphi(4\Omega) - \varphi(BO)$ ,  $\varphi(4\Omega + BO) = \varphi(4\Omega) + \varphi(BO)$ ,  $\varphi(8\Omega - BO) = \varphi(8\Omega) - \varphi(BO)$ ,  $\varphi(8\Omega + BO) = \varphi(8\Omega) + \varphi(BO)$ .

Table 5. Flow instabilities detected on the DAPAMITO4 inducer ( $c\% = 2.7\%$ ,  $\Omega = 3000$  rpm,  $T = 50.0$  °C).

Instability I.D.	Frequency [Hz]	$\Phi$	$\sigma$ range	Type
S	1.5÷7.8	0.059	0.043÷0.121	Axial
		0.056	0.043÷0.187	
		0.053	0.046÷0.300	
		0.050	0.060÷0.184	
		0.044	0.059÷0.141	
BO	9.3÷12.7	0.044	0.060÷0.350	Rotating 1-lobe
BVI1	33.7÷36.6	0.059	0.043÷0.045	Rotating 3-lobes
		0.056	0.043÷0.047	
		0.053	0.045÷0.046	
BVI2	38.6÷42.5	0.050	0.067÷0.071	Rotating 2-lobes
		0.044	0.059÷0.076	
AO1	127.9÷138	0.059	0.121÷0.208	Axial
		0.056	0.094÷0.244	
		0.053	0.147÷0.265	
		0.050	0.170÷0.271	
$4\Omega - BVI2$	155.3÷161.6	0.050	0.060÷0.071	Rotating 2-lobes
		0.044	0.059÷0.072	
$4\Omega - BVI1$	166÷166.5	0.059	0.043÷0.044	Rotating 1-lobe
		0.056	0.043÷0.045	
		0.053	0.044÷0.045	
$4\Omega - BO$	187.5÷191.9	0.044	0.141÷0.239	Rotating 3-lobes
$4\Omega + BO$	212÷212.4	0.044	0.167÷0.266	Rotating 5-lobes
$8\Omega - BO$	387.7÷388.2	0.044	0.161÷0.203	Rotating 7-lobes
$8\Omega + BO$	406÷412	0.044	0.161÷0.203	Rotating 9-lobes



When water temperature is further increased, starting from a value of about 65 °C, a weak sub-synchronous rotating cavitation has been observed in addition to the previously described phenomena. This instability is a 1-lobe phenomenon rotating at a frequency between  $0.8\Omega$  and  $0.95\Omega$ , and occurs when the head coefficient begins to be affected by the cavitation (close to the breakdown conditions). The waterfall plot in Figure 33 on the left shows a typical case of flow conditions under which this rotating cavitation instability has been detected while the same figure on the right reports a magnification of the not-filtered waterfall plot highlighting how, at a certain cavitation number ( $\sigma \approx 0.100$ ), the Synchronous Rotating Cavitation (SRC) at 50 Hz transforms into the sub-synchronous rotating cavitation (RC).

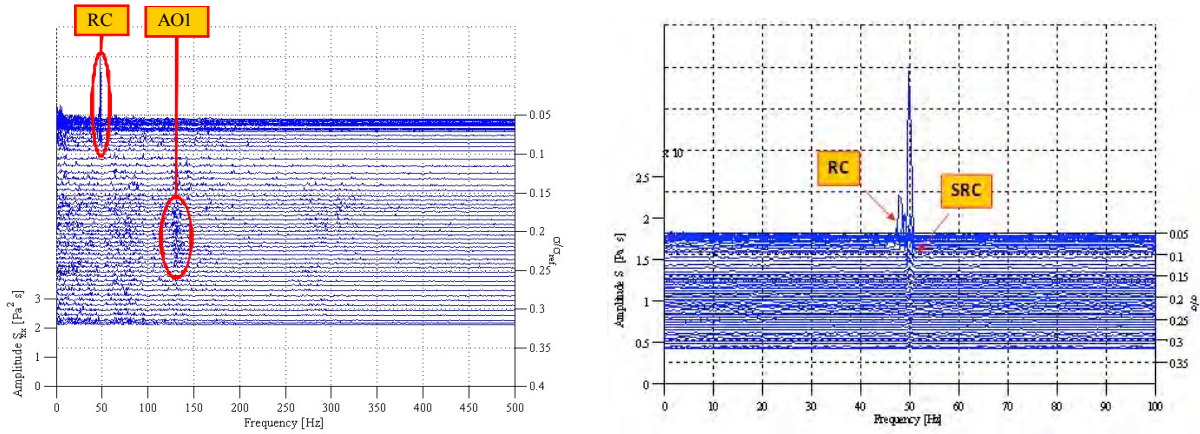


Figure 33. Left: waterfall plot of the power spectrum of the inlet pressure fluctuations on DAPAMITO4 inducer at  $\Phi = 0.059$  ( $C\% = 2.7\%$ ,  $\Omega = 3000$  rpm,  $T = 64.8$  °C), filtered for the  $n\Omega$  frequencies. Right: magnification of the waterfall plot in the 0 – 100 Hz range.

### 3.3.5 Characterization of Synchronous Instabilities

Figure 34 shows the waterfall plot of the power spectrum of the inlet pressure fluctuations on the DAPAMITO4 inducer at  $\Phi = 0.059$  and ambient temperature: the harmonics of the blade passage, in this case, have not been filtered in order to possibly characterize the synchronous flow instabilities occurring on the pump.

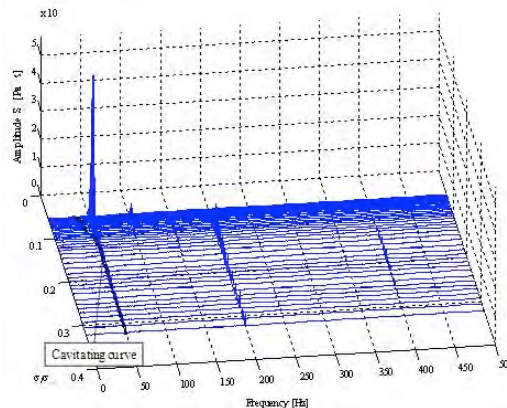
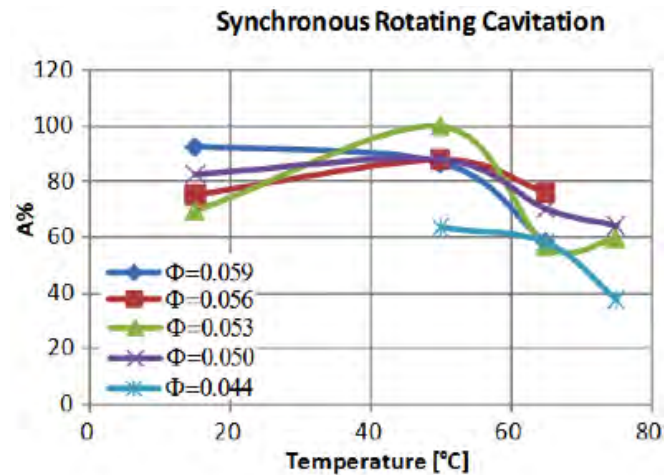


Figure 34. Non-filtered waterfall plot of the power spectrum of the inlet pressure fluctuations on DAPAMITO4 inducer at  $\Phi = 0.059$  ( $C\% = 2.7\%$ ,  $\Omega = 3000$  rpm,  $T = 15.4$  °C). The cavitating performance curve is represented as a black line on the  $\sigma$  - frequency plane.

## Fluid Dynamics Associated to Launcher Developers

It can be observed that the peaks at  $\Omega=50$  Hz become significantly more evident in correspondence of the first head drop (see the cavitating performance curve reported on the  $\sigma$  - *frequency* plane in the same plot). The cross-correlation analysis confirmed that this phenomenon is a one co-rotating cell oscillation which can be classified as a “Synchronous Rotating Cavitation” (or “Steady Asymmetric Cavitation”). It is worth noticing that the maximum amplitude of oscillations is reached when the cavitating performance curve just above breakdown conditions displays the “one step” shape, typical of this particular inducer.



**Figure 35. Amplitude (expressed as % of the maximum value, 15100 Pa) of the Synchronous Rotating Cavitation instability, as a function of the water temperature, at different flow coefficients ( $c_{\%} = 2.7\%$ ,  $\Omega = 3000$  rpm).**

The amplitude of Synchronous Rotating Cavitation oscillations, it is about one order of magnitude higher than the other non-synchronous instabilities. Analysis of the amplitude of oscillations at different water temperatures has shown that, as a general trend, it tends to decrease when temperature increases (see Figure 35). At the same time, looking at the cavitating performance curves, it has been clearly observed that the “one step” behavior becomes less and less evident when temperature increases. It can therefore be concluded that thermal cavitation effects have an influence on the flow instability itself (by reducing the amplitude of oscillations) as well as on the pump performance (by changing the shape of the performance curve and the extent of the “one step” behavior).

### 3.4 Conclusions

The following main considerations can be drawn from the results of the experimental campaign been conducted on the 4-bladed axial inducer, indicated DAPAMITO4 and designed by means of a reduced-order model recently developed at Alta:

- The maximum hydraulic efficiency of the inducer is close to 80%.
- The cavitating performance of the inducer is characterized by a “one step” shape next to breakdown conditions, associated to the occurrence of a synchronous rotating instability (steady asymmetric cavitation).
- Only weak instabilities have been observed at ambient temperature, including a 0-th order surge and a backflow oscillation (characterized by one lobe rotating at 0.2 times the pump rotational speed).
- At higher water temperatures, together with the surge and the backflow oscillation, two different kinds of backflow vortices instabilities have been observed. In addition, at water temperatures equal to 65 °C

or higher, a weak subsynchronous rotating cavitation phenomenon has been detected.

- The amplitude of the flow oscillations associated to the steady asymmetric cavitation generally tends to decrease when water temperature increases. Significant thermal cavitation effects can therefore be observed on both the flow instability extent and the cavitating performance of the inducer.

## **4.0 ROTORDYNAMIC FORCES ON A 4-BLADED HIGH-HEAD INDUCER**

### **4.1 Introduction**

Rotordynamic forces are universally recognized as an extremely dangerous source of vibrations in turbomachines and other rotating elements. These forces can affect all the components of the machine, including the bearings, the seals and the impeller itself ([25], Ehrich and Childs 1984).

The rotordynamic forces acting on centrifugal pumps have been widely studied in the past (see for example [36] Hergt and Krieger 1969, [62] Ohashi and Shoji 1984), even if only limited information is available on their dependence on cavitation ([44] Jery 1987, [27] Franz 1989). Recently, Yoshida et al., [96] have investigated the effects of seal geometry on the rotordynamic forces acting on a two-dimensional centrifugal impeller with logarithmic spiral blades, while Suzuki et al. [79] have measured the rotordynamic forces on an artificial heart pump impeller. Experimental data on the influence of cavitation on radial and rotordynamic forces on turbopump impellers mainly come from the work carried out at the California Institute of Technology in the context of the doctoral theses of Jery 1987, [44], Franz 1989, [27], and Bhattacharyya 1994, [1], and 1997, [4]. More recently, at JAXA Kakuda Space Center in Japan, some work has been carried out on whirling axial inducers under cavitating conditions ([98] Yoshida et al. 2010), showing the existence of a strong coupling between a synchronous rotating cavitation observed in the pump and the rotor vibration system. However, presently several aspects related to the rotordynamic forces acting on axial inducers and their correlation with cavitation are not yet perfectly understood.

The rotordynamic configuration of the Cavitating Pump Test Facility (CPTF) at Alta ([65] Rapposelli et al. 2002) has been designed for the analysis of steady and unsteady fluid forces and moments acting on the impeller as a consequence of its whirl motion under cavitating or fully-wetted flow conditions, with special emphasis on the onset and development of lateral rotordynamic instabilities. Recently, in the framework of a project funded by the European Space Agency, an experimental campaign has been carried out at Alta on two axial inducers (a three bladed and a four bladed one), aimed at investigating the influence of cavitation on rotordynamic forces by means of forced vibration experiments where the impeller is subject to a whirl motion of given constant eccentricity and angular velocity ([82] Torre et al. 2010, [64] Pasini et al. 2010); some experiments were also carried out by means of a novel testing procedure able to attain the continuous spectrum of the rotordynamic force as a function of the whirl/rotating speed ratio ([83] Torre et al. 2011). In the present paper, the role of the structure and oscillating behavior of the cavitating region on the blades will be analyzed more in detail, by comparing the force measurements on the four-bladed inducer to high-speed movies taken under forced whirl conditions.

### **4.2 Test Apparatus**

Alta's Cavitating Pump Rotordynamic Test Facility (CPRTF, Figure 36) has been specifically designed for characterizing the performance of cavitating/non-cavitating turbopumps in a wide variety of alternative configurations (axial, radial or mixed flow, with or without an inducer; [65] Rapposelli et al. 2002). The facility operates in water at temperatures up to 90 °C and is readily adaptable to conduct experimental investigations on virtually any kind of fluid dynamic phenomena relevant to high performance turbopumps. The inlet section is made in transparent Plexiglas and allows for the optical visualization of the cavitation on the test inducer. It can easily be replaced in order to match the tip diameter and clearance of different axial inducers.

The facility is instrumented with a series of transducers for measuring pressures (inducer inlet pressure and static pressure rise, pressure fluctuations in several points close to inducer inlet), flow rates (on the suction and discharge lines), fluid temperatures (inside the main tank and at inducer inlet), absolute angular positions

and velocities (driving and eccentric shaft).



**Figure 36. The Cavitating Pump Rotordynamic Test Facility.**

The test section is equipped with a rotating dynamometer for the measurement of the forces and moments acting on the impeller. A forced whirl motion is obtained by generating the eccentricity by means of a two-shafts mechanism. The two shafts are mounted one inside the other and the whirl motion eccentricity can be finely adjusted before each rotordynamic test in the range between 0 and 2 mm by means of a double eccentric mount. The whirl motion is generated by a brushless motor driving the external shaft, while the impeller rotation is imparted by connecting the internal shaft to the main motor with an omokinetic coupling.

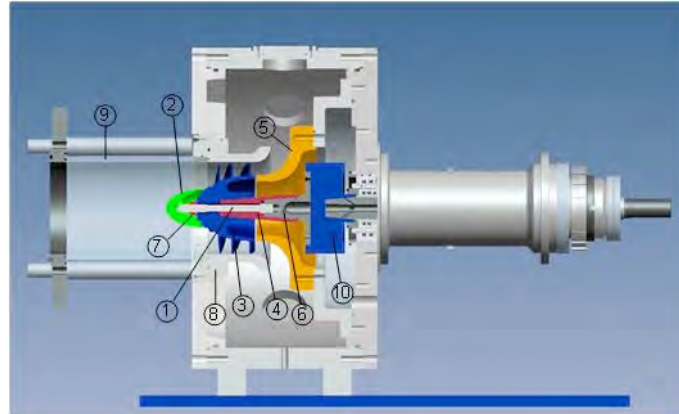
The rotating dynamometer is made of AISI 630 H1025 phase hardening steel and consists of two flanges connected by four posts of square cross-section acting as flexible elements. The posts deformations are measured by 40 semiconductor strain gauges arranged in 10 full Wheatstone bridges, which provide redundant measurements of the forces and moments acting on the impeller. Each bridge is temperature self-compensated up to 120 °C, with separate bipolar excitation and read-out for better reduction of cross-talking. The design of the sensing posts has been carried out as a result of a trade-off between acceptable sensitivity and sufficient structural resistance, operational stability and position control (stiffness). The dynamometer is optimized for a suspended mass of 4 kg with 70 mm gyration radius, an added mass of about 2 kg (based on the expected magnitude of the rotordynamic forces), a rotational speed of 3000 rpm without eccentricity, and maximum rotational and whirl speeds up to 2000 rpm with 2 mm shaft eccentricity.

Figure 37 shows a rendering of the test chamber assembly used for the experimental campaign. The rotating dynamometer (part 10) is placed between the inducer and the driving shaft. In order to reduce cantilever effects, the inducer has been recessed with respect to the optical access to the test section inlet. In this configuration the inducer blades are contained within the “inlet duct” (part 8). A nominal clearance of 2 mm allows for accommodating sufficiently large whirl eccentricities. The inducer is connected to the dynamometer (part 6) by means of a male/female conical endings adapter (part 4). A fastening shaft (part 1) is coupled on one side by means of a threaded hole machined in the conical interface of the dynamometer and on the other side by means of a nut (part 7).

The relative positions of the inducer (part 3) on the adapter (part 4) and of the adapter on the dynamometer interface (part 6) are guaranteed by means of two pins. A “radial diffuser” (part 5) has been mounted on the test section in order to reduce the suspended mass and minimize the interference with the measurement of

## Fluid Dynamics Associated to Launcher Developers

the forces acting on the inducer. In order to avoid water sloshing effects in the inducer assembly, e.g. within the nose (part 2), between the inducer and part 1, or between part 1 and part 4, the nose and the conical mounts of the inducer have been sealed by means of o-rings.



**Figure 37. Rendering of the Test Chamber Assembly.**

A Casio Exilim Pro EX-F1 digital photo-camera has been used for taking the high-speed movies discussed in the present paper, with a resolution up to 336 x 96 pixels at 1200 fps. Despite the low resolution at the highest frame rate, this compact photo-camera allows for taking relatively long movies, and therefore for adequately monitoring the development of the cavitating regions.

### 4.3 Test Inducer

The experimental campaign illustrated in the following has been conducted on the DAPAMITO4 inducer (the same inducer also used in the instability tests presented in the previous Section), whose main geometrical and operational parameters have already been reported in Table 3. As indicated earlier, the test inducer has been designed by means of the reduced order model described in Section 2 ([20] d'Agostino et al. 2008a, [21] d'Agostino et al. 2008b) and manufactured in 7075-T6 aluminum alloy, in order to reduce its weight and minimize the centrifugal component of the impeller forces measured by the rotating dynamometer during rotodynamic tests.

More in detail, the overall dimensions of this inducer have been chosen for ease of installation and testing in the current CPRTF configuration. A moderate value of the blade loading (with a diffusion factor  $D_F = 0.38$  as defined in [20] d'Agostino et al. 2008a, [21] d'Agostino et al. 2008b) and a high solidity ( $\sigma_r = 2.25$ ) have been chosen for reducing the leading-edge cavity and improving the suction performance. The value of the tip incidence-to-blade angle ratio  $\alpha/\beta_b < 0.5$  has been selected with the aim of controlling the danger of surge instabilities at design flow under cavitating conditions.

For what concerns the inducer performance, Figure 38 shows the noncavitating experimental curves of the DAPAMITO4 in terms of the static head coefficient  $\Psi = \Delta p / \rho \Omega^2 r_t^2$  and the hydraulic efficiency  $\eta = Q \Delta p_i / (\tau \Omega)$ , as functions of the flow coefficient  $\Phi = Q / \pi \Omega r_t^3$ . The curves have been obtained for a blade tip clearance equal to 2 mm and for two different values of the water temperature (ambient and about 50 °C), in order to analyze the possible influence of thermal cavitation effects. The highest measured efficiency, corresponding to the highest experimental flow coefficient ( $\Phi = 0.052$ ), is about 77%, in good agreement with the typical efficiency of this kind of turbomachines ( $\approx 70\div 80\%$ ).

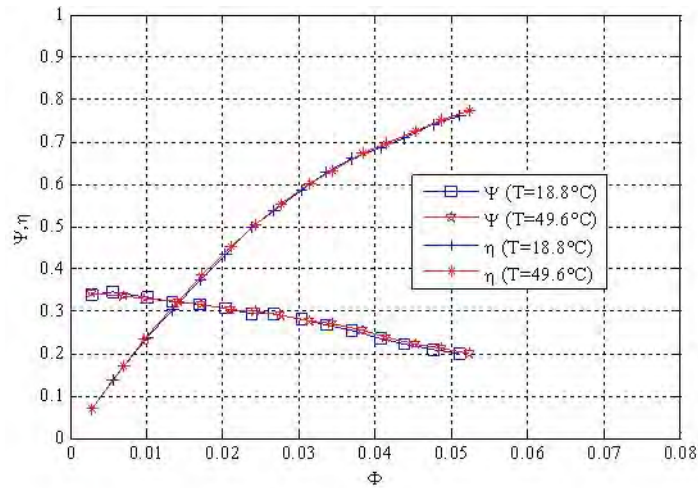


Figure 38. Noncavitating performance and hydraulic efficiency of the DAPAMITO4 inducer at different water temperatures.

#### 4.4 Experimental Procedure

The experiments presented in this paper have been conducted under forced vibration conditions, by imposing to the rotor a whirl trajectory represented by a circular orbit of fixed radius.

The generic components of the instantaneous forces acting on a whirling inducer have been schematized in the usual way, as shown in Figure 39.

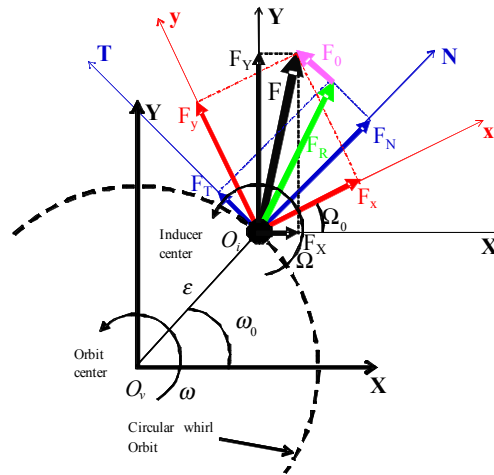


Figure 39. Rotordynamic forces in the laboratory and rotating reference frames.

The instantaneous force vector  $\vec{F}$  is expressed as the sum of a steady force  $\vec{F}_0$  (not depending on the presence of a whirl motion) and an unsteady force related to the perturbation vector  $\vec{\epsilon}$  by means of the rotordynamic matrix  $A$ :

## Fluid Dynamics Associated to Launcher Developers

$$\begin{bmatrix} F_X \\ F_Y \end{bmatrix} = \begin{bmatrix} F_{0X} \\ F_{0Y} \end{bmatrix} + \begin{bmatrix} A_{XX} & A_{XY} \\ A_{YX} & A_{YY} \end{bmatrix} \begin{bmatrix} \varepsilon \cos(\omega t + \varphi_0) \\ \varepsilon \sin(\omega t + \varphi_0) \end{bmatrix}$$

where  $\varphi_0$  is the anomaly of the eccentricity at the initial acquisition time  $t_0$ . Since the rotordynamic matrix  $A$  expresses a rotation + elongation transformation between two coplanar vectors, its elements satisfy the skew-symmetry conditions  $A_{XX} = A_{YY}$  and  $A_{XY} = -A_{YX}$ .

The normal and tangential forces with respect to the circular whirl orbit,  $F_N$  and  $F_T$ , can be expressed as functions of the elements of the rotordynamic matrix in the following way

$$F_N = \frac{1}{2}(A_{XX} + A_{YY}) = A_{XX} = A_{YY} \quad \text{and} \quad F_T = \frac{1}{2}(A_{YX} - A_{XY}) = -A_{XY} = A_{YX}$$

In the notation used in the present paper, the normal force  $F_N$  is positive when it is in the outward direction, while  $F_T$  is positive if it has the same direction as the rotational speed  $\Omega$ . Therefore a positive tangential force is destabilizing when the directions of the whirl motion and the shaft rotational motion are the same (i.e., the whirl/shaft speed ratio is positive) and stabilizing for a negative value of the whirl/shaft speed ratio. The normal force, conversely, is destabilizing when it is positive and tends to increase the radius of the whirl orbit.

The data presented in this paper are referred to purely fluid-induced forces; the effect of buoyancy and tare forces (the inducer dry weight and the centrifugal forces arising by running the inducer in air) have been subtracted from the total force. The unsteady rotordynamic forces have been normalized as follows ([1] Bhattacharyya 1994, [4] Bhattacharyya 1997)

$$F_N^* = \frac{F_N}{\pi \rho c_a \varepsilon \Omega^2 r_T^2} \quad \text{and} \quad F_T^* = \frac{F_T}{\pi \rho c_a \varepsilon \Omega^2 r_T^2}$$

where  $\rho$  is the fluid density,  $c_a$  is the axial length of the inducer blades at their tip,  $\varepsilon$  is the radius of the circular whirl orbit (eccentricity),  $\Omega$  is the inducer rotational speed and  $r_T$  is the inducer tip radius.

A novel experimental and data reduction procedure for the characterization of the rotordynamic forces has been recently developed at Alta, allowing for the measurement of the continuous spectra of the forces as functions of the whirl ratio. This new procedure consists in analyzing the rotordynamic forces in the rotating frame fixed to the dynamometer. In this frame, it can be shown that the forces measured by the dynamometer are linear in the absolute components of the radial force and in the elements of the rotordynamic matrix. This remarkable property can be used to determine the radial force and the rotordynamic matrix by applying a least-square method to the experimental data. All the plots shown in this paper have been obtained by means of this data reduction procedure, which is explained in detail in [83] Torre et al. 2011 and will not be illustrated again here.

In the following, the rotordynamic forces are reported both in terms of  $F_N^*$  and  $F_T^*$  and their non-dimensional modulus  $|\vec{F}_R^*| = \sqrt{(F_N^*)^2 + (F_T^*)^2}$  and phase angle  $\phi$  with respect to the eccentricity vector  $\vec{\varepsilon}$ , as functions of the whirl ratio  $\omega/\Omega$ . Figure 40 shows, as green, yellow, orange and red areas, the stability regions for positive (top) and negative (bottom) whirl ratios: the same colors have been used in the phase charts for highlighting the behavior of the rotordynamic forces.



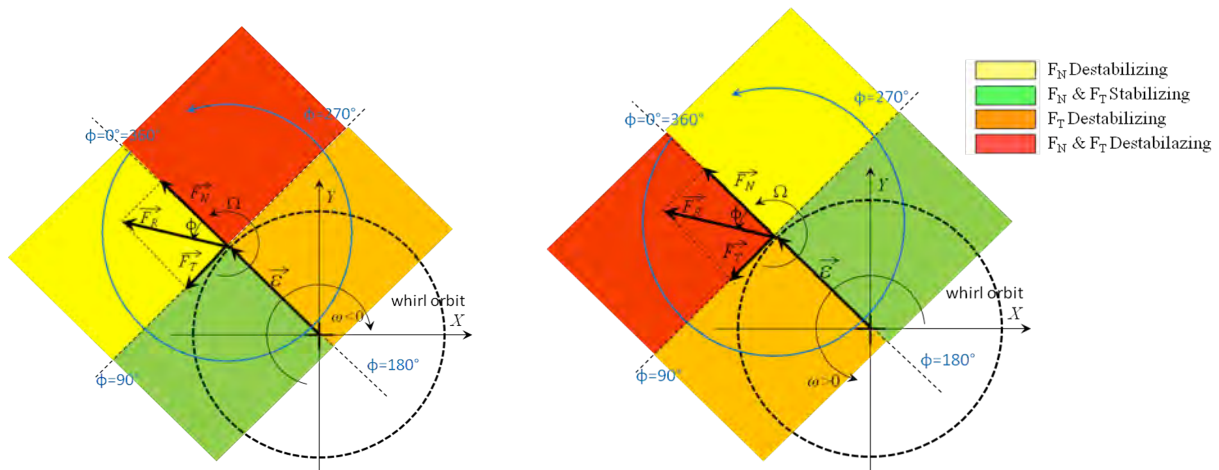


**Figure 40. Schematic representation of the stability regions for the normal and tangential components of the rotordynamic force, for positive (left) and negative (right) whirl ratios.**

The experiments shown in the present paper have been performed at an inducer rotating speed  $\Omega = 1750$  rpm, which represents a compromise value between the generation of measurable rotordynamic forces and the structural integrity of the rotating dynamometer. The eccentricity was equal to  $\varepsilon = 1.130$  mm and the flow coefficient was  $\Phi = 0.044$ . The cavitation number was about  $\sigma = 0.09$ , corresponding to significantly developed blade cavitation and a head drop equal to 11% of the nominal value (i.e., the inducer was already working under breakdown conditions). In addition, tests have been performed at two different water temperatures: about 20 °C and about 50 °C.

During the tests, high-speed movies of the whirling cavitating inducer have been taken by means of the digital photo-camera, installed in a lateral position with respect to the inlet duct, at a frame rate of 600 fps and a resolution of 432x192 pixels.

#### 4.5 Results and Discussion

The main results of the test campaign for the characterization of the rotordynamic forces on the DAPAMITO4 inducer ([83] Torre et al. 2001) can be summarized as follows:

- The influence of the flow coefficient could be identified in two concomitant effects: as the flow rate decreases the intensity of the rotordynamic force increases, while the spectrum tends to shift towards higher values of the whirl ratio.
- For negative whirl ratios the normal component showed a parabolic behavior, while the tangential one was almost linear; conversely, for positive whirl ratios, both the normal and tangential rotordynamic forces did not show a clear functional dependence on the whirl ratio.
- The intensity of the rotordynamic force clearly showed a minimum and a maximum for positive whirl ratios: the minimum corresponds to an impulsive variation of the angular phase, while the maximum takes place when the rotordynamic force becomes destabilizing.
- Under cavitating conditions, the minimum of the force at positive whirl ratios was found at the same value of  $\omega/\Omega$ , while the maximum was observed at lower values of  $\omega/\Omega$ ; the only stable range for positive whirl ratios was the interval between the minimum and the maximum, while for negative whirl ratios the cavitation tended to reduce the stabilizing range to a small interval close to zero.
- The rotordynamic forces were not affected by water temperature effects up to  $T = 50$  °C, under both

Fluid Dynamics Associated to Launcher Developers

non-cavitating and cavitating conditions.

In the following Figures, in particular, the results related to the operational point of interest for the present paper ( $\Phi = 0.044$ ,  $\sigma = 0.09$ ,  $\varepsilon = 1.130$  mm) are illustrated.

Figure 41 shows the normal and tangential components of the rotordynamic force, while Figure 42 shows its intensity and phase for two different water temperatures. The continuous spectra of the forces are reported together with the discrete results obtained in previous tests by means of the classical data reduction procedure ([64] Pasini et al. 2010): it is worth noticing that the continuous and the discrete results are perfectly superposed, thus confirming the effectiveness of the novel data reduction technique.

As already anticipated, no significant temperature effects can be observed on the force, except for some slight differences in its normal component at negative values of the whirl ratio. The force intensity shows a maximum at  $\omega/\Omega = 0.39$  and a minimum, very close to 0, at about  $\omega/\Omega = 0.10$  (Figure 42).

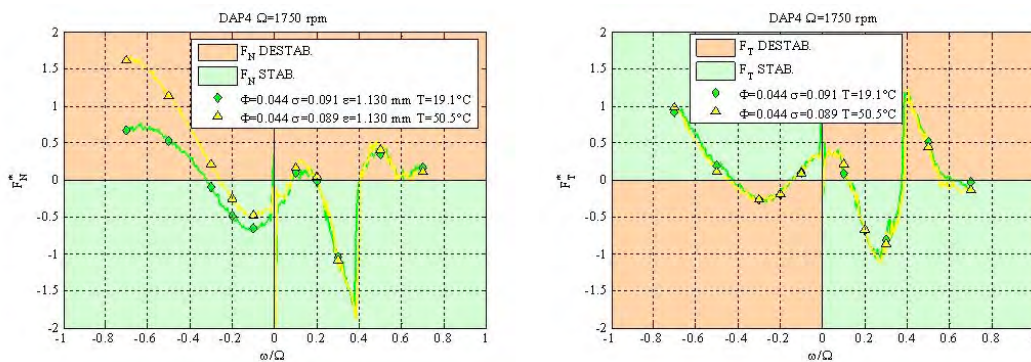


Figure 41. Normal and tangential components of the rotordynamic force, as functions of the whirl ratio, for  $\Phi = 0.044$ ,  $\sigma = 0.089$  and two different values of the water temperature.

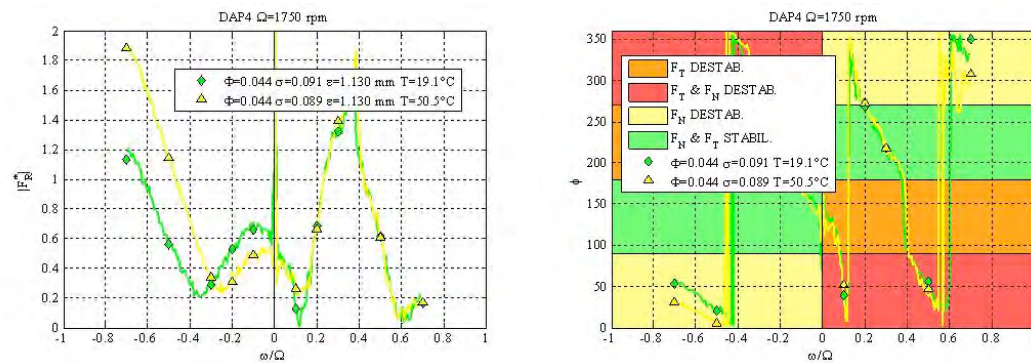


Figure 42. Intensity and phase of the rotordynamic force, as a function of the whirl ratio, for  $\Phi = 0.044$ ,  $\sigma = 0.089$  and two different values of the water temperature.

Figure 43 shows the frames extracted from a high-speed movie recorded during the continuous hot test at  $\Phi = 0.044$  under cavitating conditions ( $\sigma = 0.089$ ). The frames depict the test inducer at a whirl ratio corresponding to the destabilizing peak of the tangential rotordynamic force shown in Figure 8 ( $\omega/\Omega = 0.39$ ). The cavitating region (highlighted by solid red lines when in the foreground and dotted ones when in the background) appears to be organized in a single structure rotating at the same angular speed of the whirl motion, as shown by the analysis of the extracted frames: since the movie has been recorded at 600

fps and the inducer rotates at  $\Omega=1750$  rpm, a complete whirl orbit at the considered whirl ratio corresponds to 52 frames.

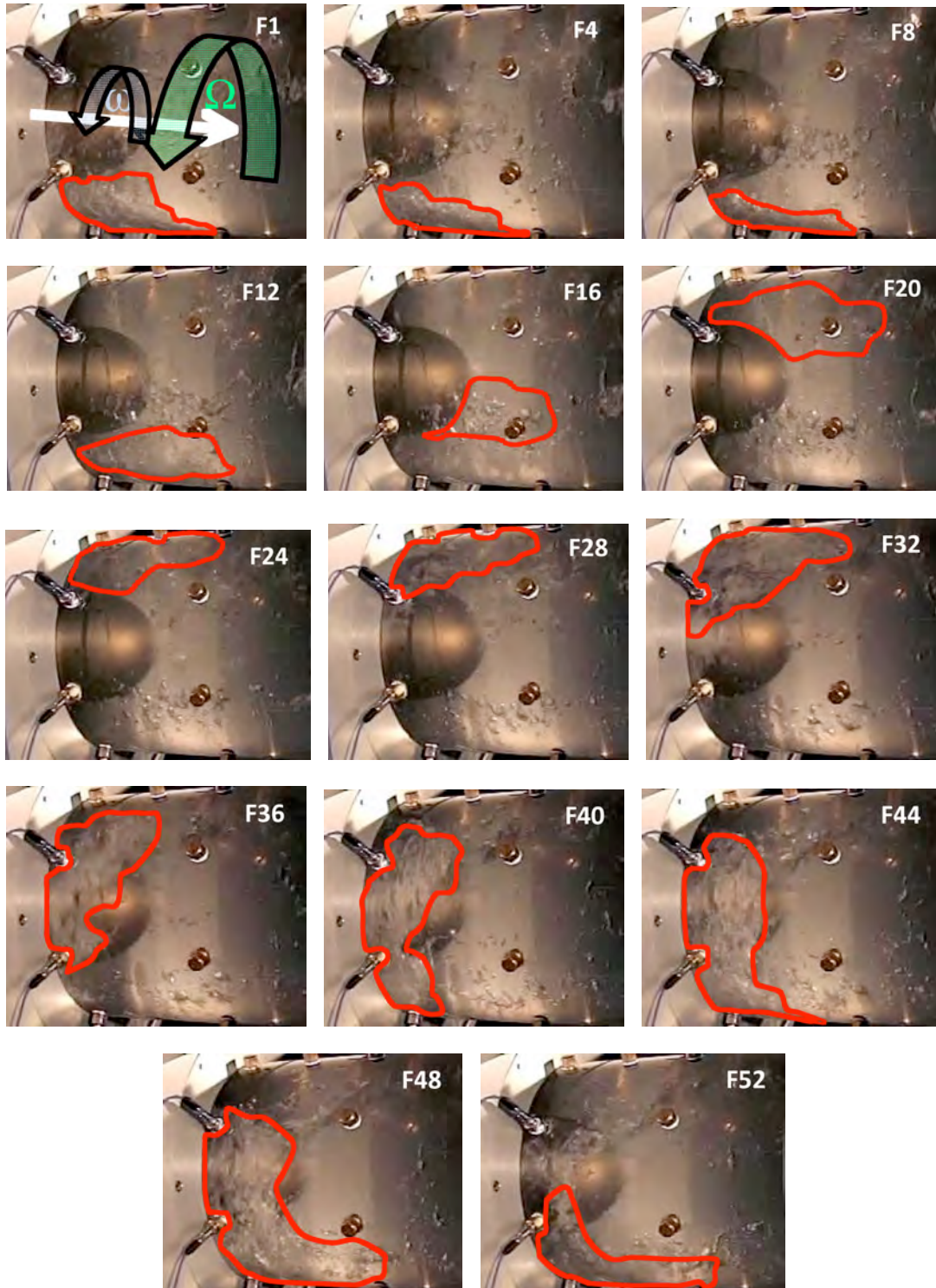


Figure 43. Frames extracted from a high-speed movie taken at 600 fps ( $\omega/\Omega = 0.39$ ,  $\phi = 0.044$ ,  $\sigma = 0.089$ ,  $T = 50.5$  °C).

Fluid Dynamics Associated to Launcher Developers

Under different whirling conditions (see Figure 44), the cavitating region does not appear to be solid, but is broken into several structures which change their aspect during the rotation, making it impossible to follow and analyze their paths.

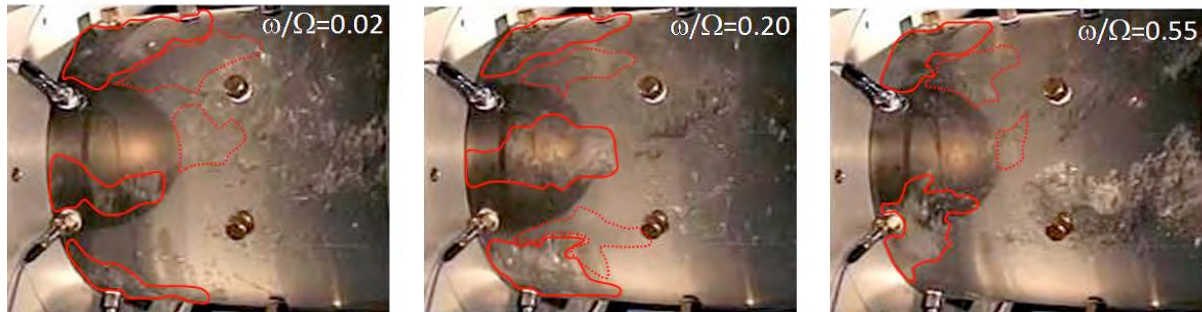


Figure 44. Appearance of the cavitating regions at different values of the whirl ratio ( $\Phi = 0.044$ ,  $\sigma = 0.089$ ,  $T = 50.5^\circ\text{C}$ ).

Figure 45 shows a combined representation of the information included in Figure 42. In particular, the rotordynamic force is represented in both intensity and phase for different positive (left) and negative (right) whirl ratios. It is worth noticing that the destabilizing force peak has the opposite direction with respect to the whirl eccentricity; furthermore, at the whirl ratio for which the peak is observed, a sudden transition between stabilizing (green) and strongly destabilizing (red) regions occurs.

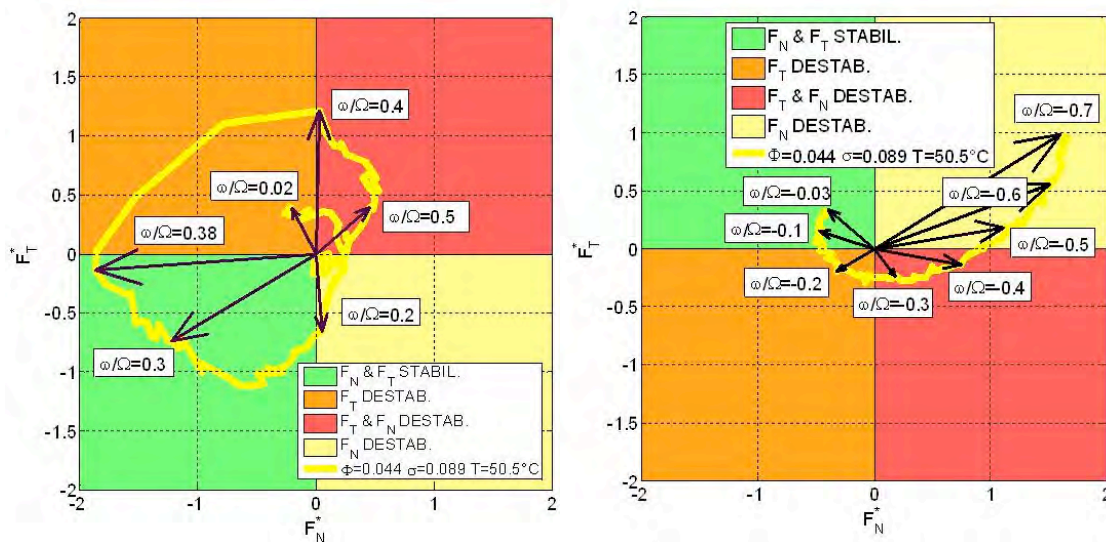


Figure 45. Rotordynamic force vector in the  $F_N^*$ -  $F_T^*$  plane for different positive (left) and negative (right) values of the whirl ratio ( $\Phi = 0.044$ ,  $\sigma = 0.089$ ,  $T = 50.5^\circ\text{C}$ ).

Conversely, Figure 46 shows the same kind of charts for a noncavitating condition ( $\Phi = 0.044$ ,  $\sigma = 0.918$ ,  $T = 50.6^\circ\text{C}$ ). In this case, the sudden transition from stabilizing to destabilizing conditions is not observed. At negative whirl ratios, the rotordynamic force shows a different behavior between cavitating and noncavitating conditions: not only the force intensity is higher when cavitation is present, but also its direction is completely different.

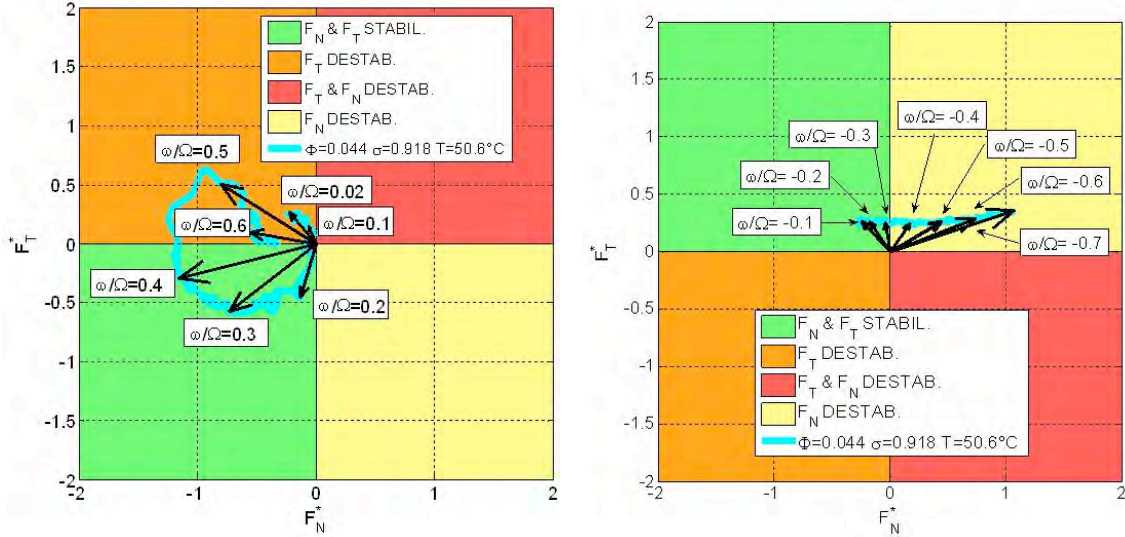


Figure 46. Rotordynamic force vector in the  $F_N^* - F_T^*$  plane for different positive values of the whirl ratio, under noncavitating conditions ( $\Phi = 0.044$ ,  $\sigma = 0.918$ ,  $T = 50.6^\circ\text{C}$ ).

#### 4.6 Conclusions

The general features of the rotordynamic forces measured on the DAPAMITO4 inducer are in good qualitative agreement with previous results obtained in a similar series of experiments conducted at the California Institute of Technology in the 1980's ([3] Bhattacharyya 1994, [4] Bhattacharyya et al. 1997). Under cavitating conditions, a destabilizing peak of the rotordynamic forces on the DAPAMITO4 inducer has been observed at a positive value of the whirl ratio. The analysis of the high-speed movies of the phenomenon has shown that the destabilizing force peak, observed when the rotordynamic force and the whirl eccentricity have opposite directions, is associated to the reorganization of the cavitating regions in the inducer backflow into a single, well defined structure synchronously rotating with the whirl motion. Conversely, at different values of the whirl ratio, cavitation is broken into several regions associated to backflow vortices, which do not seem to display a well-recognizable phase relation with respect to the whirl motion of the impeller eccentricity. As a confirmation of these findings, a previous experimental characterization of the flow instabilities on the same inducer has shown the onset of a rotating instability connected to the backflow vortices at a frequency comparable to the whirl frequency at which the rotordynamic force peak has been detected.

#### 5.0 CONCLUSIONS AND FUTURE WORK

In the last generation the technology and knowledge base of liquid propellant feed turbopumps has been completely revolutionized. The development of the propulsion systems for the Space Shuttle in the 1970's and of the Japanese launchers in the 1980's and early 1990's have represented corner points in the quest for higher performance and more detailed insight on the hydrodynamics of the flow field through the machine. As a consequence of these development efforts the design of turbopumps for space propulsion applications has rapidly evolved and their power density has raised by more than one order of magnitude with the successful introduction of faster, lighter and often supercritical machines. A large number of new types of

## **Fluid Dynamics Associated to Launcher Developers**

---

fluid dynamic instabilities, mostly induced by the occurrence of cavitation, have been identified both theoretically and experimentally, and field experience has confirmed their potentially dangerous nature. In addition, operation at supercritical speeds with non-negligible cavitation has significantly increased the importance of rotordynamic instabilities and the need for more accurate prediction of the critical speeds and their dependence on the properties of the flow.

Today cavitation phenomena in hydraulically operating turbomachinery cannot be safely predicted by theoretical or numerical methods because of the complexity of the physical phenomena involved, the imperfections and approximations of the physical models, and the insufficient temporal and spatial resolution of current numerical simulation tools. Hence experimentation still plays an essential role for technology progress in this field. Operational and economic limitations also clearly indicate that detailed experiments can only be effectively carried out on turbopumps under fluid dynamic and thermal cavitation similarity.

In recognition of these aspects, Alta's research group at Pisa has designed and realized the Cavitating Pump Rotordynamic Test Facility (CPRTF), the first openly documented facility in Europe – and one of the few in the world – capable of carrying out the direct measurement of the unsteady rotordynamic fluid forces on scaled turbopumps in fluid dynamic and thermal cavitation similarity.

As a natural development of our ongoing work in this field, the current objectives of our research team focus on:

- the experimental investigation of the dynamic transfer matrices relating the complex amplitudes of the pressure and flow perturbations at the inlet and outlet of cavitating turbopumps, in support to the understanding and control of POGO oscillations triggered by cavitation surge, which still represents a primary concern of rocket engine designers;
- the more extensive characterization of cavitation-induced rotordynamic fluid forces on turbopump impellers, in the perspective of more accurate evaluation of the dependence of the critical speeds of the machine on the form and extent of cavitation and the other operational conditions;

by means of similarity tests in the CPRTF. In particular, special attention will be paid to the influence of thermal cavitation effects on the above phenomena, since practically no systematic information is currently available on this aspect, which is universally recognized to be of special relevance in high vapor pressure liquids like most common space rocket propellants.

In general terms the final objective of the research unit at Alta consists in giving the designers of high performance turbopumps a deeper insight on the development of dangerous flow instabilities of crucial importance in rocket propulsion applications. In more practical terms, the results of the planned activities will provide experimental data on the dependence of these instabilities on the scaling parameters describing the operational conditions of the machine and the intensity of thermal effects, which commonly occur in most cryogenic propellants. By proper extrapolation based on well-established similarity laws, this information will allow for realistic predictions of these phenomena in full-scale turbomachines to be made, thereby effectively contributing to identify the operational regimes that are likely to develop into dangerous and potentially destructive fluid dynamic instabilities.

Together with the numerical simulations and theoretical analyses currently also being developed by the research team in Pisa, the above activities represent an integrated approach to the analysis of cavitation-induced instabilities in liquid propellant fuel feed systems and are expected to effectively contribute to the advancement of technology in an important sector of space engineering.

## 6.0 ACKNOWLEDGEMENTS

I wish to express my deepest gratitude to all of those who, over more than twenty years, made this lecture possible by building and promoting with their efforts the name and success of hydrodynamic research on space turbopumps at Alta and Pisa University. I am especially thankful to Profs. Mariano Andrenucci, Managing Director of Alta, and Renzo Lazzeretti, of Pisa University, for their constant encouragement, to Drs. Angelo Cervone, Lucio Torre, Angelo Pasini, Emilio Rapposelli, Cristina Bramanti and Fabrizio D'Auria for their brilliant and enthusiastic collaboration, to Giovanni Pace and Dario Valentini and all of my current and former students at Pisa University for their great help and for providing a longer perspective to my efforts. Very special thanks go to my doctoral mentors, Prof. Allan, J. Acosta and Prof. Christopher E. Brennen of the California Institute of Technology, USA, who first stimulated my interest in the hydrodynamics of cavitating turbopumps, and to my elder colleague Prof. Yoshinobu Tsujimoto of Osaka University, Japan, from whom I never stopped to learn more. Most of the work presented in this lecture has been supported by ESA and ASI and I gratefully acknowledge the supervision of Dr. Giorgio Saccoccia and Johan Steelant, who acted as contract monitors for ESA's contracts.

## 7.0 NOMENCLATURE

### 7.1 Latin Symbols

$a$	distance of the maximum camber point from the leading edge
$A$	rotordynamic matrix, area of the section
$\mathbf{A}$	rotordynamic matrix
$A_{ij}$	element of the rotordynamic matrix
$B$	flow blockage
$c$	blade chord
$c_a$	full-blade axial length
$C_L$	lift coefficient
$c_p$	constant pressure specific heat
$C_p$	pressure coefficient
$C_{p_{\min}}$	minimum pressure coefficient
$c_{\%}$	tip clearance/mean blade height ratio
$D$	diameter, diffusion factor
$\underline{D}$	vector of the forces in the lateral plane w.r.t. the rotating frame $\underline{D} = (F_x, F_y)$
$D_{ch}$	hydraulic diameter of blade channels
$df$	frequency resolution
$D_F$	diffusion factor
$f$	frequency, friction coefficient
$F$	generalized dimensional force
$F^*$	generalized nondimensional force
$f_{RC}$	rotating cavitation frequency
$g$	gravity acceleration
$h$	specific enthalpy
$H$	head

**Fluid Dynamics Associated to Launcher Developers**


---

$h_m$	mean blade height
$I, J$	integer numbers
$L$	axial length
$\ell$	cavity length
$L_{cav}$	cavity length
$L_{ch}$	effective length of blade channels
$L_{eq}$	equivalent duct length
$L_{th}$	blade cavity length
$m$	mass
$M$	mass flow gain factor
$m_c$	Carter's rule coefficient
$\dot{m}$	mass flow rate
$N$	number of blades, number of points, rotational speed
$n$	integer index, active nuclei concentration
$n_c$	number of rotating cells
$Nu$	Nusselt number
$p$	static pressure
$P$	(local) blade pitch
$p_{in}$	inlet static pressure [Pa]
$p_t$	total pressure
$p_V$	vapor pressure [Pa]
$Pr$	Prandtl number
$Q$	volumetric flow rate
$Q_{vap}$	latent heat of vaporization
$r$	radial coordinate
$R$	bubble radius
$\underline{R}$	vector of the "unknowns" ( $F_{0x}, F_{0y}, A_{xx}, A_{xy}, A_{yx}, A_{yy}$ )
$r_C$	casing radius
$r_H$	impeller hub radius
$r_k$	component of the vector $\underline{R}$
$r_M$	impeller mean radius
$r_T$	impeller tip radius
$Re$	Reynolds number $Re = 2\Omega r_T^2 / \nu$
$s$	azimuthal blade spacing
$t$	time
$T$	temperature, spectral temporal length
$t_C$	critical time for cavity growth
$T_C$	critical temperature, fundamental reference period
$\mathbf{u}$	flow velocity vector
$u$	radial flow velocity
$U$	free-stream boundary layer velocity



$U_{ref}$	reference velocity
$u_t$	radial speed at blade tip
$U_\infty$	free stream velocity
$v$	azimuthal flow velocity
$V$	mean axial velocity, volume
$v_\theta$	tangential speed
$w$	axial velocity
$X$	Fourier transform of the $x$ -signal
$y$	signal
$Z$	number of blades
$z$	axial coordinate

## 7.2 Greek Symbols

$\alpha$	thermal diffusivity, incidence angle, volume fraction
$\beta$	tip blade angle
$\beta_b$	blade angle evaluated w.r.t. the normal to the axial direction
$\beta'_2$	relative discharge flow angle without deviation
$\gamma$	blade angle from axial direction, coherence function, specific heat ratio
$\gamma_{xy}$	coherence function of $x, y$ -signals
$\delta$	tip clearance, boundary layer thickness
$\delta^*$	boundary layer displacement thickness
$\delta_T$	thermal BL thickness
$\Delta h_v$	head shift due to thermal cavitation effects
$\Delta p$	static pressure rise
$\Delta p_t$	total pressure rise
$\Delta t$	sampling interval
$\Delta T$	differential temperature
$\Delta \theta$	angular separation in the azimuthal direction
$\varepsilon$	radius of the whirl orbit (eccentricity)
$\eta$	hydraulic efficiency
$\vartheta$	azimuthal coordinate, angle of attack
$\theta^*$	boundary layer momentum thickness
$\nu$	kinematic viscosity
$\rho$	flow density
$\sigma$	cavitation number, blade solidity, standard deviation
$\tau$	torque
$\varphi$	cross-correlation phase
$\phi$	phase angle
$\Phi$	flow coefficient
$\Phi_D$	design flow coefficient
$\psi$	slip velocity stream function

## Fluid Dynamics Associated to Launcher Developers

---

$\Psi$	static head coefficient
$\Psi_t$	total head coefficient
$\omega$	whirl rotational speed
$\Omega$	rotational speed
$\omega_0$	anomaly of the eccentricity @ $t_0$
$\Omega_A$	auto-oscillation frequency
$\Omega_s$	specific speed
$\tilde{\Omega}$	angular position of the rotating $x$ -axis w.r.t. the absolute one $X$
$\Omega_0$	angular position of the rotating $x$ -axis w.r.t. the absolute one $X$ at $t_0$

### 7.3 Subscripts

$B$	bubble
$C$	critical conditions
$D$	design conditions
$H$	hub radius
$in$	at the upstream pressure tap, inertially –dominated
$L$	liquid
$le$	leading edge
$N$	normal to the whirl orbit
$NC$	non-cavitating operation
$out$	at the downstream pressure tap
$R$	rotordynamic force modulus
$ref$	reference condition
$sat$	saturation conditions
$t$	total quantity (i.e. $p_{t1}$ = total pressure at section 1)
$T$	tip radius/ tangent to the whirl orbit
$te$	trailing edge
$th$	thermally-dominated
$v$	vapor pressure
$V$	vapor phase
$x, y$	rotating reference frame
$X, Y$	absolute reference frame
$\delta^\circ$	flow deviation angle
0	initial condition, steady forces, initial time, zero lift
1	upstream station
2	downstream station

### 7.4 Superscripts

$q'$	value of $q$ in the rotating frame
$\bar{q}$	mean value of $q$
$\hat{u}$	fully-guided flow velocity
$\tilde{u}$	slip flow velocity

## 7.5 Acronyms

<i>AO</i>	Axial Oscillation
<i>BO</i>	Backflow Oscillation
<i>BVI</i>	Backflow Vortices Instability
<i>CPRTF</i>	Cavitating Pump Rotordynamic Test Facility
<i>MBT</i>	Moved Back Transducers
ODE	ordinary differential equation
<i>RC</i>	Rotating Cavitation
<i>S</i>	Surge
<i>SRC</i>	Synchronous Rotating Cavitation
<i>STCE</i>	Scaling of Thermal Cavitation Effects
2D	two-dimensional
3D	three-dimensional

## 8.0 REFERENCES

- [1] Acosta A. J., 1958, "An Experimental Study of Cavitating Inducers", Proceedings of the Second ONR Symposium on Naval Hydrodynamics, ONR/ACR-38, 533-557.
- [2] Ashihara K., Goto A., Kamijo K., Yamada H., Uchiumi M., 2002, "Improvements of Inducer Inlet Backflow Characteristics Using 3-D Inverse Design Method", 38th AIAA/ASME/SAE/ASEE Joint Propulsion Conference, Indianapolis, USA.
- [3] Bhattacharyya A., 1994, "Internal Flows and Force Matrices in Axial Flow Inducers", Ph. D. Thesis, Report no. E249.18, California Institute of Technology, Pasadena, USA.
- [4] Bhattacharyya A., Acosta A. J., Brennen C. E., Caughey T. K., 1997, "Rotordynamic Forces in Cavitating Inducers", ASME Journal of Fluids Engineering, 199(4), pp.768-774.
- [5] Braisted D. M., 1979, "Cavitation Induced Instabilities Associated with Turbomachines", Report No. E184.2, California Institute of Technology, 1979.
- [6] Bramanti C., Cervone A., d'Agostino L., 2007, "A Simplified Analytical Model for Evaluating the Noncavitating Performance of Axial Inducers", 43rd AIAA/ASME/SAE/ASEE Joint Propulsion Conference, Cincinnati, USA.
- [7] Brennen C.E., 1978, "Bubbly Flow Model for the Dynamic Characteristics of Cavitating Pumps", J. of Fluid Mechanics, Vol. 89, part 2, pp. 223-240.
- [8] Brennen C. E., 1994, "Hydrodynamics of Pumps", Oxford University Press, Oxford Engineering Science Series 44.
- [9] Brennen C.E., 1995, "Cavitation and Bubble Dynamics", Oxford University Press.
- [10] Brennen C.E., Acosta A.J., 1973, "Theoretical, Quasi-Static Analysis of Cavitation Compliance in Turbopumps", J. of Spacecraft, Vol. 10, No. 3, pp. 175-179.
- [11] Brennen C.E. and Acosta A.J., 1976, "The Dynamic Transfer Function for a Cavitating Inducer",

---

**Fluid Dynamics Associated to Launcher Developers**

---

- ASME J. Fluids Eng., Vol. 98, pp. 182-191.
- [12] Callenaere M., Franc J. P., Michel J. M., 1998, "Influence of Cavity Thickness and Pressure Gradient on the Unsteady Behaviour of Partial Cavities", 3rd International Symposium on Cavitation, Grenoble, France, April 7-10.
- [13] Cervone A., Testa R., Bramanti C., Rapposelli E. and d'Agostino L., 2005, "Thermal Effects on Cavitation Instabilities in Helical Inducers", AIAA Journal of Propulsion and Power, Vol. 21, No. 5, Sep-Oct 2005, pp. 893-899.
- [14] Cervone A., Torre L., Bramanti C., Rapposelli E., d'Agostino L., 2006b, "Experimental Characterization of Cavitation Instabilities in a Two-Bladed Axial Inducer", AIAA Journal of Propulsion and Power, Vol. 22, No. 6, pp. 1389-1395.
- [15] Cervone A., Bramanti C., Torre L., Fotino D., d'Agostino L., 2007, "Setup of a High-Speed Optical System for the Characterization of Flow Instabilities Generated by Cavitation", ASME Journal of Fluids Engineering, Vol. 129, Is. 7, pp. 877-885.
- [16] Cooper P., 1967, "Analysis of Single- and Two-Phase Flows in Turbopump Inducers", ASME J. of Engineering for Power, October 1967, pp. 577-588.
- [17] d'Agostino L., d'Auria F. and Brennen C.E., 1998, "A Three-Dimensional Analysis of Rotordynamic Forces on Whirling and Cavitating Helical Inducers", ASME Journal of Fluids Engineering, Vol. 120, pp. 698-704.
- [18] d'Agostino L. and Venturini-Autieri M.R., 2002, "Three-Dimensional Analysis of Rotordynamic Fluid Forces on Whirling and Cavitating Finite-Length Inducers", 9th Int. Symp. on Transport Phenomena and Dynamics of Rotating Machinery (ISROMAC-9), Honolulu, USA.
- [19] d'Agostino L. and Venturini-Autieri M.R., 2003, "Rotordynamic Fluid Forces on Whirling and Cavitating Radial Impellers", CAV 2003, 5th International Symposium on Cavitation, Osaka, Japan
- [20] d'Agostino L., Torre L., Pasini, A. Cervone, A., 2008a, "On the Preliminary Design and Noncavitating Performance of Tapered Axial Inducers", ASME Journal of Fluids Engineering, 130 (11).
- [21] d'Agostino L., Torre L., Pasini A., Baccarella D., Cervone A., Milani A., 2008b, "A Reduced Order Model for Preliminary Design and Performance Prediction of Tapered Inducers: Comparison with Numerical Simulations", Proc. 44th AIAA/ASME/SAE/ASEE Joint Propulsion Conference, Hartford, USA.
- [22] d'Agostino, L., Pasini, A., Valentini, D., 2011, "A Reduced Order Model for Preliminary Design and Performance Prediction of Radial Turbopumps", 47th AIAA/ASME/SAE/ASEE Joint Propulsion Conference, San Diego, California, USA, July 31-August 3.
- [23] d'Agostino L., Pasini A., Valentini D., Pace G., Torre L., Cervone A., 2012, "A Reduced Order Model for Optimal Centrifugal Pump Design", 14th Int. Symp. on Transport Phenomena and Dynamics of Rotating Machinery, ISROMAC-14, February 27th – March 2, 2012, Honolulu, HI, USA.
- [24] d'Auria F., d'Agostino L. and Brennen C.E., 1995, "Bubble Dynamic Effects on the Rotordynamic Forces in Cavitating Inducers", 1995 ASME Fluids Engineering Summer Meeting, Hilton Island, South Carolina, USA, August 13-18.

---

**Fluid Dynamics Associated to Launcher Developers**

---

- [25] Ehrich F., Childs S. D., 1984, "Self-Excited Vibrations in High Performance Turbomachinery", *Mechanical Engineering*, May, pp. 66-79.
- [26] Franc J. P., 2001, "Partial Cavity Instabilities and Re-Entrant Jet", CAV2001, Int. Symposium on Cavitation, Pasadena, California, USA, June 20-23.
- [27] Franz R. J., 1989, "Experimental Investigation of the Effect of Cavitation on the Rotordynamic Forces on a Whirling Centrifugal Pump Impeller", Ph.D. Thesis, California Institute of Technology, Pasadena, USA.
- [28] Fuji A., Azuma S., Yoshida Y., Tsujimoto Y., 2002, "Higher Order Rotating Cavitation in an Inducer", *Proceedings of ISROMAC-9 - the 9th International Symposium on Transport Phenomena and Dynamics of Rotating Machinery*, Honolulu, Hawaii, USA, February 10-14.
- [29] Fujii A., Mizuno S., Horiguchi H. and Tsujimoto Y., 2005, "Suppression of Cavitation Instabilities by Jet Injection at Inducer Inlet", *ASME Fluid Engineering Division Summer Meeting and Exhibition (FEDSM2005)*, Houston, USA.
- [30] Furukawa A., Ishizaka K., Watanabe S., 2001, "Experimental Estimate of Helical Inducer Blade Forces in Cavitation Surge Condition", CAV2001, International Symposium on Cavitation, Pasadena, California USA, June 20-23.
- [31] Furukawa A., Ishizaka K., Watanabe S., 2002, "Experimental Study of Cavitation Induced Oscillation in Two Bladed Inducers", *Space Launcher Liquid Propulsion: 4th International Conference on Space Launcher Technology*, Liege, Belgium.
- [32] Goirand B., Mertz A. L., Joussefin F. and Rebattet C., 1992, "Experimental Investigations of Radial Loads Induced by Partial Cavitation with Liquid Hydrogen Inducer", *IMEchE*, C453/056, pp. 263-269.
- [33] Greitzer E. M., 1981, "The Stability of Pumping Systems – The 1980 Freeman Scholar Lecture", *ASME Journal of Fluids Engineering*, Vol.103, pagg. 193-242, June 1981.
- [34] Hashimoto T., Yoshida H., Funatsu S., Hishimoto J., Kamijo K., Tsujimoto Y., 1997, "Rotating Cavitation in Three and Four-Bladed Inducers", *33th AIAA/ASME7SAE/ASEE Joint Propulsion Conference and Exhibit*, Seattle, USA.
- [35] Hashimoto T., Yoshida H., Watanabe M., Kamijo K., Tsujimoto Y., 1997b, "Experimental Study on Rotating Cavitation of Rocket Propellant Pump Inducers", *J. Propulsion and Power*, Vol. 13, No. 4.
- [36] Hergt P., Krieger P., 1969, "Radial Forces in Centrifugal Pumps with Guide Vanes", *Proc. Inst. Mech. Eng.*, 184, Part 3N, pp. 101-107.
- [37] Higashi S., Yoshida Y. and Tsujimoto Y., 2001, "Tip Leakage Vortex Cavitation from the Tip Clearance of a Single Hydrofoil", CAV2001, International Symposium on Cavitation, Pasadena, California, USA, June 20-23.
- [38] Hildebrand F.B., 1976, "Advanced Calculus for Applications", 2nd edition, Prentice Hall.
- [39] Horiguchi H., Watanabe S. and Tsujimoto Y., 2000, "Theoretical Analysis of Cavitation in Inducers with Unequal Blades with Alternate Leading Edge Cutback: Part I- Analytical Methods and Results for Smaller Amount of Cutback", *Journal of Fluids Engineering*, Vol. 5.

---

**Fluid Dynamics Associated to Launcher Developers**

---

- [40] Horiguchi H., Arai S., Fukutomi J., Nakase Y., Tsujimoto Y., 2003b, "Quasi Three-Dimensional Analysis of Cavitation in an Inducer", 4th ASME-JSME Joint Fluids Engineering Conference, Honolulu, Hawaii, USA, July 6-10.
- [41] Imamura H., Kurokawa J., Matsui J., Kikuchi M., 2003, "Suppression of Cavitating Flow in Inducer by J-Groove", CAV2003, Int. Symposium on Cavitation, Osaka, Japan, November 1-4.
- [42] Jakobsen J.K., 1971, "Liquid Rocket Engine Turbopump Inducers", NASA SP 8052.
- [43] Janigro A. and Ferrini F., 1973, "Inducer Pumps" in Recent Progress in Pump Research, von Karman Institute for Fluid Dynamics, Lecture Series 61.
- [44] Jery B., 1987, "Experimental Study of Unsteady Hydrodynamic Force Matrices on Whirling Centrifugal Pump Impellers", Report no. 200.22, California Institute of Technology, Pasadena, USA.
- [45] Kamjio K., Shimura T., Watanabe M., 1977, "An Experimental Investigation of Cavitating Inducer Instability", ASME Paper n. 77-WA/FW-14.
- [46] Kamjio K., Yoshida M. and Tsujimoto Y., 1993, "Hydraulic and Mechanical Performance of LE-7 LOX Pump Inducer", AIAA Journal of Propulsion and Power, Vol. 9 (6): pp. 819-826.
- [47] Kang D., Cervone A., Yonezawa K., Horiguchi H., Kawata Y., Tsujimoto Y., 2007, "Effect of Blade Geometry on Tip Leakage Vortex of Inducer", The 9th Asian International Conference on Fluid Machinery, Jeju, South Korea.
- [48] Kawanami Y., Kato H., Yamaguchi H., Tagaya Y., Tanimura M., 1997, "Mechanism and Control of Cloud Cavitation", J. of Fluids Eng., Vol. 119, pp. 788-795.
- [49] Kimura T., Yoshida Y., Hashimoto T., Shimagaki M., 2006, "Numerical Simulation for Unsteady Cavitating Flow in a Turbopump Inducer", CAV2006, 6th Int. Symposium on Cavitation, Wageningen, The Netherlands.
- [50] Kjeldsen, M., Effertz, M., Arndt, R. E. A., "Investigation of Unsteady Cavitation Phenomena", Proceedings of US-Japan Seminar: Abnormal Flow Phenomena in Turbomachinery, Osaka, Japan, Nov. 1-6, 1998.
- [51] Kubota A., Kato H., Yamaguchi H., Maeda M., 1989, "Unsteady Structure Measurement of Cloud Cavitation on a Foil Section Using Conditional Sampling Technique", J. of Fluids Eng., Vol. 111, pp. 204-210.
- [52] Lakshminarayana B., 1982, "Fluid Dynamics of Inducers - A Review", ASME J. of Fluids Engineering, Vol. 104, pp. 411-427.
- [53] Lieblein S., Schwenk F.C. and Broderick R.L., 1953, "Diffusion Factor for Estimating Losses and Limiting Blade Loadings in Axial Flow Compressor Blade Elements", NACA RM E53D01.
- [54] Lieblein S., 1965, "Experimental flow in Two-Dimensional Cascades", Aerodynamic Design of Axial Flow Compressors, NASA SP-36, 101-149.
- [55] Murai H., 1968, "Observations of Cavitation and Flow Patterns in an Axial Flow Pump at Low Flow Rates", Mem. Inst. High Speed Mech., Tohoku Univ., 24, No.246.

---

**Fluid Dynamics Associated to Launcher Developers**

---

- [56] NASA, 1970, "Prevention of Coupled Structure-Propulsion Instability", NASA SP-8055, Space Vehicle Design Criteria Manuals.
- [57] NASA, 1971, "Liquid Rocket Engine Turbopump Inducers", NASA SP-8052, Space Vehicle Design Criteria Manuals.
- [58] NASDA, 2000a, Report No. 94, May 2000.
- [59] NASDA, 2000b, Report No. 96, June 2000.
- [60] Natanzon M. S. et al., 1974, "Experimental Investigation of Cavitation Induced Oscillations of Helical Inducers", Fluid Mech. Soviet Res., Vol. 3 No. 1, pp.38-45.
- [61] Ng S.L. and Brennen C.E., 1978, "Experiments on the Dynamic Behavior of Cavitating Pumps", ASME J. Fluids Eng., Vol. 100, No. 2, pp. 166-176.
- [62] Ohashi H., Shoji H., 1984, "Lateral Fluid Forces Acting on a Whirling Centrifugal Impeller in Vaneless and Vaned Diffuser", Proc. Workshop on Rotordynamic Instability Problems in High Performance Turbomachinery, NASA Conf. Publ. 2338, pp. 109-122.
- [63] Ohta T., Kajishima T., 2008, "Transition of Different Unsteady Cavitating Flows in 2D Cascade with Flat Blades", Proceedings of ISROMAC-12 - the 12th International Symposium on Transport Phenomena and Dynamics of Rotating Machinery, Honolulu, Hawaii, USA, February 17-22.
- [64] Pasini A., Torre L., Cervone A., d'Agostino L., 2010, "Rotordynamic Forces on a Four Bladed Inducer", Proc. 46th AIAA/ASME/SAE/ASEE Joint Propulsion Conference, Nashville, USA.
- [65] Rapposelli E., Cervone A., d'Agostino L., 2002, "A New Cavitating Pump Rotordynamic Test Facility", AIAA Paper 2002-4285, Proc.38th AIAA/ASME/SAE/ASEE Joint Propulsion Conference, Indianapolis, USA.
- [66] Rosenmann W., 1965, "Experimental Investigations of Hydrodynamically Induced Shaft Forces With a Three Bladed Inducer", Proc. ASME Symp. on Cavitation in Fluid Machinery.
- [67] Rubin S., 1966, "Longitudinal Instability of Liquid Rockets Due to Propulsion Feedback (POGO)", J. Spacecraft and Rockets, Vol. 3, No. 8, pp. 1188-1195.
- [68] Ryan R.S., Gross L.A., Mills D. and Michell P., 1994, "The Space Shuttle Main Engine Liquid Oxygen Pump High-Synchronous Vibration Issue, the Problem, the Resolution Approach, the Solution", 30th AIAA/ASME/SAE/ASEE Joint Propulsion Conference, Indianapolis, USA.
- [69] Sack L. E., Nottage H. B., 1965, "System Oscillations Associated to Cavitating Inducers", ASME J. Basic Eng., Vol. 87, pp. 917-924.
- [70] Sakoda M., Yakushiji R., Maeda M., Yamaguchi H., 2001, "Mechanism of Cloud Cavitation Generation on a 2-D Hydrofoil", CAV2001, Int. Symposium on Cavitation, Pasadena, California, USA, June 20-23.
- [71] Sargent S. R., Sorensen K. P., McGlynn R. D., 2008, "Measurement of Cavitation Induced Strain on a 3 Bladed Inducer", Proceedings of ISROMAC-12 - the 12th International Symposium on Transport Phenomena and Dynamics of Rotating Machinery, Honolulu, Hawaii, USA, February 17-22.

---

**Fluid Dynamics Associated to Launcher Developers**

---

- [72] Semenov Y. A., Fujii A., Tsujimoto Y., 2004, “Rotating Choke in Cavitating Turbopump Inducer”, ASME Journal of Fluids Engineering, Vol. 126, pp. 87-93.
- [73] Shimagaki M., Hashimoto T., Watanabe M., Hasegawa S., Nakamura N., Shimura T., 2006, “Unsteady Pressure Fluctuations in an Inducer”, JSME Int. Journal of Fluids and Thermal Engineering, Series B, Vol. 49, No. 3, pp. 806-811.
- [74] Shimiya N., Fujii A., Horiguchi H., Uchiumi M., Kurokawa J., Tsujimoto Y., 2006 , “Suppression of Cavitation Instabilities in an Inducer by J-Groove”, CAV2006, 6th Int. Symposium on Cavitation, Wageningen, The Netherlands.
- [75] Shimura T., Yoshida M., Kamijo K., Uchiumi M., Yasutomi Y., 2002, “Cavitation Induced Vibration Caused by Rotating-Stall-Type Phenomenon in LH2 Turbopump”, Proceedings of ISROMAC-9 - the 9th International Symposium on Transport Phenomena and Dynamics of Rotating Machinery, Honolulu, Hawaii, USA, February 10-14.
- [76] Shimura T., Shimagaki M., Watanabe Y., Hasegawa S. and Tanaka S., 2003, “Cavitation Induced Vibration of LE-7A Oxygen Turpopump”, OS-4-009, CAV 2003, 5th International Symposium on Cavitation, Osaka, Japan, November 1-4.
- [77] Stripling L.B. and Acosta A.J., 1962, "Cavitation in Turbopumps – Part 1”, ASME J. Basic Eng., Vol. 84, pp. 326-338.
- [78] Subbaraman M., Patton M., 2006, “Suppressing Higher-Order Cavitation Phenomena in Axial Inducers”, CAV2006, 6th Int. Symposium on Cavitation, Wageningen, The Netherlands.
- [79] Suzuki T., Prunieres R., Horiguchi H., Tsukiya T., Taenaka Y., Tsujimoto Y., 2006, “Measurements of Rotordynamic Forces on an Artificial Heart Pump Impeller”, Proc. 23rd IAHR Symposium, Yokohama, Japan.
- [80] Tomaru H., Ugajin H., Kawasaki S., Nakano M., 2007, “Suppression of Cavitation Surge in a Turbopump Inducer by the Backflow Restriction Step”, 43rd AIAA/ASME/SAE/ASEE Joint Propulsion Conference, Cincinnati, USA.
- [81] Torre L., Pace G., Miloro P., Pasini A., Cervone A., d’Agostino L., 2010, “Flow Instabilities on a Three Bladed Axial Inducer at Variable Tip Clearance”, 13th International Symposium on Transport Phenomena and Dynamics of Rotating Machinery, Honolulu, Hawaii, USA, April.
- [82] Torre L., Pasini A., Cervone A., Pecorari L., Milani A., d’Agostino, L., 2010, “Rotordynamic Forces on a Three Bladed Inducer”, Proc. Space Propulsion Conference, San Sebastian, Spain.
- [83] Torre L., Pasini A., Cervone A., d’Agostino L., 2011, “Continuous Spectrum of the Rotordynamic Forces on a Four Bladed Inducer”, ASME/JSME/KSME Joint Fluids Engineering Conference, Hamamatsu, Japan.
- [84] Tsujimoto Y., Kamijo K., Yoshida Y., 1993, “A Theoretical Analysis of Rotating Cavitation in Inducers”, Journal of Fluids Engineering, Vol. 115.
- [85] Tsujimoto Y., Semenov Y. A., 2002, “New Types of Cavitation Instabilities in Inducers”, Space Launcher Liquid Propulsion: 4th International Conference on Space Launcher Technology, Liege, Belgium.



---

**Fluid Dynamics Associated to Launcher Developers**

---

- [86] Tsujimoto Y., Yoshida Y., Maekawa Y., Watanabe S., Hashimoto T., 1997, "Observations of Oscillating Cavitation of an Inducer", ASME Journal of Fluids Engineering, Vol. 119, pp. 775-781.
- [87] Tsujimoto Y., Watanabe S., Horiguchi H., 1998, "Linear Analyses of Cavitation Instabilities of Hydrofoils and Cascades", Proc. of US-Japan Seminar: Abnormal Flow Phenomena in Turbomachinery, Osaka, Japan, Nov. 1-6.
- [88] Tsujimoto Y., 2001, "Simple Rules for Cavitation Instabilities in Turbomachinery", CAV2001, Int. Symposium on Cavitation, Pasadena, California, USA, June 20-23.
- [89] Tsujimoto Y., Horiguchi H., Qiao X., 2005, "Backflow from Inducer and its Dynamics", ASME Fluid Engineering Division Summer Meeting and Exhibition, Houston, TX, USA, June 19-23.
- [90] Uchiumi M., Kamijo K., Hirata K., Konno A., Hashimoto T., Kobayasi, S., 2003, "Improvement of Inlet Flow Characteristics of LE-7A Liquid Hydrogen Pump", Journal of Propulsion and Power, Vol. 19, No. 3.
- [91] Uchiumi M., Kamijo K., 2008, "Occurrence Range of a Rotating-Stall-Type Phenomenon in a High Head Liquid Hydrogen Inducer", Proceedings of ISROMAC-12 - the 12th International Symposium on Transport Phenomena and Dynamics of Rotating Machinery, Honolulu, Hawaii, USA, February 17-22.
- [92] Wade R. B., Acosta A. J., 1966, "Experimental Observations on the flow past a plano-convex hydrofoil", J. of Basic Engineering, Vol. 87, pp. 273-283.
- [93] Watanabe S., Yokota K., Tsujimoto Y., Kamijo K., 1999, "Three-Dimensional Linear Analysis of Rotating Cavitation in Inducers Using an Annular Cascade Model", ASME J. of Fluids Engineering, Vol. 121, pp. 866-871.
- [94] Yamamoto K., 1991, "Instability in a Cavitating Centrifugal Pump", JSME Int. J., Ser. II, 34, 9-17.
- [95] Yoshida Y., Tsujimoto Y., Kataoka D., Horiguchi H. and Wahl F., 2001, "Effects of Alternative Leading Edge Cutback on Unsteady Cavitation in 4-Bladed Inducers", Journal of Fluid Engineering, Vol. 123, no. 4, pp. 762-770, December.
- [96] Yoshida Y., Tsujimoto Y., Morimoto G., Nishida H., Morii S., 2003, "Effects of Seal Geometry on Dynamic Impeller Fluid Forces and Moments", ASME Journal of Fluids Engineering, 125, pp. 786-795.
- [97] Yoshida Y., Kazami Y., Nagaura K., Shimagaki M., Iga Y., Ikohagi T., 2008, "Interaction Between Uneven Cavity Length and Shaft Vibration at the Inception of Synchronous Rotating Cavitation", Proceedings of ISROMAC-12 - the 12th International Symposium on Transport Phenomena and Dynamics of Rotating Machinery, Honolulu, Hawaii, USA, February 17-22.
- [98] Yoshida Y., Eguchi M., Motomura T., Uchiumi M., Kure H., Maruta Y., 2010, "Rotordynamic Forces Acting on Three-Bladed Inducer under Supersynchronous /Synchronous Rotating Cavitation", ASME Journal of Fluids Engineering, 132.
- [99] Watanabe S., Yokota K., Tsujimoto Y., Kamijo K., 1999, "Three-Dimensional Linear Analysis of Rotating Cavitation in Inducers Using an Annular Cascade Model", ASME Journal of Fluids Engineering, Vol. 121, pp. 866-871.
- [100] Zoladz T., 2000, "Observations on Rotating Cavitation and Cavitation Surge from the Development of

**Fluid Dynamics Associated to Launcher Developers**

---

the Fastrac Engine Turbopump”, 36th AIAA/ASME/SAE/ASEE Joint Propulsion Conference, Huntsville, USA.

